UCN Detector development for the TRIUMF Neutron EDM experiment

by

Fleurette Doresty Fonseca

A Thesis submitted to the Faculty of Graduate Studies of

The University of Manitoba

in partial fulfillment of the requirements of the degree of

MASTER OF SCIENCE

Department of Physics and Astronomy

University of Manitoba

Winnipeg

ABSTRACT

A new measurement of the neutron electric dipole moment (nEDM) is being developed at TRIUMF, where a high density source of ultra cold neutrons (UCN) is currently under construction. A fast, high-efficiency UCN detector is needed for the experiment, and a 6-Li doped glass scintillation detector is being explored for this purpose. In this work, simulations and test measurements were carried out to optimize the light guide design for the new UCN detector. Acrylic and air-core light guides, the latter with two different reflecting surfaces, were considered. Three prototype light guides were constructed and tested, and results were compared with simulations. The best solution was found to be an acrylic guide, wrapped with mylar foil. For a guide 12 cm in length as required by the experimental layout, a lower limit of approximately 25 photoelectrons per neutron capture was established for the proposed geometry and photomultiplier configuration.

«ad majorem Dei gloriam»

ACKNOWLEDGMENT

I would like to express my sincerest gratitude to my supervisor Professor Michael Gericke for giving me the opportunity to conduct my studies in his research group. It was his continuous guidance and support during my master studies which made this work possible. I also would like to give special thanks to my co–supervisor Professor Shelley Page for her constant help, encouragement and insightful comments which gave a substantial contribution to the development of this dissertation. I am very grateful to both of them for sharing their experience, time, wisdom and energy with me during these years.

I would also like to acknowledge all the professors from whom I received invaluable knowledge during my studies at this University, and also to the entire Physics and Astronomy department for assiting me in times of need.

As well, I would truly like to thank Dr. Peiqing Wang and Dr. Jie Pan for their patience and for taking the time to answer my questions. A big thanks to my fellow graduate students and friends at the University of Manitoba, Carlos, Mario, Taraneh, Sr Elaine for helping me and making my time at the University more pleasant. To my colleagues, friends and family around the world and to all the special people that I have met during my journey in physics, including my Winnipeg family and friends. In each one of them I have found the motivation for pursuing this fascinating path, and I have had the opportunity to discover new worlds in each shared moment.

One of my biggest gratitutes goes to my parents Marlen Fonseca and Wilson Doresty, and my sister Pauline for believing in me and for encouraging me since I decided to become a physicist. They have been a constant light shining the way. A huge thanks to my beloved Javier for sharing this adventure with me, for supporting me countless times and fighting by my side to conquer this dream. And finally, my deepest and foremost thanks to God for giving me the strength and being my center and my refuge every day of this journey.

LIST OF ABBREVIATIONS

ADC	Analog to Digital Converter
CP	Charge–Parity
CPT	Charge, Parity and Time Reversal
EDM	Electric Dipole Moment
GEANT	Particle Physics Simulation Package
KEK	The High Energy Accelerator Research Organization
LPSS	Long–Pulse Spallation Source
NPE	Number of Photoelectrons
ORNL	Oak Ridge National Laboratory
PE	Photo–Electron
PHITS	Particle and Heavy Ion Transport Code System
PMT	Photomultiplier Tube
PSI	Paul Scherrer Institute
PSNS	Pulsed Spallation Neutron Sources
QDC	Charge–to–Digital Converter
RCNP	Research Center for Nuclear Physics
RF	Radio frequency
RMS	Root Mean Square
SNS	Spallation Neutron Source
SPSS	Short–Pulse Spallation Source
TRIUMF	Tri–University Meson Facility
UCN	Ultra–cold neutrons
VME	Versa–Module Eurobus

CONTENTS

LIST OF FIGURES

LIST OF TABLES

1

INTRODUCTION

The presence of a nonzero electric dipole moment (EDM) in a system indicates Charge-Parity (CP) violation in that system, which would be an indication of new physics beyond the Standard Model. A good candidate experiment to search for CP violation is the search for a non-zero EDM of the neutron, and a first upper limit on its EDM value of $|\mathrm{d}_n| < 3 \times 10^{-20}\, e \cdot cm$ was obtained in 1957 [Smi57]. Since then, different experiments around the world have been designed and constructed in order to push down this limit, by improving the statistical and systematic sensitivity of the experiment.

A new, very precise, measurement of the neutron EDM will take place at TRIUMF, where a new ultra cold neutron source is expected to reach the largest density of ultra–cold neutrons. A prototype experiment has been developed at RCNP[1], and will be moved to TRIUMF, where improvements will be undertaken in order to increase the storage time and the density of UCN in the EDM cell.

The neutron EDM will be measured using Ramsey's technique [Ram82], and the number of polarized neutrons need to be counted after this process (see Section 1.1.4). The total number of detected neutrons is one of the factors determining the statistical error in the measurement[2], hence the importance of having a high UCN density. Since a high rate of UCN is expected in the new facility at TRIUMF, the experiment requires UCN detectors that can operate at high rates. Li–6 doped glass scintillators, which are under development for the EDM experiment, will be used for neutron counting at TRIUMF.

Light guides are required to guide photons obtained from the scintillation process to the photomultiplier. The purpose of this work was to study the light collection for three

[1] Research Center for Nuclear Physics, Japan.
[2] Other parameters are the storage time and the electric field.

different light guide materials. It is expected that these results may be used to optimize the detector and light guide configuration for the neutron UCN detector at TRIUMF. This work was performed by simulating the light collection of a prototype detector with different light guide materials in Geant4 [Gea15a]. Additionally, experimental tests were performed at the University of Manitoba in order to benchmark the simulation results.

This thesis is organized into five chapters as follows:

- Chapter 1: a brief discussion of the general properties of UCN, and the motivation and general aspects of the EDM measurements.
- Chapter 2: the main aspects of neutron production and cooling techniques for ultra-cold neutron production at TRIUMF.
- Chapter 3: a brief discussion of the scintillation process, the ^{6}Li glass scintillators and the other main components of the UCN detector.
- Chapter 4: the conceptual design of the prototype detector, simulations in Geant4, experimental results and discussions.
- Chapter 5: a summary of the work and a future outlook on the UCN detector.

1.1 Neutrons and ultra-cold neutrons

1.1.1 Fundamental properties

The neutron is a subatomic particle with a net electric charge equal to zero. In part because it is electrically neutral, the neutron is an ideal testing ground for nuclear and particle theory [AL12]. Neutrons and protons are the constituents of atomic nuclei, where neutrons on average constitute more of the 50% of the nucleus. The strong nuclear force between these two particles keeps them tightly bound in competition with the Coulomb repulsion of the protons.

There is a mass difference between the neutron and proton[3], with the proton being lighter than the neutron, which means that the free neutron is energetically allowed to decay to a proton. A free neutron is therefore unstable and beta decays to a proton via the reaction:

$$n \rightarrow p + e^{-} + \bar{\nu}_e,$$

where a neutron decays to a proton, an electron and an electron antineutrino, with a mean lifetime of $\tau = 880.1 \pm 1.1$ seconds. The properties of the neutron are summarized in Table 1.1 [B+12].

Property	**Experimental value**
Mass (MeV/c^2)	939.565379 ± 0.000021
Mean life time (s)	880.1 ± 1.1
Magnetic moment (μ_N)	$-1.91304272 \pm 0.00000045$
Mean-square charge radius (fm^2)	-0.1161 ± 0.0022
Charge ($10^{-21}e$)	-0.2 ± 0.8
Spin	1/2
Isospin	1/2
Quark content	udd

Table 1.1 Fundamental properties of the neutron.

[3]The proton mass m_p equals 99.86% of the neutron mass m_n.

1.1.2 Fundamental interactions for low energy neutrons

Neutrons are affected by the four fundamental interactions in nature: gravitational, strong, weak and electromagnetic interactions.

- **Gravitational interaction**

  Since ultra–cold neutrons are non–relativistic, massive objects, their gravitational interaction can be most easily quantified by considering their gravitational potential energy when falling from a certain height above a surface. This is also relevant for the UCN detector design, since the UCN will need to acquire a certain kinetic energy before they hit the detector, in order to be detected. The corresponding UCN potential energy is given by:

$$\begin{aligned} U_{grav} &= mgh \\ &= 103 \left(\frac{\text{neV}}{\text{m}} \right) h, \end{aligned}$$

  where m is the neutron mass, g is the acceleration due to gravity and h is the vertical distance. Therefore, by energy conservation, neutrons in free fall accelerate and their kinetic energy increases. For instance, neutrons falling from 1 meter will have enough kinetic energy (103 neV) to pass through the aluminum foil ($\sim 100\ \mu$m) in front of a neutron detector. As neutrons rise above some surface, their potential energy increases, while their kinetic energy decreases. For example, UCN with an initial kinetic energy below 103 neV will not be able to reach the top of a UCN container of 1 m height.

- **Magnetic interaction**

  The neutron has a magnetic moment $\vec{\mu}$ associated with its spin. In the presence of an external magnetic field, the magnetic potential energy due to the interaction of the magnetic moment with the field is given by

$$U_{\text{m}} = -\vec{\mu} \cdot \vec{B}(r) \tag{1.1}$$

As we can see from Table 1.1, the magnetic moment has a value proportional to the nuclear magneton $\mu = -1.91304272\mu_N = -9.6623650(23) \times 10^{-27} \frac{\text{J}}{\text{T}}$ [COD15]. The potential energy of a neutron in an external magnetic field is then approximately $U_m = -60 \left(\frac{\text{neV}}{\text{T}}\right) B$.

Using the expression above, the magnetic force experienced by a neutron in a non–uniform field $\vec{B}$ can be found by calculating the gradient of the potential:

$$\vec{F}_m = -\vec{\nabla} U_m = \vec{\nabla}(\vec{\mu} \cdot \vec{B})$$

In the above result it is assumed that due to the low speed of the neutrons, the magnetic moment of these particles are always oriented in the direction of the magnetic field, satisfying the adiabatic condition. This condition states that the variation in time of the magnetic field $\vec{B}$ seen by the neutron as it moves in the magnetic field, is lower than the Larmor frequency of precession of the neutron ω_0 [GRL91]:

$$\frac{1}{|\vec{B}|} \cdot \left| \frac{d\vec{B}}{dt} \right| \ll \frac{\vec{\mu} \cdot \vec{B}}{\hbar} = \omega_0 \tag{1.2}$$

- **Strong interaction**

The strong interaction is a short range interaction, responsible for binding together protons and neutrons to form nuclei, and also for keeping tightly bound quarks inside baryons (composed of three quarks) and mesons (composed of one quark and one antiquark). This fundamental interaction is also responsible for the total external reflection at any angle of incidence of ultra–cold neutrons, impinging on the walls of a container for a variety of materials.

Low energy neutron scattering is best understood using the usual solid state formalism used for crystalline structures. For a neutron interacting with a collection of N nuclei in a solid with some lattice structure, the potential describing this interaction

in first Born approximation is [Kas04]:

$$V(\vec{r}) = \frac{2\pi\hbar^2}{m} \sum_l b_l \delta(\vec{r} - \vec{R}_l), \tag{1.3}$$

where m is the mass of the neutron, b_l is the scattering length (the sum is over those nuclei that are contained within the region corresponding to the size of the neutron wavelength), and $\vec{R}_l$ are the positions of the nuclei in the solid. For very low energies, this potential further approximates to a step function $V = V_F$ (> 0) at the surface of the material such that neutrons incident on the potential barrier with insufficient energy will be totally reflected.

In terms of the neutron's kinetic energy (E_{kin}), this reflection takes place for energies lower than the effective potential (V_F) of the material, known as the *Fermi potential* via the condition:

$$E_{kin} \sin^2\theta \leqslant V_F, \tag{1.4}$$

where $V_F = \left(\frac{2\pi\hbar^2}{m}\right) Nb$, θ is the angle of incidence of UCN with respect to the normal to the surface and N is the number density of nuclei corresponding to the material that the container wall surfaces are made from. The above expression is satisfied for any value of θ and therefore ultra–cold neutrons will be reflected by the material surface for [GRL91]:

$$E_{kin} \leqslant V_F. \tag{1.5}$$

UCN are trapped when condition (1.5) is satisfied; however, it must be admitted that a small amount of surface absorption is possible, giving rise to small but finite loss probability associated with each wall bounce.

The Fermi potential of some relevant materials is shown in Table 1.2.

Element	^{58}Ni	BeO	Fe	Cu	Al
V_F (neV)	335	261	210	168	54

TABLE 1.2 Fermi potential of different common materials [GRL91].

- **Weak interaction**

  This interaction is responsible for the β–decay of the neutron:

$$n \rightarrow p + e^{-} + \overline{\nu}_e$$

  previously mentioned. The relation is represented in the quark model as a process in which a down-quark is transformed into an up-quark as shown in the expression below [Ale92]:

$$d \rightarrow u + e^{-} + \overline{\nu}_e$$

  The free neutron decay is of great interest since a precise value of the neutron lifetime is required as a test of the Standard Model and for theoretical estimations in Big–Bang Nucleosynthesis [Yan06].

1.1.3 Tests of fundamental symmetries with neutrons

In physics, there are three important discrete symmetries: Charge conjugation (C), Parity (P) and Time reversal (T). A Hamiltonian is invariant if it is unchanged under the product of transformations CPT; this is known as the *CPT Theorem* [Soz08]. CPT is now understood to be a fundamental symmetry of nature.

There is conclusive evidence [CDS12] that the amount of matter and antimatter contained in the universe is not equal. This may be explained by considering an anti-symmetrical process at the beginning of the universe [CDS12] [Hĺ4]. Sakharov in 1967 [Sak67], stated three criteria which must be satisfied in order to explain the baryon asymmetry (the amount of matter and antimmater are not the same) in the universe:

1. A non-conservation of the baryon number is required to allow the system to change its baryon number over time.

2. Charge and CP violations are required to favour the predominance of matter with respect to antimatter in the universe.

3. These processes should have occurred in a non-thermal equilibrium phase of the universe, since in thermal equilibrium the baryon number would be constant.

The Standard Model predicts an asymmetry in the baryon content of the universe, which is nine orders of magnitude smaller than the experimental observations [BCS04]. Considering criterion 2 from above, this situation motivates the introduction of physics beyond the Standard Model, with new sources of CP violation in order to explain the observed baryon asymmetry. This, in turn, motivates experimental searches for these new CP violating effects. A consequence of the new CP violating physics is that the neutron should have a non-zero electric dipole moment at the level of $d_n \lesssim 10^{-27} - 10^{-28}\, e \cdot cm$ (predicted by Supersymmetry). Neutron EDM searches are therefore an important way to verify the new CP violating models.

The Hamiltonian for a neutron in the presence of electric $\vec{E}$ and magnetic $\vec{B}$ fields, is [LG93]:

$$H = -\vec{\mu} \cdot \vec{B} - \vec{d} \cdot \vec{E} \tag{1.6}$$

where $\vec{d}$ and $\vec{\mu}$ are the electric and magnetic[4] dipole moments, respectively.

Table 1.3 lists the behavior of the Hamiltonian and its parts under parity and time reversal transformations, showing that with the introduction of an electric dipole moment (the second term) the Hamiltonian (eqn (1.6)) is odd, under both P and T and therefore also under CP (with the E and B fields specified as experimental control variables).

	P	T
$\vec{\mu}$	$\vec{\mu}$	$-\vec{\mu}$
$\vec{\mathrm{d}}$	$-\vec{\mathrm{d}}$	$\vec{\mathrm{d}}$
$\vec{\mathrm{E}}$	$-\vec{\mathrm{E}}$	$\vec{\mathrm{E}}$
$\vec{\mathrm{B}}$	$\vec{\mathrm{B}}$	$-\vec{\mathrm{B}}$

TABLE 1.3 Behaviour of physical observables under Parity and Time-reversal operations [Soz08].

If CPT symmetry is assumed, a violation of CP symmetry is implied with the existence

[4] Electric and magnetic dipole moments lie in the spin direction $\frac{\vec{S}}{S}$, i.e., $\vec{\mu} = \mu\frac{\vec{S}}{S}$ and $\vec{d} = d\frac{\vec{S}}{S}$, where $\vec{S} = \frac{\hbar}{2}\vec{\sigma}$.

of a non zero $\vec{d}$. In models that are consistent with the observed matter–antimatter asymmetry, the neutron EDM is in the range between 10^{-28} and $10^{-26}\, e{\cdot}cm$, and improved experimental values will provide constraints on these theories.

Early interest in the neutron EDM as a source of time-reversal violation was motivated by the work of Lee and Yang [LY56] and Wu [WAH+57], which found violations of P symmetry in the K^0 decay and in nuclear beta decay. Purcell and Ramsey stated in a note published in 1950 [Pur50] that even when some theoretical predictions based on symmetry arguments rejected the idea that nuclei and elementary particles might have EDMs, they proposed that a definite conclusion should come from experimental evidence. This led them to work with J.H. Smith (1957) in an experiment where they used *"a neutron beam resonance apparatus of high resolution to detect a possible shift of the neutron precession frequency upon the application of a strong electric field"*, as described by Purcell and Ramsey in [Pur50]. The experimental limit reached by Smith, Purcell and Ramsey [Smi57] was $|\vec{d}_n| < 5 \times 10^{-20}\, e \cdot cm$.

1.1.4 Measurement of the neutron EDM

Currently, the neutron EDM (nEDM) can be measured using Ramsey's separated oscillatory fields magnetic resonance method [Ram82]. The following description of the nEDM experiment is based on the one included in the proposal for the nEDM experiment at TRIUMF [C15].

Figure 1.1 shows the apparatus that will be used for Phase I of the nEDM experiment at TRIUMF. UCN will be produced and guided to the EDM cell which is placed in a homogeneous magnetic field ($\vec{B}_0$) and a strong electric field ($\vec{E}$), where the precession frequency of neutrons will be measured. The results from the spin resonance will be observed by means of the UCN spin analyzer and detector, as will be discussed in subsection 3.4.

The experimental setup using Ramsey's method to measure the precession frequency is briefly explained here. Neutron spins are aligned to the static magnetic field $\vec{B}_0$ before an oscillating magnetic field $\vec{B}_1$ of angular frequency ω, is applied in a perpendicular

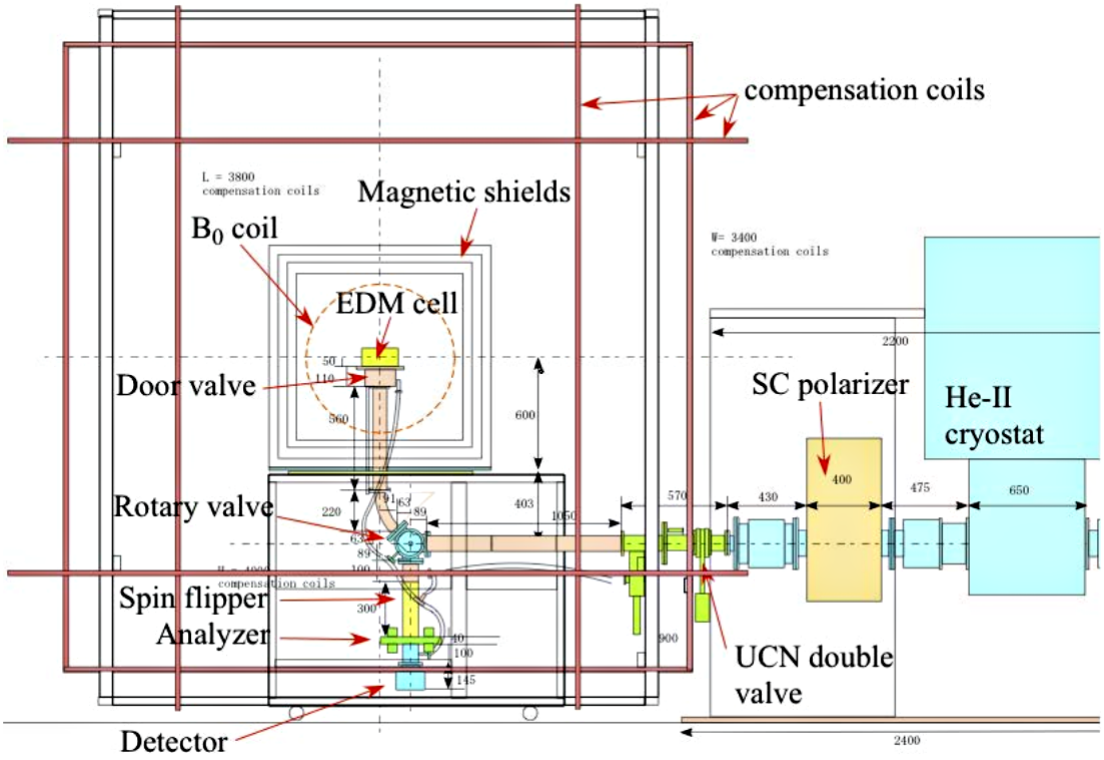

FIG. 1.1 Diagram of the apparatus for the EDM experiment at TRIUMF [C15].

direction to $\vec{B}_0$, in the $x-y$ plane (see diagram to the left in Figure 1.2). This RF $\vec{B}_1$ pulse is applied for a period τ during which the spin direction rotates by 90 degrees; this pulse is known as $\frac{\pi}{2}$–pulse. After the RF pulse is turned off, the UCN are free to precess in the horizontal plane in the presence of the electric and magnetic fields for a period of time T (where $T >> \tau$). The frequency at which this occurs is the Larmor frequency $\omega_0 = \gamma B_0$, where γ is the neutron gyromagnetic ratio. During the precession, the direction of the $\vec{E}$ field is alternated to be either parallel or antiparallel with the $\vec{B}_0$ field. The energy of the neutron in these fields can be written as

$$\hbar\omega_0^{\pm} = 2|\mu_n \mathrm{B}_0 \pm \mathrm{d}_n \mathrm{E}| \tag{1.7}$$

where $+$ and $-$ signs are for parallel and antiparallel directions of the fields respectively. After the time T passes, a second RF pulse, of magnitude B_1 and angular frequency ω, is applied for a time τ. This $\frac{\pi}{2}$–pulse rotates the spin of the neutron by another 90

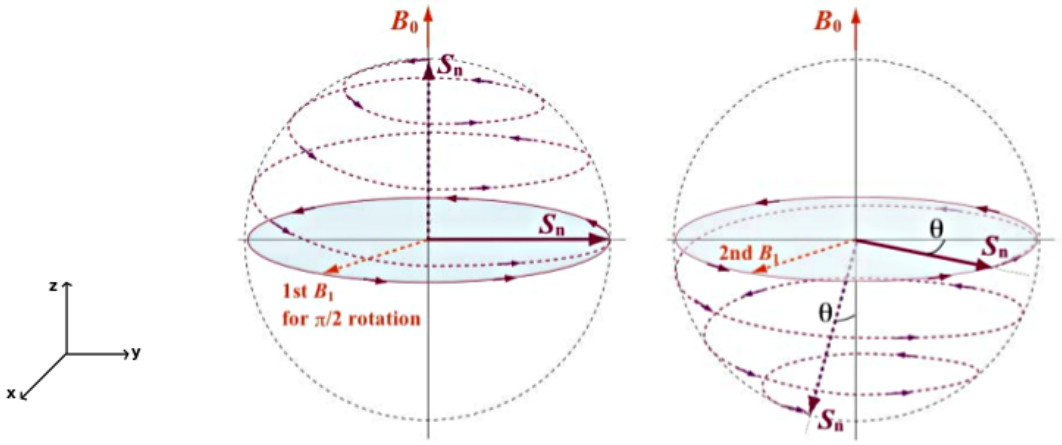

FIG. 1.2 Schematic representation of a system of spin 1/2 precessing in a magnetic field [C15]. This picture is semi–classical; $\vec{S}_n$ along $\vec{B}_0$ means $\langle \vec{S}_n \cdot \hat{k} \rangle = \frac{1}{2}\hbar$ (it is not exactly parallel to but it does precess around $\vec{B}_0$).

degrees, as shown to the right in Figure 1.2. A total reversal of the spin occurs if the RF pulses are in phase with the neutron spin precession; otherwise the spin direction will change according to the difference of frequency with respect to the Larmor frequency ($\Delta\omega = \omega - \omega_0$). The actual precession frequency of the neutrons is obtained by detuning the RF pulse and counting both spin states (up and down) of the UCN as ω is scanned near ω_0. As a result, the so–called *Ramsey pattern* is generated.

Figure 1.3 shows the results from a Ramsey resonance at RCNP. The central part of this figure corresponds to a complete reversal of the spin, i.e., where the difference of frequency of both reversal frequencies with respect to the Larmor frequency equals zero (resonance frequency). In addition, the four steepest points on the central part of the resonance pattern are marked in red color; the frequency shift is found from accumulated experimental data at these points.

The nEDM is measured from a shift in the central frequencies obtained from a combination of relations for parallel and antiparallel fields in expression (1.7). The resulting equation for the nEDM is:

$$d_{\mathrm{n}} = \frac{\hbar\left(\omega_0^{+} - \omega_0^{-}\right)}{4E} \tag{1.8}$$

Using the above relation, once spin precession frequencies in both $\vec{E}$ field directions are known, it is possible to find the electric dipole moment of the neutron.

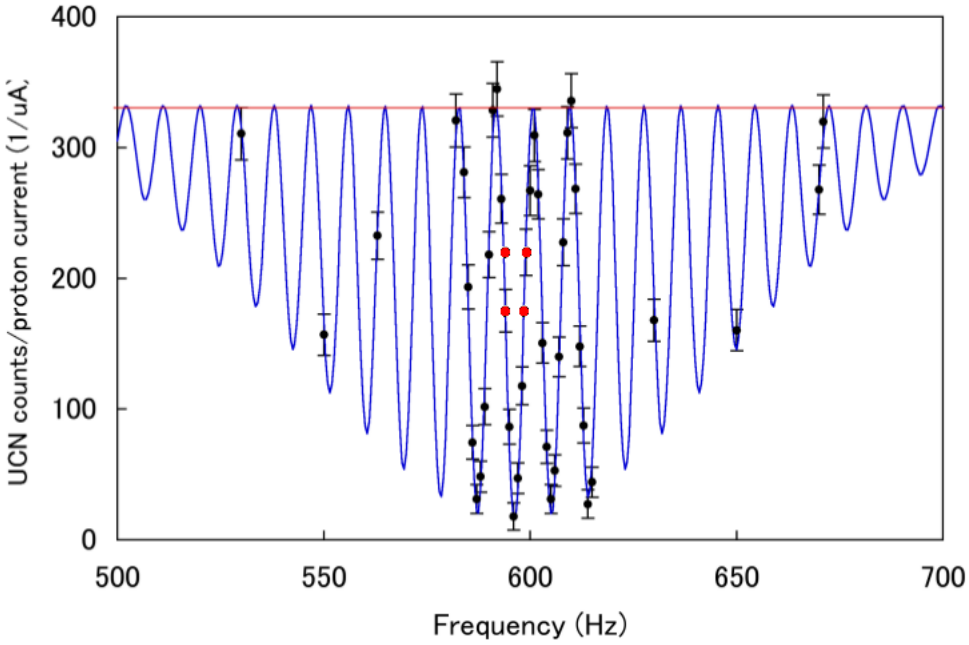

FIG. 1.3 Ramsey pattern obtained at RCNP with a static magnetic field of 10 μT and $T = 100$ ms. The central part in the pattern indicates a complete spin reversal [MM+15].

The statistical precision of this method is limited by the statistical error per measurement cycle, as follows[5]:

$$\sigma(\mathrm{d}_n) = \frac{\hbar}{2\alpha \mathrm{E} \mathrm{T} \sqrt{N}},$$

where α is the visibility of the central resonance fringe defined as $\alpha = \frac{N^{\uparrow/\downarrow}_{\max} - N^{\uparrow/\downarrow}_{\min}}{N^{\uparrow/\downarrow}_{\max} + N^{\uparrow/\downarrow}_{\min}}$, T is the time of free precession and N is the number of neutrons counted in the experiment. The goal of current and future nEDM measurements, including the neutron EDM measurement at TRIUMF, is to improve the statistics and sensitivity.

Table 1.4 shows values for the nEDM setup using Ramsey's technique in the RAL–SUSSEX–ILL and RCNP experiments, along side with the goal statistical error of $\sigma(d_\mathrm{n}) =$

[5]This formula is obtained by calculating the error propagation of d_n in equation (1.8): $\sigma_{d_\mathrm{n}} = \frac{\hbar}{4E}\sqrt{\sigma^2_{\omega_0^+} + \sigma^2_{\omega_0^-}}$. The values of $\sigma_{\omega_0^\pm}$ are calculated from an expression of the neutron Larmor frequency in terms of detected neutrons, which is not discussed in this work, but is fully described in [HÍ4].

2.0×10^{-26} $e \cdot cm$/day, for the proposed TRIUMF measurement, at the end of the first phase of operation [C15].

Parameter	ILL	RCNP	TRIUMF
B_0	1 μ T	2 μ T	1 μ T
α	0.60	0.90	0.95
E	10 kV/cm	10 kV/cm	10 kV/cm
T	130 s	30 s	130 s
N	14,000 UCN/edm cycle (1 cycle = 210 s)		2.3×10^8 UCN per day
σ_{d}	2.0×10^{-25} $e \cdot cm$/day		2.0×10^{-26} $e \cdot cm$/day

TABLE 1.4 Parameters from nEDM experiments at PSI, RCNP and TRIUMF [Rog09] [C15]. The values contained in the table are the static magnetic field (B_0), the visibility of the central fringe (α), the free precession time (T), the number of UCNs (N), and the statistical sensitivity ($\sigma(d_{\mathrm{n}})$).

1.1.5 History of neutron EDM measurements

Different experiments have been designed around the world, with the aim of measuring the neutron EDM [ZT12]. Some of these are listed in Table 1.5 including the name of the institution, the goal experimental limit, and the type of detector used in each case. So far, the best limit has been set by the Sussex-RAL-ILL collaboration with a precission of 2.9×10^{-26} e.cm (90% CL). The nEDM experiment at TRIUMF has a long-term goal of reaching the world's highest sensitivity ($\sigma(d_{\mathrm{n}}) = 10^{-27}$ $e\cdot$ cm [C15]) by the end of the decade.

One of the main instruments in the measurement of a neutron EDM is the UCN detector. Different types of UCN detectors have been considered, depending on the particular needs of each experiment. Two examples are the PNPI-ILL experiment which has a silicon UCN detector with a ^{6}LiF converter [S+13], and the experiment at TRIUMF which will use ^{6}Li doped glass scintillators to capture ultra-cold neutrons [C15], first built at PSI [BFL+05]. A detailed discussion about the detector that is planned to be implemented at TRIUMF is presented in the next chapter.

Collaboration	Goal (precision)	Type of detector	Status
PSI UCN Source [Rog09] [HÍ14]	$d_n < 5 \times 10^{-28}$ e cm	^{6}Li-doped glass scintillators	Working
ILL - CryoEDM [C$^+$10]	$d_n < 2.2 \times 10^{-28}$ e cm	Cryogenic solid state detectors with a thin surface film of ^{6}LiF	In commissioning stage
PNPI - ILL [S$^+$13]	$d_n < 5.5 \times 10^{-26}$ e cm	Silicon UCN detector with a ^{6}LiF converter	Working
SNS nEDM [Zhe12]	$\sigma(d_n) = 3 \times 10^{-28}$ e cm	^{3}He gas-detector	Under construction
FRM-II [A$^+$12]	$d_n < 5 \times 10^{-28}$ e cm	UCN detector with Ti/^{6}LiF multi-layer converter and ^{58}Ni reflector [M$^+$02]	Under construction
RCNP - TRIUMF [C15]	$\sigma(d_n) \sim 10^{-27}$ e cm	^{6}Li-doped glass scintillators	Under construction

TABLE 1.5 nEDM experiments around the world.

2

ULTRA COLD NEUTRON SOURCE AT TRIUMF

2.1 Physics of neutron production

In this chapter the production of ultra–cold neutrons is discussed. The production takes place in three stages: neutron production from a spallation source, cold neutron production from a moderation process in heavy water, and UCN production in He–II. For each process, a theoretical description is included followed by a general description of the prototype experiment at KEK–RCNP and finally the proposed experiment at TRIUMF.

2.1.1 Neutron production

There are no free neutrons in nature, since their decay time is $\sim$ 15 min; neutrons are only stable inside nuclei. Therefore, in order to use them in experiments they have to be released from their stable configuration inside an atomic nucleus. There are two different and complementary ways in which neutron beams can be produced: the fission process, where a heavy nucleus splits into two lighter species, releasing neutrons; and the spallation process, where a target of heavy nuclei is bombarded with energetic protons, and excess neutrons are released. Neutrons are liberated with a high energy ($\sim$ MeV) and need to be slowed down before they can be used in EDM experiments (e.g. to maximize the interaction time while performing measurements).

- **Spallation process**

  In a spallation process, a projectile beam such as protons, neutrons or light nuclei with a high energy (from 100 MeV to several GeV), bombards a target of heavy

nuclei, emitting a large quantity of neutrons. This process will be used to generate neutrons in the facility at TRIUMF, and it will be discussed in more detail in the following text.

Consider an example of a spallation reaction in which a proton with an energy of 1 GeV strikes a lead target (^{208}Pb). As result of this reaction, there are 30 neutrons liberated on average, as well as a range of heavier nuclear fragments [Ben06]. As an illustration, the cross sections for producing heavy nuclear fragments in the spallation process of a ^{208}Pb beam (208 GeV) impinging on a hydrogen target, were measured by Enqvist et al. (2001)[E$^+$01]. Their results can be observed in the chart of nuclides in Figure 2.1.

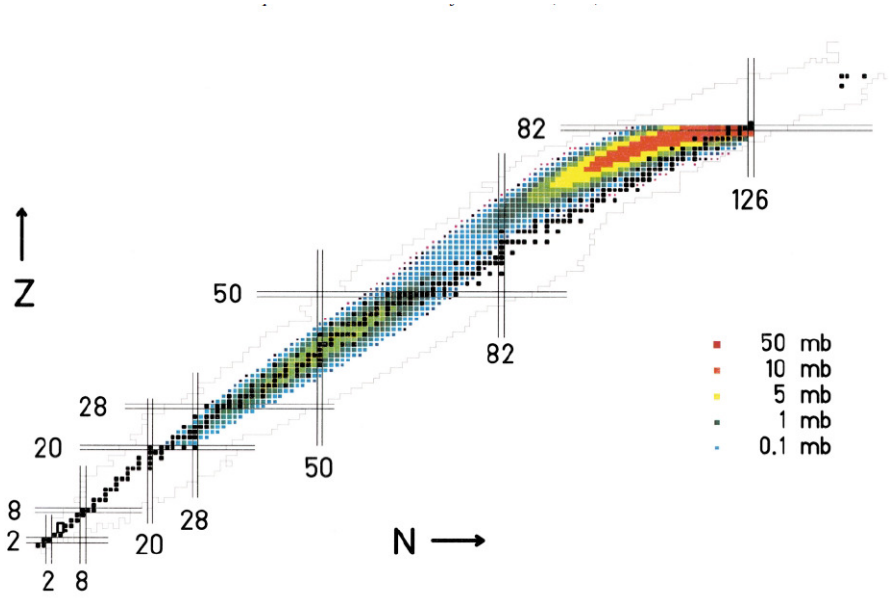

FIG. 2.1 Illustration of the wide range of heavy nuclear products that can be produced in a spallation reaction. Experiment: heavy ion ^{208}Pb beam impinging on LH_2 at 1 GeV/nucleon. The color code indicates a wide range of production cross sections between 0.1 and 50 mb; 1 mb = 10^{-27} cm^2 [E$^+$01].

A high energy proton striking a heavy nuclear target in a spallation process, interacts directly with one of the constituent nucleons, due to its short Broglie wavelength. As result of this collision, neutrons and other particles are produced in a two–stage process, as shown in Figure 2.2, which corresponds to the internuclear cascade and

evaporation of particles [Wat03].

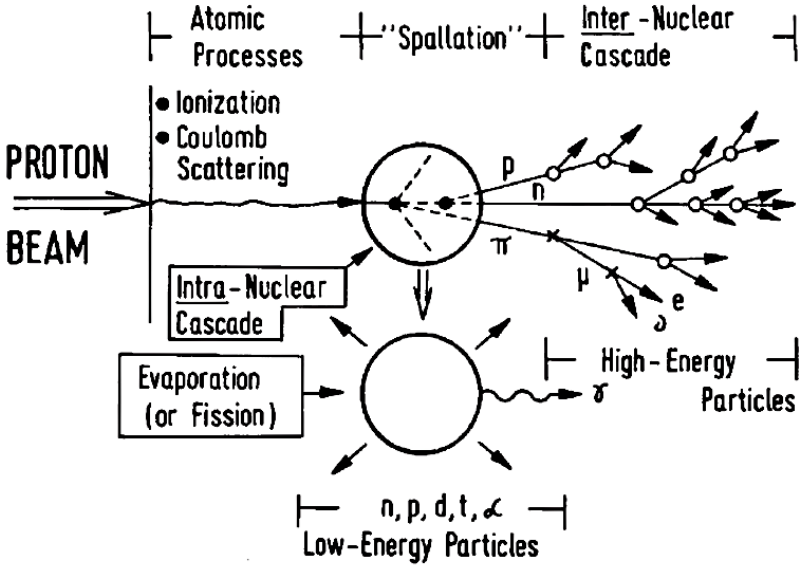

FIG. 2.2 A schematic representation of spallation process [Wat03].

In the internuclear cascade a high energy proton in a spallation process liberates high energy neutrons, and also other particles such as pions and protons, which are ejected in the same general direction of the incident proton [Wat03]. After this process, some nuclei remain excited and the second stage of the spallation process takes place. At this point, low energy particles such as protons, neutrons, deuterons and tritons evaporate isotropically from excited nuclei. The neutrons produced at this stage are of particular interest, as these can be moderated and converted into cold neutrons. The remaining energy of nuclei after particle evaporation is liberated by the emission of gamma rays. The incoming beam can also trigger a slower timescale fission process via the formation of unstable nuclei, which is relevant since neutrons are also produced as a result of the fission reaction.

The advantage of using the spallation process is that it can produce intense pulsed beams of neutrons, and the pulsed nature allows for better control of systematic effects and backgrounds. The pulse width in the proton beam is determined in the accelerator/storage ring and this, in turn, determines the timing structure of the

neutron pulses. The instantaneous intensity of neutron production can be increased by compressing the time interval over which neutrons are produced. The ability to produce a large number of neutrons in a short time interval is the major advantage of spallation sources over reactor sources. An important advantage of a pulsed source is the possibility to use the Time of Flight (TOF) method to determine the velocity and therefore energy of the produced neutrons [VBZR12].

Depending on the time structure, Pulsed Spallation Neutron Sources (PSNS) can be classified into two categories: a short–pulse spallation source (SPSS) and a long–pulse spallation source (LPSS) [VBZR12]. In a SPSS, protons coming from the linear accelerator are stored in a synchrotron ring before they collide with the target. This way, higher density proton beams can be generated and a larger number of neutrons are delivered in a shorter time. Short pulses combined with a small repetition rate prevent a possible overlap between slow and fast neutrons belonging to different pulses [Len93]. On the other hand, in a LPSS protons are extracted directly from the linear accelerator, producing a mean neutron flux which is higher, compared to the SPSS sources.

An example of a SPSS is the Spallation Neutron Source (SNS) at the Oak Ridge National Laboratory (ORNL), in the USA [Ale10]. For this spallation source, the time structure of the proton beam is shown in Figure 2.3 where two different types of structure can be observed: a macrostructure and microstructure. The Macrostructure diagram in this figure shows that the width of the pulse is 1 ms, which is repeated at 15.7 ms intervals. Each 1 ms pulse is composed of several subpulses, which is referred to as the microstructure of the pulse. The width of each subpulse is 64.5 ns and the separation between them is about 300 ns, as shown in the lower diagram in Figure 2.3.

A SPSS time structure is planned for the new facility at TRIUMF as shown in Figure 2.4. The primary beamline (BL1U) (see Figure 2.6) will deliver 40 μA proton pulses with an energy of 500 MeV to the spallation target; this delivery will be done by a combination of a Septum and Kicker magnets (not discussed in this work [C15])

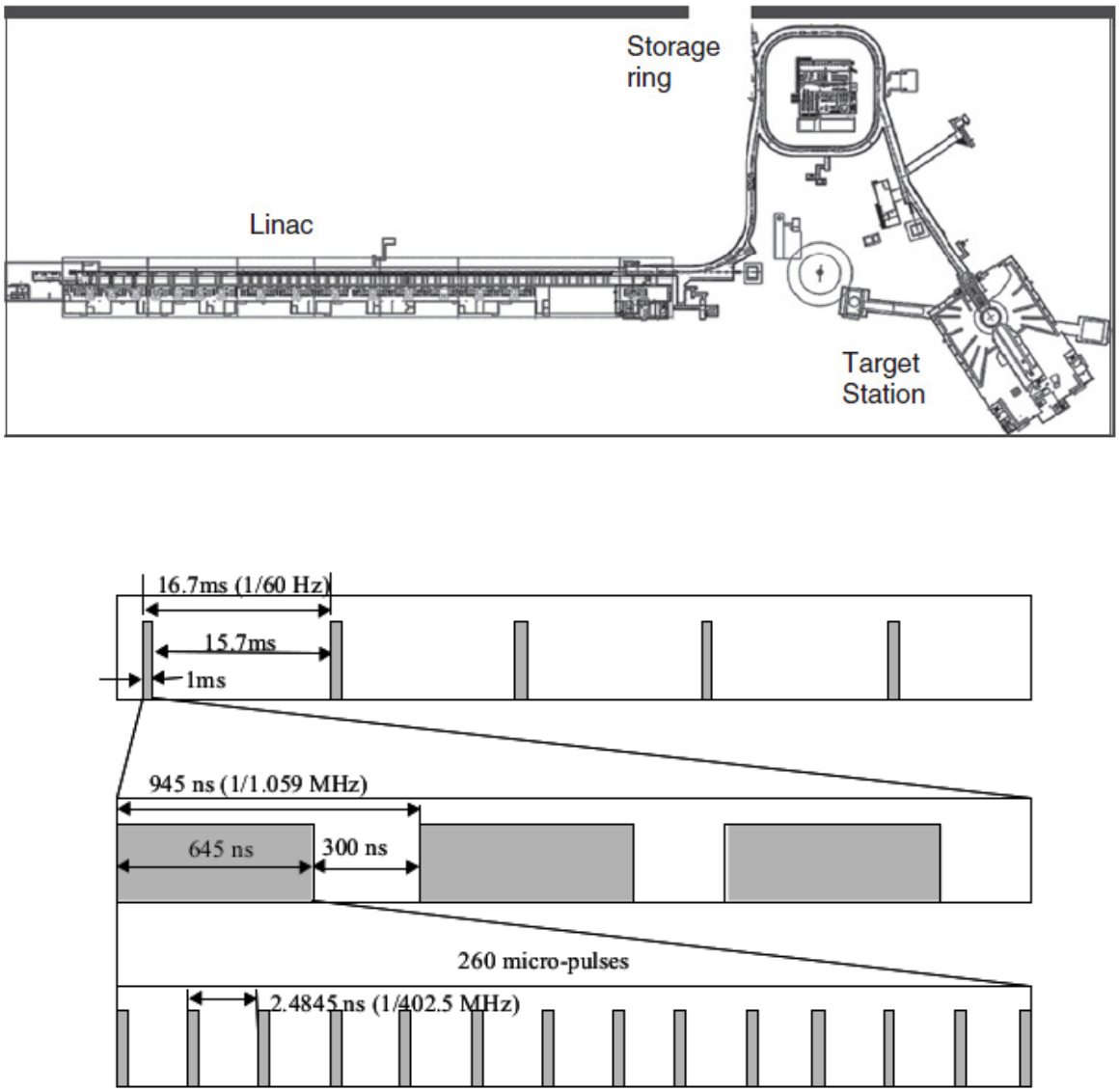

FIG. 2.3 The above figure shows a schematic representation of the SNS facility [AC+09]. The Figure below shows the time structure of the beam pulse at SNS: the macrostructure and microstructure of the pulse [Ale10].

on a intermittent basis. The intensity of the proton beam will be maintained for 1 minute and then turned off for 3 minutes. Since the beam will be shared with the beam line BL1A (which feeds another experiment), the separation between BL1A and BL1U will be defined by the kicker, which will be turned on $\sim$ 1 ms and then turned off for several ms to feed BL1U and BL1A, respectively [Dav13].

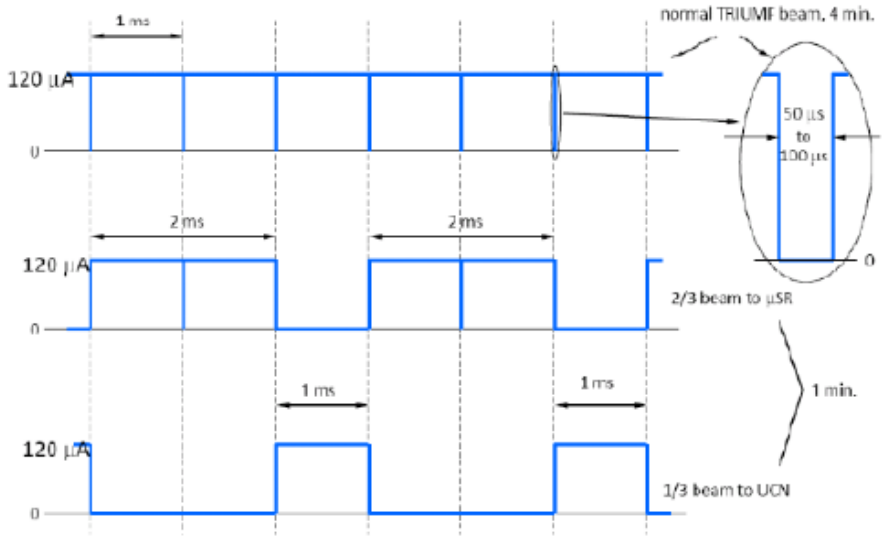

FIG. 2.4 A schematic representation of the time–base sharing of the proton beam at TRIUMF for beamlines BL1A and BL1U [Dav13].

PSNS	Type of accelerator	Current	Beam power
KEK-RCNP He–II Spallation UCN Source [Mat13]	392 MeV ring cyclotron	1 μA	400 W
TRIUMF (planned)	500 MeV synchrotron	40 μA	20 kW
SNS [Ale10]	1 GeV linac + acc. Ring	1.4 mA	1.44 MW
European Spallation Source (ESS) [HB212]	2.5 GeV (linac)	50 mA	5 MW

TABLE 2.1 General characteristics for Pulsed Spallation Sources.

Some other PSNS around the world are summarized in Table 2.1.

Both the proton energy and the target type play important roles in the design of spallation sources, since more neutrons are liberated for higher proton energy and the production cross–section depends on the target nuclear mass and other target material properties. The number of neutrons produced per incident proton can be estimated for several target materials using Fig. 2.5 [Tes85], constructed from

measured values, with an error in the results around ±20%. The graph shows that, for every material, the value of the neutron yield for energy values between 50 and 500 MeV, is proportional to the square of the proton energy (E_p^2). However, the behaviour of the curves change at 1000 MeV, where the proton energy is directly proportional to the E_p [Tes85].

For example, the neutron yield values for Lead (Pb) and Tantalum (Ta) targets are shown in the indicated curve in Figure 2.5. From there, the number of neutrons produced by an incident proton energy of 500 MeV (the value corresponding to the planned experiment at TRIUMF) in a lead target is around 6.7 n/p.

2.1.2 Neutron Production at TRIUMF

The tungsten target for neutron production via spallation will be located in the Meson Hall at TRIUMF. The proton beamline BL1U will be used to deliver protons from the cyclotron to the tungsten target as shown in Figure 2.6. This target will be comprised of 4 rectangular blocks (2cm, 2cm, 3cm and 5cm length), resulting in a target with total cross section around 6×8 cm^2 and length of 12 cm[1] [C15]. A yield of 7 neutrons per proton (see Figure 2.5) is expected for this target. The neutron moderation and generation of UCN is described in the following sections.

[1]This length corresponds to the approximate stopping length of protons in tungsten.

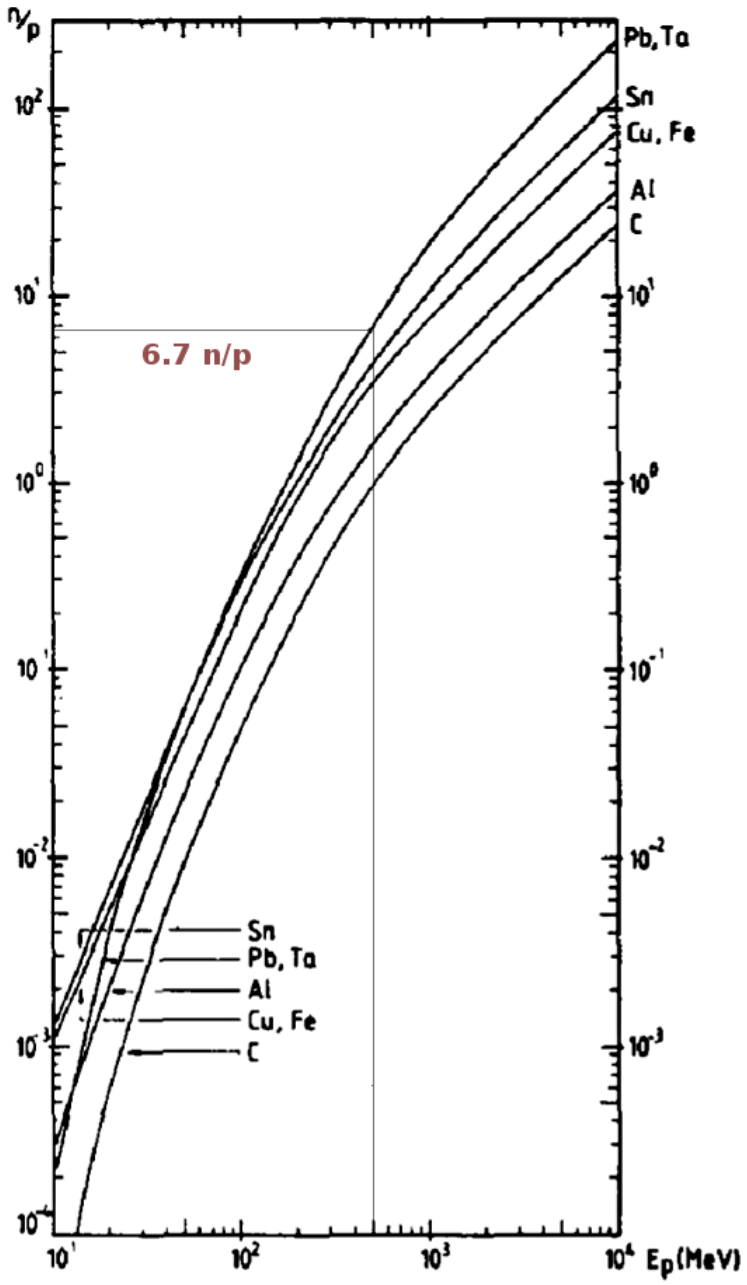

FIG. 2.5 Neutron yield for several target materials [Tes85]. The x–axis corresponds to the kinetic energy of the incident proton in MeV, and the y–axis to the ratio of neutrons produced for each incident proton on a logarithmic scale.

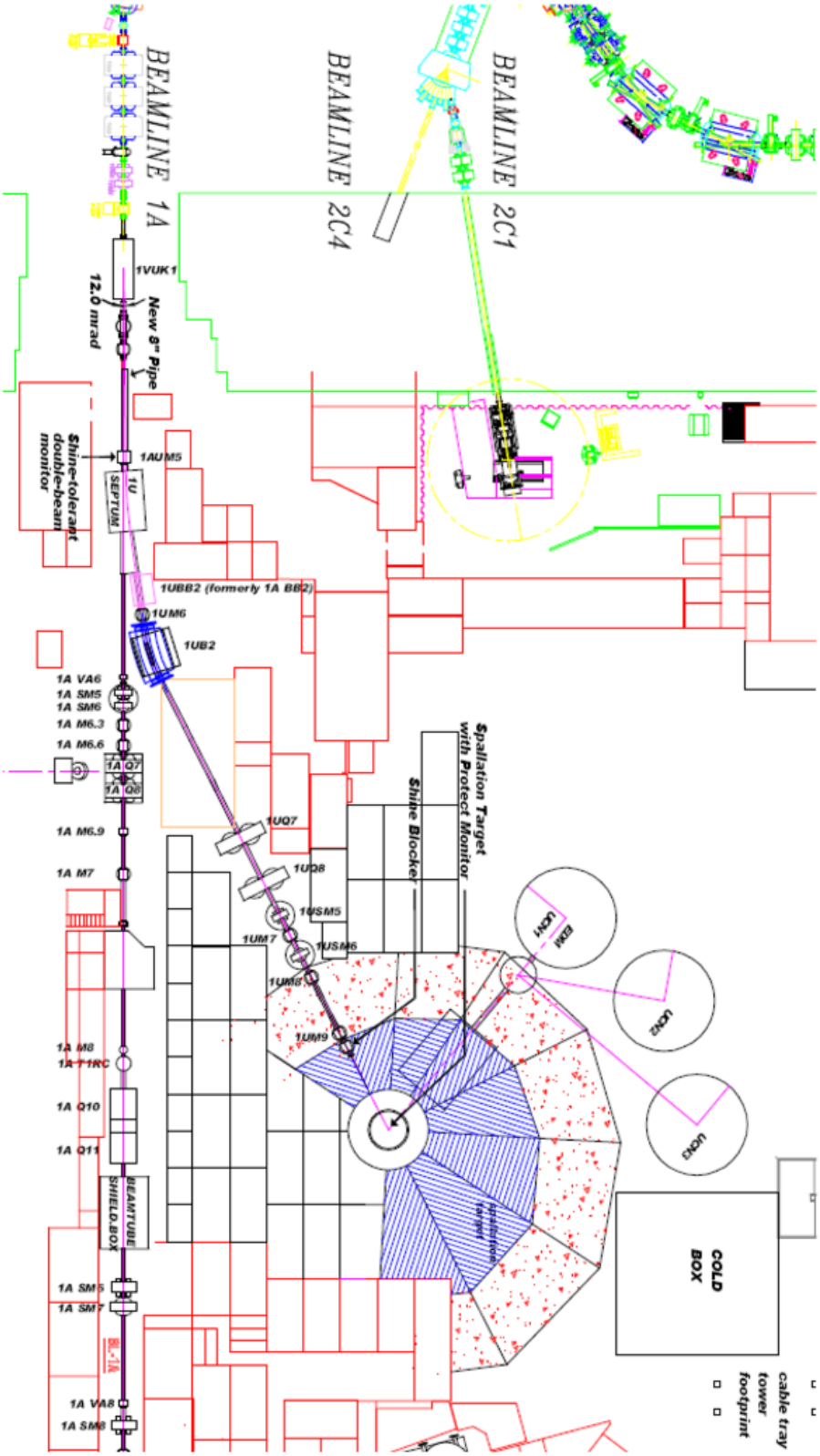

FIG. 2.6 A schematic view of the proposed UCN neutron facility in the TRIUMF Meson Hall [C15].

2.2 Physics of cold neutron production

2.2.1 Moderation process

For the measurement of the neutron EDM, ultra-cold neutrons are required since these can be easily stored for studies of the spin precession. Neutrons generated from the spallation process have energies around a few MeV and, therefore, have to be slowed down in order to produce UCN. When the energy of a neutron is low ($\leqslant 30$ meV) its wavelength is around a few angstroms ($1\ \mathring{A} = 10^{-10}$ m), and the optical properties of these particles become relevant [KL97]. At these low energies, neutrons can be reflected from surfaces, under the right conditions, allowing them to be transported and trapped in material containers.

Neutrons are slowed down by scattering from nuclei in a process called moderation. For lower energies, a superthermal process is required to generate UCN, which will be discussed in section 2.3. A moderator is a medium in which neutrons lose energy by repeatedly colliding with nuclei, atoms or molecules in the environment, until the neutrons reach thermal equilibrium at the moderator temperature. For instance, to reduce the temperature of a neutron from $E_0 = 2$ MeV to $E = 1$ eV, a particular number of collisions will be required depending on the moderator material [Lam66]. Table 2.2 shows values for different moderators and the number of collisions required in each case.

Medium	H_2O	D_2O	Be	O	Fe	U
n	16	29	69	121	407	1730

Table 2.2 Approximate values of the number of collisions needed to slow down neutrons from an energy of 2 MeV to 1 eV in different moderator materials [Lam66].

Two of the most common thermal moderators are ordinary water (H_2O), and heavy water (D_2O). If these are at room temperature (T $\sim$ 290K), then thermal neutron energies can be obtained ($\sim$ 0.0254 eV). For cold neutrons, the most common moderator is liquid hydrogen (T $\sim$ 20K), and for ultra–cold neutrons the most common is liquid helium (T $<$ 1K). A good moderator must have the following properties: a large probability of scattering with a small probability of absorption, and a considerable energy loss per collision. These aspects will be discussed further in this section.

When the neutrons come to thermal equilibrium in the moderator, their speed distribution can be described as a Maxwellian distribution [GNS95]:

$$\mathrm{d}N(v) = \left(\frac{m}{2\pi kT}\right)^{\frac{3}{2}} \exp\left(-\frac{mv^2}{2kT}\right) 4\pi v^2 \mathrm{d}v \tag{2.1}$$

where k is the Boltzmann constant ($k = 1.3806488(13)^{-23}$ J/K [M+11]), T (K) is the absolute temperature of the moderator, m is the neutron mass and v is the neutron speed.

The most probable speed can be found by maximizing the expression $g(v) = \frac{\mathrm{d}N}{\mathrm{d}v}$, i.e., finding $g'(v)|_{v^*} = 0$. Then, the most probable speed is:

$$v^* = \sqrt{\frac{2kT}{m}} \tag{2.2}$$

As an example, we can find the most probable speed for a neutron moving in a moderator with a temperature of 20°C, using the relation above:

$$v^* = 2198 \text{ m/s}.$$

The mean square speed $\langle v^2 \rangle$ can be obtained as follows:

$$\begin{aligned} \left\langle v^2 \right\rangle &= \int_0^\infty g(v) v^2 \mathrm{d}v \\ &= \left(\frac{m}{2\pi kT}\right)^{\frac{3}{2}} \int_0^\infty \exp\left(-\frac{mv^2}{2kT}\right) 4\pi v^4 \mathrm{d}v \\ &= \frac{3kT}{m}. \end{aligned} \tag{2.3}$$

Using the value for the mean square speed $\langle v^2 \rangle$, the average energy of a neutron can be obtained from the classical formula for the kinetic energy:

$$\langle E_{\text{kin}} \rangle = \left\langle \frac{1}{2} m v^2 \right\rangle = \frac{3}{2} kT. \tag{2.4}$$

The speed distribution can be written in terms of the neutron energy by introducing the

definition for the kinetic energy into the expression (2.1). The result gives the Maxwellian neutron energy distribution, as:

$$\mathrm{d}N(E) = \frac{2\pi}{(\pi kT)^{3/2}} \mathrm{e}^{-\frac{E}{kT}} \sqrt{E} \mathrm{d}E \tag{2.5}$$

Maxwellian speed and energy distributions for a neutron are shown in Figure 2.7. Speeds (2.2) and (2.3) are marked on the graph.

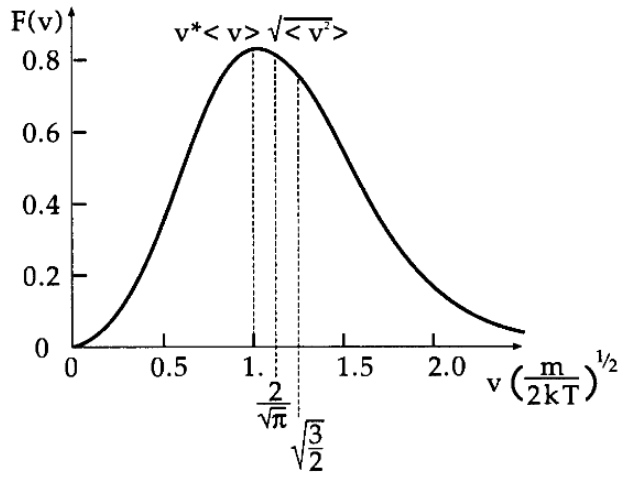

FIG. 2.7 Maxwellian speed distribution. In the graph, $v^* < \langle v \rangle < \sqrt{\langle v^2 \rangle}$ [GNS95].

Figure 2.8 shows the energy distribution of thermal neutrons (temperature T = 293K) from the moderation process, described by equation (2.5). According to expression (2.4), $\langle E_{\mathrm{kin}} \rangle \propto T$. To reach average energies corresponding to ultra cold neutrons (neV), one would therefore need to go to a moderator temperature of ~ 0.4 mK. This is not practical, so one must use a non thermal approach for the last stage of cooling. Ultra-cold neutrons can be produced either from the Maxwellian spectrum low energy tail or through a superthermal process. In the experiment at TRIUMF, a superthermal source is proposed to generate UCN by phonon scattering of cold neutrons in superfluid helium (He-II). This last part of UCN production will be discussed in more detail in section 2.3.1.

As previously mentioned, a good moderator must have a large probability of scattering

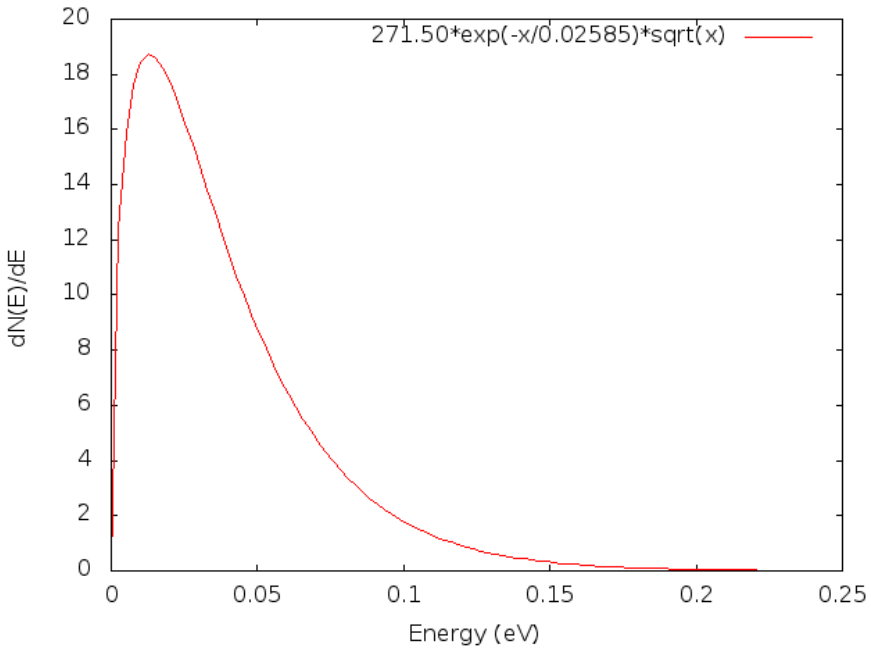

FIG. 2.8 Maxwellian energy spectrum for the number of neutrons per unit energy interval at room temperature.

with a small probability of absorption, and a considerable energy loss per collision. Thermal moderators containing light nuclei, for example, liquid hydrogen (LH_2) and liquid deuterium (LD_2) are good choices. Neutrons are slowed down more efficiently by protons due to the small difference of mass between protons and neutrons, making the use of moderators with a high density of protons more convenient [Car90]. Water moderators (H_2O) are used as a reference point with a proton density of 6.7×10^{28} protons/m^3 [Car04].

A neutron colliding elastically with a moderator nucleus (initially at rest) loses an amount of energy ΔE depending on the mass of the moderator nucleus and the incoming energy and collision angle. Typically, a relatively large number of collisions is required to achieve a significant energy loss starting with $\sim$ MeV neutrons.

The average logarithmic value of the energy decrement per collision (ξ) is defined as [BRS05]:

$$\begin{aligned} \xi &= \left\langle \ln\left(\frac{E_i}{E_F}\right)\right\rangle \\ &= 1 + \frac{(A-1)^2}{2A}\ln\frac{A-1}{A+1}, \end{aligned} \tag{2.6}$$

where E_i and E_F are the initial and final neutron energies ($E_i > E_F$) and A is the mass number of nuclei of the moderator.

The average number of collisions (n) required to slow down a neutron from an energy E_0 to E_F ($E_0 > E_F$) in terms of the equation (2.6), is given by the following expression:

$$n = \frac{\ln\left(\frac{E_0}{E_F}\right)}{\xi}. \tag{2.7}$$

As an example, the mean number of collisions required to thermalize a neutron from an energy of 2 MeV to 0.025 eV is $n = 25$ when the moderator is deuterium (using expression 2.7 with $A = 2$).

Cold neutrons are produced by down–scattering thermal neutrons to lower energies in a cold moderator, which is kept at cryogenic temperatures. Some typical moderator materials used for cold neutron production are liquid L_2 and D_2, solid methane and solid D_2O [CCK15].

2.2.2 Cold Neutron Production at KEK–RCNP

The experiment at TRIUMF will be developed in two stages. In the first one, a prototype of the experiment will be designed and carried out at the Research Center for Nuclear Physics (RCNP) in Japan. Later, the experiment will be upgraded after being moved to the facility at TRIUMF where the measurement of the neutron EDM will be performed to higher precision. A schematic representation of the UCN source at RCNP is shown in Figure 2.9.

The ultra–cold neutron production at the KEK–RCNP He–II spallation UCN source

is performed in two stages [Mat13]: a spallation process and a moderation process. For the spallation neutron production, a proton beam of 392 MeV and a maximum current of 1 μA collides with a lead target, which is a block of dimensions $100\times100\times200$ mm^3, liberating neutrons. Neutrons liberated from the lead target have energies of a few MeV and these are cooled to thermal energies by a heavy water moderator D_2O at 300 K, placed in an Aluminum bottle. There is a graphite reflector surrounding the lead target and the moderator to reflect neutrons that would otherwise escape, thereby increasing the flux of neutrons to the moderator.

For cold neutron production, thermal neutrons are moderated by a solid D_2O moderator whose temperature is kept at 20 K by a SRD–220 GM refrigerator [Mat13]. The material of the bottle in which the cold D_2O moderator is contained is also Al, and is placed above the thermal moderator, as shown in the schematic set–up in Figure 2.9. Lastly, cold neutrons are converted into ultra–cold neutrons in the He–II bottle (see subsection 2.3.1) and guided through the UCN guide to the UCN detector.

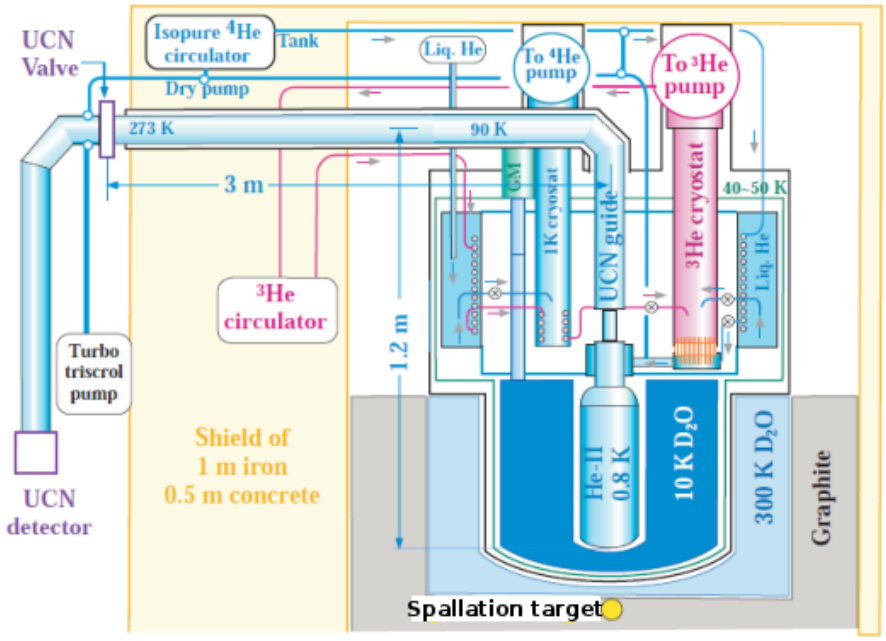

FIG. 2.9 A schematic representation of RCNP facility for UCN production [Mat13].

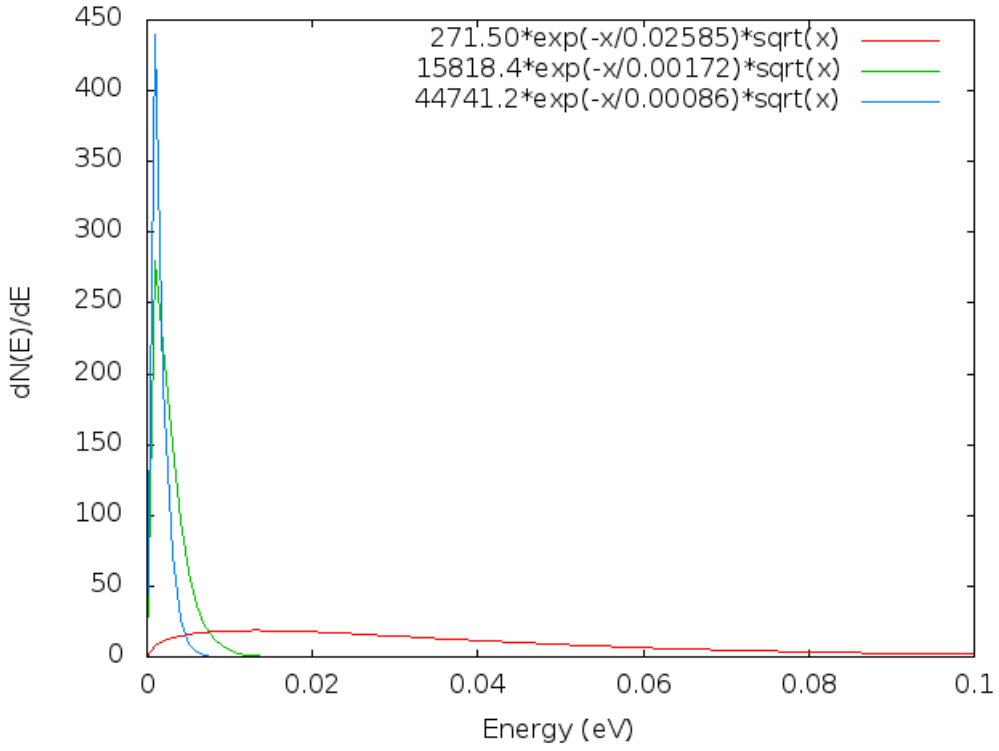

FIG. 2.10 Energy spectra for the number of neutrons per unit energy interval in the 300 K (red), 20 K (green) and 10 K (blue) moderators.

Energy spectra for moderators at 300 K, 20 K and 10 K are shown in Figure 2.10; these are the temperatures for moderators at RCNP and TRIUMF. For 300 K the spectrum is similar to that obtained for thermal neutrons in Figure 2.8. However, when the temperature decreases, the peak of the energy distribution is moved toward the lower energy side of the spectrum, as shown in Figure 2.10. Furthermore, the distribution becomes narrower for temperatures as low as 10 K and 20 K.

2.2.3 COLD NEUTRON PRODUCTION AT TRIUMF

The new facility at TRIUMF will use a new design concept which has been developed at RCNP. This involves a horizontal extraction of the UCN neutrons as shown in Figure 2.11. For cold neutron production, a two stage procedure will be implemented, as previously described for the prototype experiment at RCNP: neutron moderation in heavy water at

300 K and 20 K.

For cold production at TRIUMF, it is expected to increase the power of the incident beam up to 50 times compared with the upper limit of 400 W (1 μA $\times$ 392 MeV) at RCNP. The heat deposited at this power (see Table 2.3), is dissipated in the prototype experiment by a cryostat with a cooling power capacity which is ten times larger than the required at RCNP. This will ensure that the heat generated in the experiment at TRIUMF is dissipated [Mat13].

Eventually, it is planned to replace the 10 K D_2O cold moderator by a 20 K liquid D_2 (LD_2) moderator [C15]; this will improve the cold neutron flux which in turn will increase the UCN production, while decreasing the heating associated with the beam.

2.3 Physics of ultra–cold neutron production

2.3.1 Superthermal UCN production in He–II

The superthermal process can be used to produce UCN from cold neutrons in a down–scattering process, in which neutrons lose their energies by inelastic scattering [Kas04]. Golub and Pendelebury in 1977 [GP77], studied for the first time the mechanism of production of ultra–cold neutrons in superfluid ^{4}He. Their idea was to consider two energy levels for the moderator, an excited and a ground state, with an energy gap between these

		Power deposit (W)
300K D_2O	Vessel (Al)	69.2
	D_2O	264
	Sum	333.2
20K D_2O	Vessel (Al)	46.4
	D_2O	219.2
	Sum	265.6
He–II	Vessel (Al)	3.6
	He–II	1.6
	Sum	5.2

Table 2.3 Heating power expected to be deposited by the 20 kW beam at TRIUMF [C15].

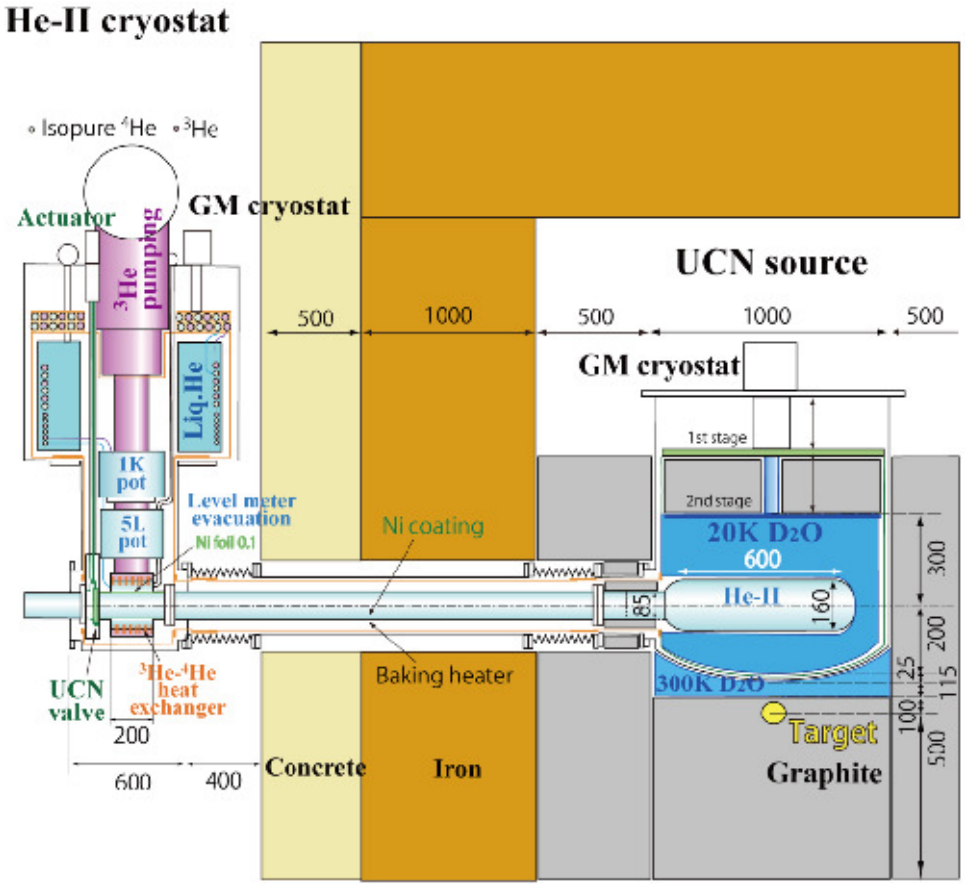

FIG. 2.11 A schematic representation of the neutron production set–up at TRIUMF [Tri16].

denoted by Δ. Consider a moderator, for an incident neutron with energy $E = E_{\mathrm{UCN}} + \Delta$ interacting with a spectrum of elementary excitations in the superfluid. Under the right kinematic conditions, the latter will absorb an amount of energy Δ creating a phonon, while the neutron is down–scattered to the UCN energy range. However, it is also possible to have a situation where an UCN gains an amount of energy Δ from the moderator, and this is referred to as an up–scattering process.

Both processes can be described, in a general way, with the principle of detailed balance (see for details [GRL91]) as follows:

$$E\mathrm{e}^{-\frac{E}{k_{\mathrm{B}}T}}\sigma(E \to E') = E'\mathrm{e}^{-\frac{E'}{k_{\mathrm{B}}T}}\sigma(E' \to E).$$

where E is the incident energy of the neutron, E' its final energy, k_{B} is the Boltzmann

constant, T is the temperature, and $\sigma(E \rightarrow E')$ and $\sigma(E' \rightarrow E)$ are the downscattering and upscattering cross–sections, respectively. At low temperatures the upscattering term in the expression above will be very small, leading to a net production rate of ultra–cold neutrons.

When the system reaches steady state, the rate of UCN production ($[P] = \frac{UCN}{cm^3 s}$) will be proportional to the density of UCN:

$$\rho = P \cdot \tau,$$

where the loss rate $1/\tau$ is a sum of partial rates ($1/\tau_i$) for individual loss mechanisms such as up–scattering by phonons in He–II and the absorption by ^{3}He.

The UCN production via phonon scattering is generated via a cold neutron interacting inelastically with a phonon in superfluid helium. After the scattering process, there is a change in the energy and momentum of the cold neutron, given by the expression $\hbar\omega = E - E' = \frac{\hbar^2}{2m}(k^2 - k'^2)$ where $\hbar\omega$ is the energy of the phonon. The relation between energy and momentum can be represented by a dispersion curve. Figure 2.12 shows the measured dispersion curve (energy versus wave number where $p = \hbar k$) for phonon excitations in superfluid He–II. For neutrons, the dispersion curve is a parabola: $E = \frac{\hbar^2 k^2}{2m}$. The condition in which UCN are generated through the creation of phonons is satisfied at the point in phase space where the dispersion curve for He–II is intersected by the dispersion curve for a free neutron [Mat13]. Then, using the experimental information in Figure 2.12 from D.M. McKinsey [McK02], this condition will be satisfied for $k_\mathrm{i} = 0.706$ Å^{-1} and $\lambda = \frac{2\pi}{k_\mathrm{i}} = 8.9$ Å [LG93].

2.3.2 KEK-RCNP Superthermal Production in He-II

The value of the UCN density at the experimental port was calculated at KEK (see for a detailed description, the analysis made by Matsumiya in [Mat13]). This led to a UCN density value of 15.3 ± 1.1 $\frac{\mathrm{UCN}}{\mathrm{cm}^3}$. After several improvements in the experimental setup the lifetime of trapped UCN was improved, which also resulted in a higher density, as will

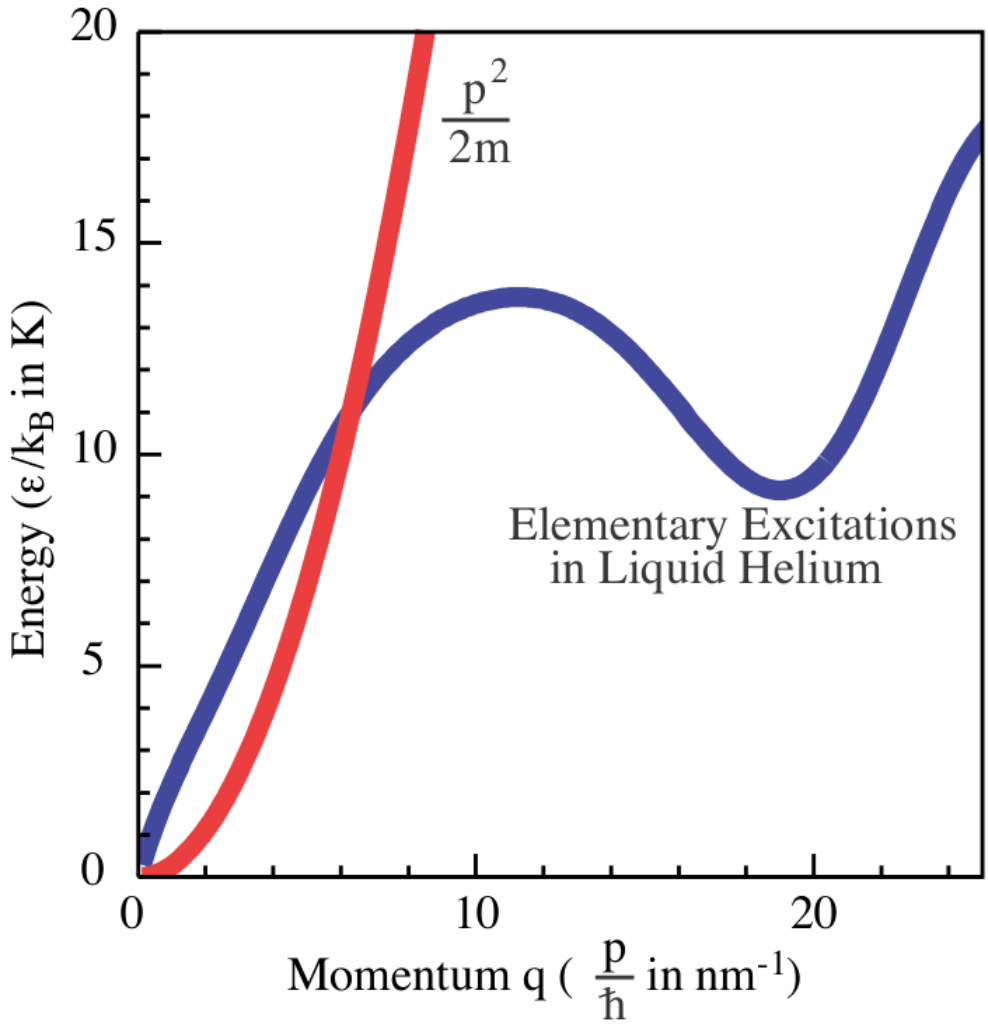

FIG. 2.12 Experimental dispersion curve for one-phonon excitations [McK02].

be discussed in the following subsection.

2.3.3 SUPERTHERMAL PRODUCTION IN HE–II AT TRIUMF

UCNs will be produced at TRIUMF using the method previously described for the prototype experiment at RCNP. After UCN production, the heat in the He-II bottle will be removed through a heat exchanger by ^{3}He pumping in the cryostat, reaching temperatures below 1K; the goal is to reduce the temperature in the He–II bottle to 0.7 K. Once this limit is reached, the *UCN valve* (see Figure 2.11) will be opened and ultra–cold neutrons

will be conducted to the next part of the experiment.

2.3.4 UCN Storage time

The storage time is an important factor for UCN, which depends on a number of factors. UCN production is increased when the number of neutrons from the spallation source is increased, which requires a higher power of the primary proton beam. The latter will increase the gamma heating which, in turn, will raise the temperature inside the He-II bottle. This will increase the number of phonons, which, in turn, will increase the phonon-UCN collision rate, reducing the lifetime of neutrons inside the He-II bottle. This last can be solved by implementing a He-II heat exchanger in the experiment to extract the heat from the bottle. The UCN storage time dependence on phonon up-scattering is inversely proportional to the seventh power of the temperature (see Appendix A) [C15]:

$$\tau \propto \frac{1}{T^7}$$

At temperatures of 0.8 K and 0.7 K the expected storage times are 600 s and 1370 s, respectively. Other additional factors constraining the total lifetime of UCNs are: the intrinsic neutron lifetime (τ_β =880 s), absorption by ^{3}He, loss per bounce at the walls, and up-scattering by phonons in the moderator. The storage lifetime in the bottle is obtained from the addition of these contributions, as follows:

$$\tau = \left(\frac{1}{\tau_{\mathrm{ph}}} + \frac{1}{\tau_{\mathrm{w}}} + \frac{1}{\tau_{^3\mathrm{He}}} + \frac{1}{\tau_\beta} \right)^{-1}$$

An estimated storage time of 174 s at 0.8 K [Mat13] was calculated from the expresion above; the goal at TRIUMF has been set to 100 s [C15].

After improvements in the current UCN experiment at RCNP (see Appendix B), and with the use of the ^{3}He cryostat, the final storage lifetime reached was 81 s for a temperature of 0.8 K. Under these conditions, a UCN density of 26 UCN/cm^3 was obtained, corresponding to a production rate of 4 UCN/cm^3/s. The goal with the new experiment at TRIUMF is to reach a UCN density of 800 UCN/cm^3, which corresponds to

an increase by a factor of 50 in the production rate of UCN compared with the prototype at RCNP (P $\sim$ 200 UCN/cm^3/s). A summary of achieved and planned values are shown in Table 2.4.

Experiment	τ (s)	T_{HeII} (K)	Density ($\frac{UCN}{cm^3}$)	Production rate ($\frac{UCN}{cm^3 s}$)
RCNP	81	0.8	26	4
TRIUMF	100	0.7	800	200

TABLE 2.4 Key trapping parameters obtained at the RCNP UCN source and expected values at the new facility at TRIUMF.

3

TRIUMF EDM MEASUREMENT AND UCN DETECTION

3.1 UCN EDM MEASUREMENT STRATEGY

At TRIUMF, ultra–cold neutrons will be produced in a process comprised of three stages: spallation, moderation in D_2O and downscattering in superfluid helium. In the spallation process, a proton beam of 400 MeV collides with a tungsten target liberating neutrons with energies on the order of MeV (see section 2.1). These neutrons will be slowed down in D_2O at 300K to thermal energies, and then converted into cold neutrons by moderation in D_2O at 10K (see section 2.2). The experimental set–up for UCN production at TRIUMF was described previously in subsection 2.2.3. Figure 3.1 shows the He–II bottle in which cold neutrons will be down scattered to UCNs by phonon production (see section 2.3). The temperature in the bottle is expected to be kept at 0.7K. After the UCN production, the UCN valve (which keeps the UCN confined in the bottle) will be opened, and UCNs will be guided through a horizontal UCN guide, and then through the rotary valve, to the EDM cell (see Figure 3.1), where the nEDM experiment will be performed.

For the measurement of the neutron EDM, the Ramsey separated oscillatory field resonance method will be used [Ram82]. In this process, a neutron precesses in weak and strong magnetic and electric fields, as previously described in section 1.1.4. The current EDM apparatus at RCNP will be transported to TRIUMF and used for Phase I of the neutron EDM measurement at this facility [C15]. Figure 3.1 shows a schematic diagram of the experimental set–up where the main components are marked. The spherical B_0 coil contains the EDM cell, which is in the presence of a homogeneous magnetic field and a strong electric field; four magnetic shields are used to shield the EDM cell from external

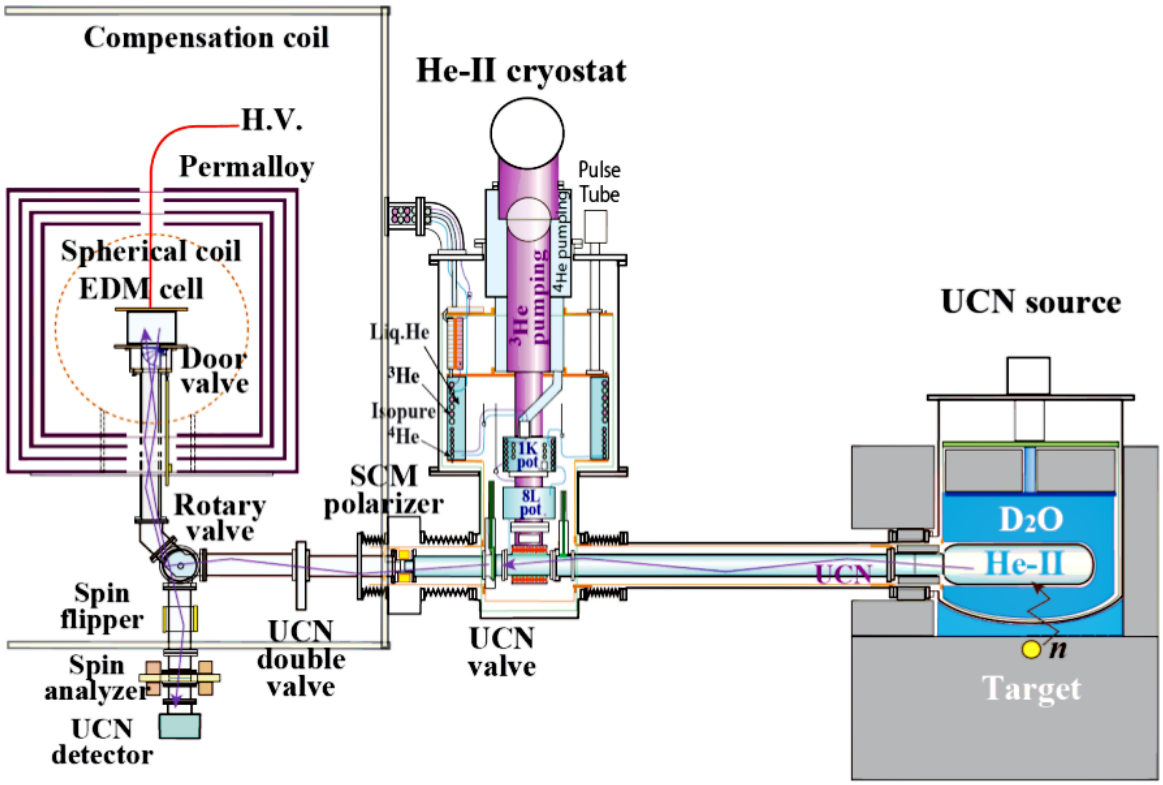

FIG. 3.1 Schematic representation of the experimental apparatus for the measurement of the neutron EDM at RCNP [C15].

magnetic fields. After spin precession occurs, the door and rotary valves are opened (see Figure 3.1) and neutrons fall down passing through the spin flipper and the analyzer (see section 3.4), and are counted in the UCN detector. This chapter focuses on the UCN detector and the main characteristics of its components.

3.1.1 SCHEMATIC PROCESS IN THE DETECTOR

In general, a scintillation detector system consists of a scintillating medium, a light guide, a photomultiplier (PMT) and an electronic acquisition system to analyze the signal. Scintillator materials exhibit the luminescence property known as *scintillation*, as a result of ionizing radiation passing through them [Lia12].

Scintillators can be classified according to their composition as organic or inorganic, and the latter will be of particular interest in this work. Two advantages of inorganic

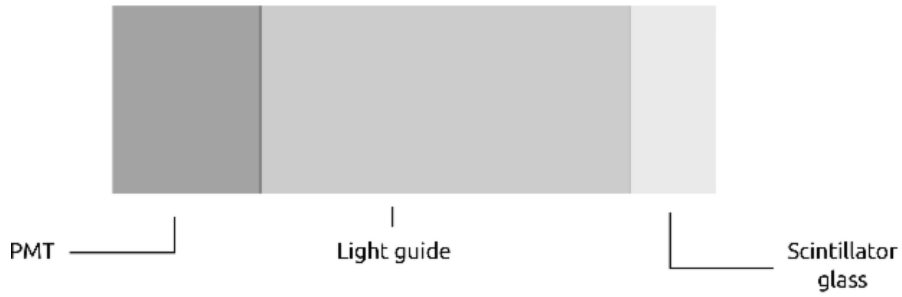

FIG. 3.2 Schematic representation of a scintillation counter. The detector in the TRIUMF EDM experiment consists of a glass scintillator, light guide and PMT.

scintillators are their higher radiation tolerance, and their light output that is larger compared to organic scintillators, which gives a better energy resolution. These materials can be adapted for neutron and gamma–ray detection.

In this work, neutrons are detected by means of ^{6}Li–doped glass scintillators, in which light is emitted after a neutron is absorbed by a ^{6}Li nucleus in the scintillator. When the neutron capture occurs, two secondary particles (t, α) are generated in the process with a specific kinetic energy. These particles will travel through the medium creating scintillation light, which can be collected by a photomultiplier.

^{6}Li is widely used as a neutron detector mainly due to its high neutron absorption cross section. Furthermore, the reaction products are relatively low energy particles with a large mass and are therefore, easily stopped in small amounts of materials, depositing all of their energy. An important issue will be the sensitivity to gamma-rays, which may be mitigated by implementing an adequate discrimination method.

3.1.2 INORGANIC SCINTILLATORS

The following description for inorganic scintillators is based mostly on [Kno00]. The scintillation mechanism in inorganic scintillators is determined by the energy states of the crystal lattice in the material.

A schematic representation of the scintillation process is shown in Figure 3.3. The figure shows two energy bands: the conduction and valence bands. In the valence band, electrons are bound to the crystal lattice sites; when energy is absorbed in this band,

an electron near the top of the valence band, is elevated to the conduction band (where electrons are free to move through the crystal), leaving behind a hole. The gap between both bands is known as *band gap* and electrons are forbidden to exist in this area, in a pure crystal.

The electrons in the conduction band eventually decay back to the valence band emitting a photon, typically with an energy above the visible spectrum if the band gap is relatively large. In order to generate a larger number of scintillation photons, an *activator* is added to the material. These are small amounts of impurities which modify the internal energy band structure by creating regions (sites) in the lattice, where the band gap is reduced, while leaving the general band structure unaltered in the lattice. By doing this, the photons generated by electron transitions in the scintillation process will be emitted with a particular average or peak wavelength in the visible spectrum, which is specific to a particular dopant.

When a charged particle passes through the material, a large number of *electron–hole* pairs are created. The electrons are excited into the conduction band, while the holes in the valence band drift to the activator sites and ionize them. The free electrons will combine with the ionized activators, resulting in a neutral, activator state which decays to the ground state and the de–excitation process will then generate a photon (this occurs promptly with a high probability of photon emission which is known as *fluorescence*) in the visible range depending on the dopant.

3.1.3 Neutron cross section

Neutron interactions can be classified in two categories: scattering and absorption. In the scattering process the neutron and the nucleus reappear after the reaction, and the scattering can be elastic or inelastic. In the absorption process the neutron combines with the nucleus, to form a new nucleus; another isotope. This new isotope is called a compound state, because it exists in a very high energy state. The compound state usually decays via gamma emission to some stable beta, alpha or unstable nucleus, which then further decays. In some cases, the compound nucleus breaks up, such as the case of

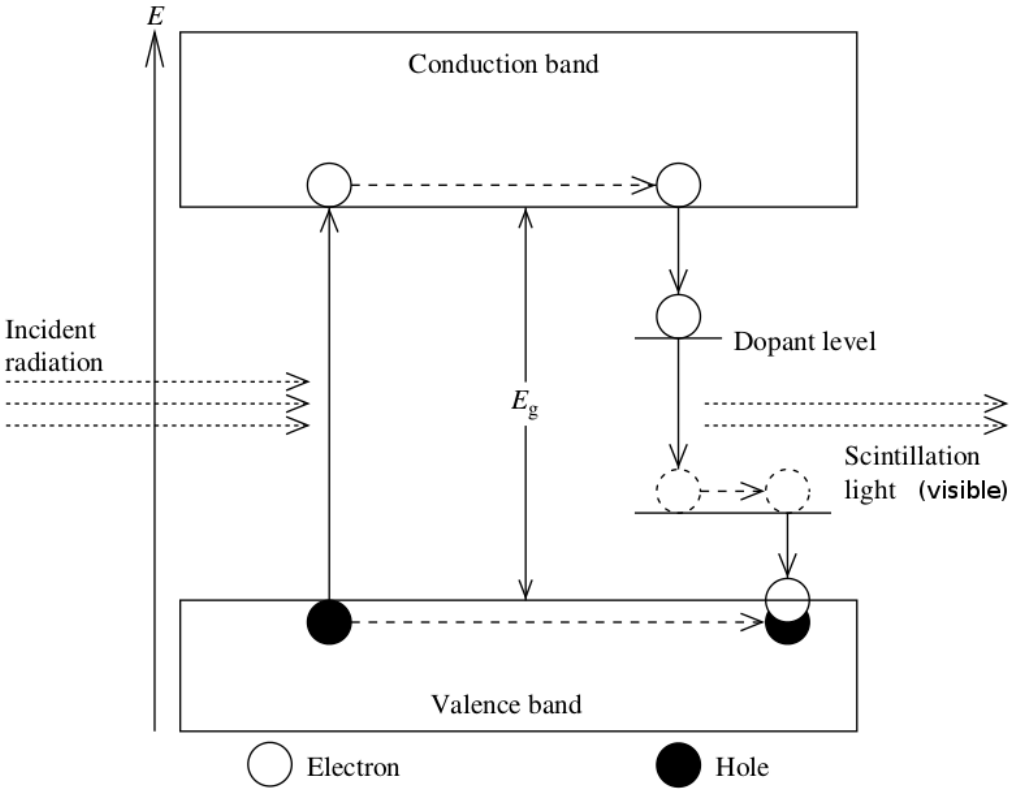

FIG. 3.3 Diagrammatic representation of energy levels of an inorganic scintillator with an activator [Nae07]. Scintillation light in the visible spectrum is emitted in the process.

^{6}Li that forms a ^{7}Li isotope from a neutron capture, which decays into an alpha particle and a triton.

The probability of a neutron to interact with a nucleus is described in terms of the cross section (σ) of the neutron–nucleus interaction. This quantity depends on the energy of the neutron and the type of nucleus involved in the reaction (Figure 3.4). The cross section corresponds to the effective area presented by the nucleus to the interacting neutron, so it has dimensions of area, and its unit is barns (b), where

$$1 \text{ barn} = 10^{-28} \text{ m}^2.$$

Taking into account that the nuclear radius is between 10^{-15} and 10^{-14} meters, the geometrical cross–sectional area of a nucleus is around 1 barn.

For neutrons interacting with nuclei, the probability of being scattered or absorbed is defined in terms of microscopic cross sections such as the elastic scattering cross section σ_{el}, the inelastic scattering cross section σ_{in}, the fission cross section σ_{f}, and the capture cross section σ_{c}. Therefore, the addition of these terms accounts for the total probability that any interaction takes place between a neutron and nucleus:

$$\sigma_{\mathrm{T}} = \sigma_{\mathrm{el}} + \sigma_{\mathrm{in}} + \sigma_{\mathrm{f}} + \sigma_{\mathrm{c}} \ldots$$

The attenuation of neutron flux (particles/area/time) through a thickness x of a volume of material with cross–section σ_T and nuclear density N (m^{-3}), is given by

$$\mathrm{I}(x) = \mathrm{I}_0 \mathrm{e}^{-N\sigma_T x} \quad ,$$

where I_0 is the incident flux and $\mathrm{I}(x)$ is the flux transmitted a distance x through the volume. In this case, the volume corresponds to a detector.

The rate of reactions taking place in the detector can be obtained by multiplying the total loss of flux of the incoming particles by the cross-sectional area, A:

$$\mathrm{R} = \mathrm{I}_0 \left(1 - \mathrm{e}^{-N\sigma_T x}\right) \mathrm{A}$$

In the case of a thin target, the exponent in the expression above is very small ($N\sigma_T x \ll 1$), and therefore, the number of neutron–nucleus interactions taking place in the material per unit area for a beam of neutrons traversing the target is:

$$R = \mathrm{I}_0 \mathrm{N} \sigma_T x \tag{3.1}$$

The detection of neutrons is only possible indirectly, by means of the secondary charged particles produced after neutrons are absorbed. The energy released after neutron capture can be measured directly, because several MeV of energy are liberated in the form of kinetic

energy of the secondary particles. The most common neutron detection reactions are:

$$^{3}\mathrm{He} + \mathrm{n} \rightarrow {}^{3}\mathrm{H} + \mathrm{p} + 0.8\ \mathrm{MeV}$$
$$^{6}\mathrm{Li} + \mathrm{n} \rightarrow {}^{4}\mathrm{He} + {}^{3}\mathrm{H} + 4.8\ \mathrm{MeV}$$

The first reaction above is commonly used in gas proportional counters while the second one is convenient for use in scintillator detectors.

Figure 3.4 shows the absorption cross sections (σ_a) for the reactions mentioned above. At low energies, these cross sections are inversely proportional to the velocity: $\sigma_a \propto \frac{1}{v}$. Therefore, in this region the cross section will also be inversely proportional to $\sqrt{E}$, since the kinetic energy $E = \frac{1}{2}mv^2$. A physical interpretation of this law ($1/v$ law) is summarized by B.T.W. Wilis and C.J. Carlile (2009) [WC09] as: "*the slower the neutron, the longer the dwell time near the nucleus and the higher the probability of absorption*".

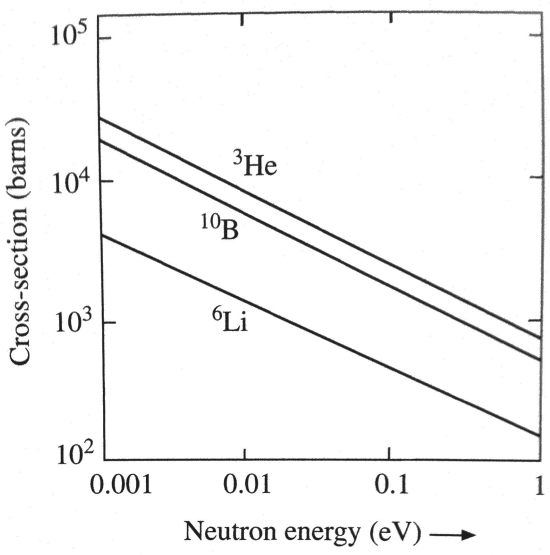

FIG. 3.4 Neutron absorption cross section for low energy neutrons with ^{3}He, ^{10}B and ^{6}Li nuclei [WC09].

3.2 Lithium glass

New techniques for UCN detection have been the result of an adaptation of current thermal and cold neutron detection techniques, which are based on elements with high absorption and low scattering cross-sections such as ^{3}He,^{6} Li and ^{10}B. These new detectors must have a fast response time in order to detect UCNs at high event rates (>MHz) [BBL+09]. This property will be of particular interest for the detector in this work, since the world's highest density of UCN is expected in the new source at TRIUMF, which will lead to an expected rate in the detector of $3.3\times10^{6}\,\frac{\mathrm{UCN}}{\mathrm{s}}$ [C15]. Other requirements that this detector must satisfy are [BFL+05]:

1. Detection of neutrons should be accomplished with high efficiency, which should take into account factors such as edge effects and electronic aspects (e.g. signal to noise ratio).

2. The efficiency of the detector must be stable over time.

3. The detector must have low background sensitivity to photons; the system should be able to discriminate between neutrons and gamma-rays, which is the main background in the detector region.

4. The detector should have an appropriate radiation hardness[1] to prevent the detector performance from deteriorating (the electronics primarily becomes noisy and the signal amplitude will decrease because the transmission of optical light decreases with radiation damage) over the lifetime of the experiment.

The scintillators of particular interest in this work (type GSx [AST14]) were developed by Applied Scintillators Technology (AST). The composition of the types of glass used is Ce_2O_3, SiO_2, MgO, Al_2O_3 and Li_2O oxides; the cerium is used to activate the scintillators in the 6-Lithium glass and, as a result, the emission spectrum of light will have a defined peak related to the sites of Ce^{3+}. The main properties of the glass types GS10, GS20

[1] G. Ban et al. [BFL+05] found from radiation hardness tests with cold neutrons, that there were not measurable effects in GS20 scintillators for an absorbed dose lower than 1×10^{13}n/cm^3.

and GS30 are included in Table 3.1. The main difference between these materials is in their content of ^{6}Li: GS10 has a natural content of lithium-6 while GS20 and GS30

^{6}Li content	Glass type	^{6}Li fraction (atoms/m^3)	Refractive index	Relative light output (%)	Fermi potential (neV)
Depleted	GS30	6.4×10^{17}	1.58	100	104
Natural	GS10	1.8×10^{21}	1.55	85	85
Enhanced	GS20	2.2×10^{22}	1.57	85	107

TABLE 3.1 Fundamental properties of the Lithium–6 doped scintillator glasses. The values of the Fermi potential and critical velocity were calculated by G. Bal et al [BBL+09], using data on the neutron scattering lengths and the chemical composition of the glass scintillators.

are doped with and depleted with ^{6}Li, respectively. Two important characteristics of these scintillators are: the emitted light has a peak at 395 nm which avoids the need for wavelength shifters[2], and a short decay time $(60 - 75)$ ns which allows operation at high rates [BBL+09].

3.2.1 WORKING PRINCIPLE

A particular interest in the use of ^{6}Li–doped glass scintillators as UCN detectors is due to the high neutron capture cross-section, which allows a high detection efficiency. An ultra–cold neutron with an approximate energy of 300 neV will have a cross section around 172 kb which is obtained from extrapolating graph 3.4, using $\sigma \propto 1/\sqrt{E}$. This value for the cross section is so large that a physically thin detector with only a small percentage of Lithium-6 ($\rho(^6Li) = 1.8 \times 10^{21}\ cm^{-3}$ [BFL+05]) will effectively capture all UCN that hit the detector at normal incidence to the glass surface. The neutron capture by a ^{6}Li nucleus leads to the following reaction:

$$\mathrm{n} + {}^6\mathrm{Li} \rightarrow {}^3\mathrm{H}(2.74\ \mathrm{MeV}) + {}^4\mathrm{He}(2.05\ \mathrm{MeV}) \tag{3.2}$$

[2]This is a material which is used to increase the wavelength of the light emitted in such a way that it can match in a better way with the specifications of the photocathode in a photomultiplier [Tso15].

As a result of this reaction, an alpha ($^4He^{++}$) and triton ($^3H^+$) are created (for low energy neutrons the alpha and triton particles are emitted back to back) liberating in the process 4.78 MeV of energy, producing in turn a large amount of scintillation light [BBL+09]. The sensitivity to gamma rays which could mimic a neutron signal is reduced by making the detector thin, so that a typical electron from a compton scattering event escapes from the detector. The choice for our detector is 100μm GS20 bonded to 60μm GS30 glass. Measurements have not been made for this detector thickness; however we can safely assume an upper limit of around 2×10^{-3} probability for a gamma–induced false neutron signal based on measurements in reference [JC83] for a 1 mm detector.

3.2.2 The scintillator stack

When a neutron capture occurs inside a Lithium–6 doped scintillator glass whose thickness is large enough to contain the track length of the resulting particles (alpha and triton), the full energy is deposited inside the scintillator. However in the case of an *edge event* when the neutron is captured at or near the surface of the glass, an alpha or triton particle may leave the glass, and this produces a small amplitude signal. This incomplete energy deposition of the neutron is defined as an edge event, and the smaller associated signal may be comparable to electronic noise and gamma radiation. In order to minimize edge effects, two glass layers are attached together as shown in Figure 3.5 [Rog09], in which a Li-depleted glass (GS30) is placed above the enriched glass (GS20). Incident neutrons will pass through the GS30 (its ^{6}Li fraction is equal to 0.01% which makes it almost transparent to the UCN) and will be captured in the GS20 glass. In the case of an edge event, i.e., if a triton (range $\sim$ 37 μm) or an alpha particle (range $\sim$ 6 μm) escapes from the GS20, its energy will be deposited in the upper glass, and thus the total energy deposited by the neutron event can be detected.

In cases when only the GS10 or GS20 glasses are used, there is an incomplete energy deposition (edge effects) arising from the particles which not fully deposit their energy into the glass. A study of the light collection in these cases was performed by S. Hansen–Romu and B. Jamieson [HJ12a] and is briefly discussed in Appendix J.

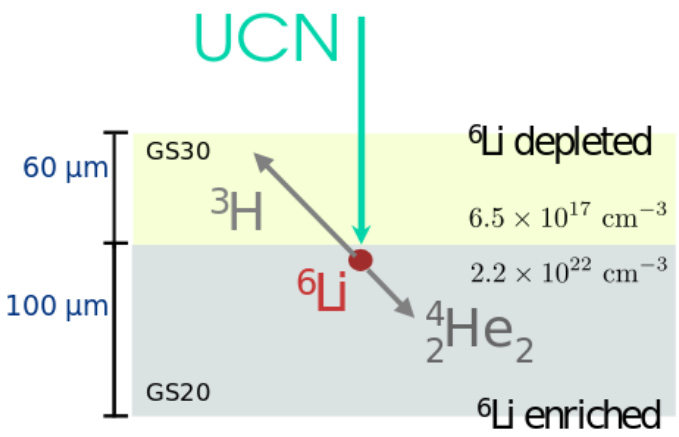

FIG. 3.5 A schematic representation of the GS30-GS20 stack showing an edge event taking place close to the interface between two glasses. Two particles are generated when a nucleus of Lithium-6 ($^6_3\mathrm{Li}_3$) captures a neutron: an alpha ($^4_2\mathrm{He}_2^{++}$) and a triton ($^3_1\mathrm{H}_2^{+}$). The energy of the alpha particle is fully deposited in the GS20 glass while the triton deposits its energy in the GS30 glass.

3.3 PROTOTYPE DETECTOR

3.3.1 BASIC DESIGN

The UCN detector at TRIUMF is being designed to detect ultra-cold neutrons with a high efficiency. This detector is composed of three main parts as previously mentioned: a scintillator, a light guide and a photomultiplier. A schematic design for each element of the prototype detector used in this work is presented in Figures 3.5, 3.8, 3.9 and 3.11, which will be discussed in the next sections.

3.3.2 SCINTILLATOR GLASS

The UCN detector consists of a stack of enriched and depleted glass layers (GS20 and GS30, respectively), as shown in Figure 3.5. The total thickness of the resulting scintillator[3] is 160 μm, and the layers are optically bonded.

[3]The thicknesses of the two types of glass are 60 μm and 100 μm for depleted and doped sides, respectively (see Section 3.4).

Some GS20–GS30 stack detectors were acquired by the UCN Detector Group from Applied Scintillation Technologies in the UK [AST15], for testing purposes. Since the two glass types are visibly identical, a means was developed to independently verify which side is which. Doped and depleted sides were identified as described in [JR15], by comparing the number of neutron capture events for both possible orientations of the glass stack. An excess in the events around the energies of alpha and triton particles was used to identify the ^{6}Li enhanced GS20 scintillator side of the glass stack (see Appendix I).

Some of the main properties of inorganic scintillators are mentioned as follows:

- **Light output**

  For an incident particle in a scintillator, only a small part of its kinetic energy is converted into visible light, which will depend on the energy and the type of the incident particle. The light yield is an important quantity for scintillator counters and is measured in photons per unit energy, such as Megaelectronvolts ($\frac{\text{photons}}{\text{MeV}}$). In this way, it provides a measure for the efficiency of the scintillator to convert the deposited energy into photons.

- **Time**

  An important factor in the scintillation process is the speed at which the crystal emits visible pulses after the absorption of a neutron or gamma ray. This is relevant since it determines the ability to discriminate sequential two scintillation pulses, which is useful when there are high event rates, and for Time–Of–Flight measurements [Kna12].

  The time profile of a typical scintillation pulse is comprised of two components: a part that increases rapidly (less than 1 ns), and a part which decays slowly (between few ns and several ms). Both parts can be modelled by a rise and decay exponential functions; the light output L in a scintillator is schematically indicated in Figure 3.6 [Nae07]:

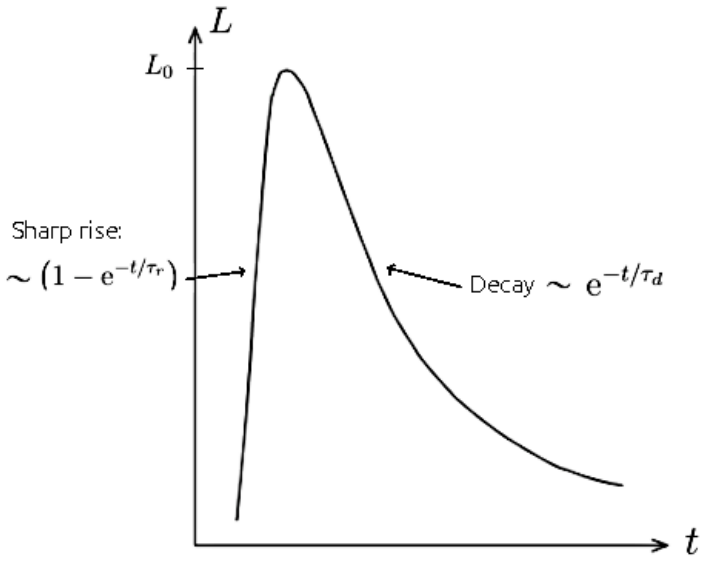

FIG. 3.6 Time profile of a typical scintillation pulse. Both parts in the pulse can be modelled by a rise and decay exponential functions [Nae07].

where τ_d and τ_r are the decay and rise times, respectively. Inorganic scintillators have a fast response; for instance the decay time for light output of 6–Lithium glass scintillators is between 60 and 75 ns.

- **Light collection**

  The light produced in the scintillator is not completely transmitted to the photomultiplier [Leo94]. This reduction of the light is caused by two processes occurring at the scintillator boundaries: absorption and loss of photons at boundaries. The absorption will depend on the attenuation length (l_{att}), which is the distance over which the intensity of the light has dropped by a factor equal to e^{-1}, and the distance along the length of the material of the light through the scintillator (x). The absorption process is described by the following equation:

$$\mathrm{I}(x) = \mathrm{I}_0 e^{-\frac{x}{l_{\text{att}}}},$$

  where I_0 corresponds to the incident intensity of the light.

  Inside the scintillator the light travels in all directions, and can be reflected or

transmitted at boundaries. For a photon incident upon a boundary between two materials, reflection occurs when the angle of incidence (θ_i) is greater than a critical angle (θ_c), where the latter is given by the following equation [Kno00]:

$$\theta_c = \arcsin\left(\frac{n_2}{n_1}\right). \tag{3.3}$$

In the relation above, n_1 and n_2 are the refractive indices of the scintillator and its surrounding medium, respectively. When the condition in equation (3.3) is satisfied, total internal reflection of the light takes place, and photons are confined to the scintillator. However, it is also possible that the incident light can have an angle of incidence smaller than θ_c. In that case, there is only a partial reflection, and the remaining light is transmitted to outside the scintillator and therefore lost.

3.3.3 Light guide design

- **General description**

  The scintillator and the photomultiplier can be coupled by means of a light guide or light pipe, which is used to guide the light to be detected. Light guides are characterized by a high index of refraction which minimizes the critical angle (θ_c), maximizing internal reflection at the boundaries of the guides. This allows a maximum transmission of the scintillation light. In the case of air–core light guides, the index of refraction is close to 1 and the light undergoes total external reflection upon encountering mirrored boudaries.

  For transparent solids as light guides, a reflective material is used to wrap the surface in order to avoid loss of light due to transmission to the surrounding medium. Some typical materials for light guides are [Nae07]: plexiglass, glass, clear plastic, fiberglass and liquid light guides.

  The shape of the light guide design is also important. In the ideal case, the light will be totally transmitted from the scintillator to the PMT, with a light guide whose cross-sectional area be constant and without sharp bends. In the case where

the light is transmitted from a bigger (A_{in}) to a smaller (A_{out}) cross-sectional area, Garwin [Gar52] states that only a fraction of the light can be transmitted, which is equivalent to the ratio of the cross–sectional areas $\frac{A_{\text{out}}}{A_{\text{in}}}$.

The reflective surface of the light guide can be specular or diffuse. In the specular case, the incident light is reflected at the same inclination angle, i.e., $\theta_{\text{i}} = \theta_{\text{r}}$, which is the case for a mirror. For a diffuse surface, the reflection will not depend on the incident angle, and it will follow Lambert's cosine law [Leo94] that will not be considered in this work.

Air–core light guides may present a degradation in the light transmission with radiation damage. For example, from radiation tests performed for two different types of aluminized Mylar, Type–1 AM and Type–2 AM [ABA+06], these materials showed a decrease in their light transmission capability of about 14% and 3%, respectively [ABA+06], following irradiation for 72 hours with 10 Mrad of γ-rays from a ^{137}Cs source.

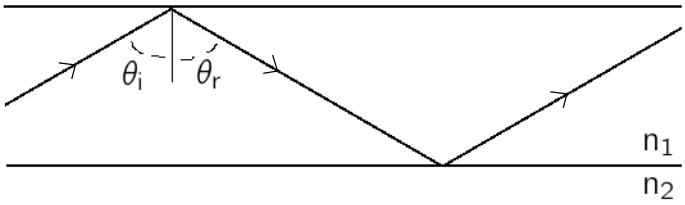

FIG. 3.7 Specular reflection for a light ray passing through a light guide with $n_1 > n_2$. For $\theta_i > \theta_c$, the light will undergo total internal reflection as it travels along the pipe.

- **Acrylic light guide**

  The acrylic light guide for the prototype detector is shown in Figure 3.8. This is a trapezoidal light guide with a rectangular cross-section. Its length is 12 cm and the cross–sectional areas are 29×29 mm^2 and 18×18 mm^2, respectively. The larger side is in contact with the scintillator and it is coupled using optical grease, which has an index of refraction similar to both of them. The smaller side is coupled to

the PMT also using optical grease, whose refraction index is similar to that of the photocathode window (Table 3.2).

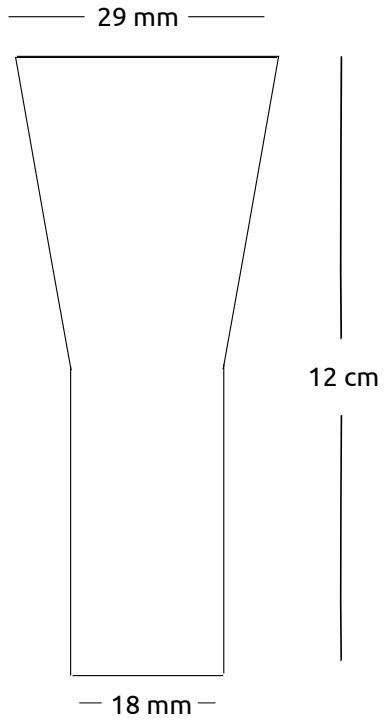

FIG. 3.8 Acrylic light guide for prototype detector.

Acrylic	GS20	Glass	Optical grease
1.5	1.55	1.5	1.5

TABLE 3.2 Approximate values of indices of refraction of relevant materials.

- **Air-core light guides**

  The air-core light guides were designed with a rectangular cross–section of area 18×18 mm^2, as shown in Figure 3.9. Using this size it is possible to couple the light guide and the photomultiplier directly.

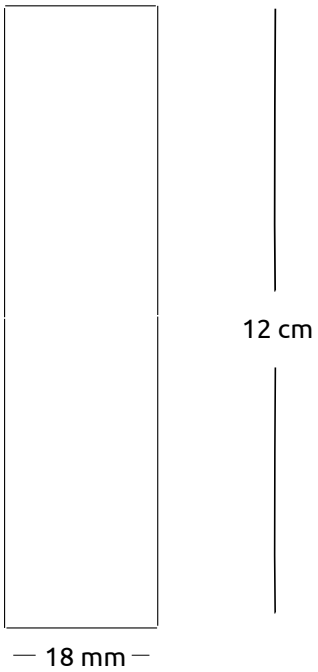

FIG. 3.9 Air-core light guide for prototype detector.

3.3.4 PHOTOMULTIPLIER

- **General description**

  Photomultipliers (PMT's) are used to convert incident light into an electric current that can be measured. A schematic design of a photomultiplier is shown in Figure 3.10, where it is possible to identify four main parts: the photo–cathode, a focusing region for electron collection, an electron multiplier section (also known as a series of dynodes) and the anode, where the signal is finally collected.

  The way a PMT works can be described in few steps as follows; a high–voltage is applied across the photocathode–anode system. When a photon strikes the photocathode, which is made of a photosensitive material, an electron may be ejected due to the photoelectric effect. The electron is accelerated and collides with the first dynode, liberating secondary electrons as a consequence of the energy released. Then, secondary electrons are accelerated to the following dynode, striking it and releasing energy which is used to liberate more electrons at each stage. At the end, the cascade of all electrons is collected at the anode. The magnitude of the signal

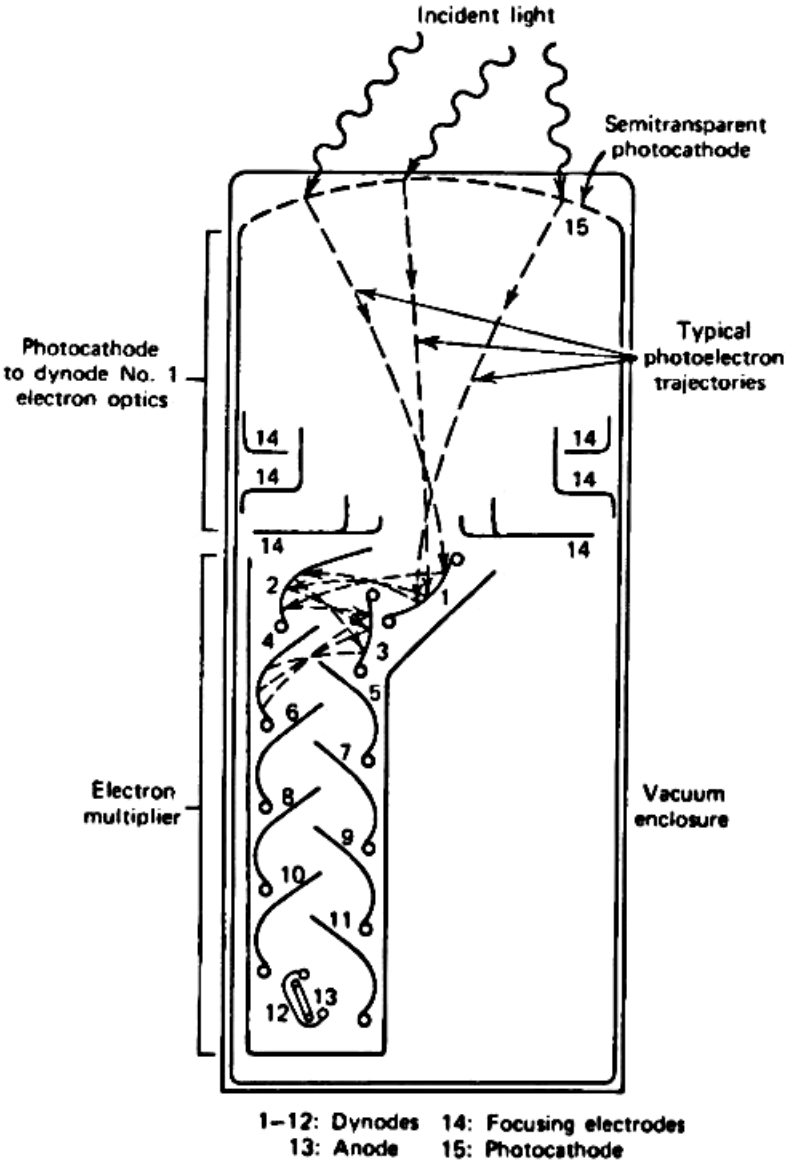

FIG. 3.10 A schematic representation of the elements inside a PMT tube [Kno00].

obtained from the anode will be proportional to the incident light intensity; the gain is a function of the applied voltage and the biasing of the dynode chain. For N dynodes the gain varies approximately as $G \sim (\mathrm{HV})^N$.

- **The photoelectric effect**

  The efficiency of conversion due to the photoelectric effect depends on the material and the frequency of the incident light. Therefore, the spectral response of the cathode is expressed in terms of the quantum efficiency (QE), which is a function of the wavelength of the incident photon. This quantity is equivalent to the ratio between the number of photoelectrons released $n_{released}$ and the number of incident photons $n_{incident}$ [Leo94]:

  $$QE(\lambda) = \frac{n_{released}}{n_{incident}}. \tag{3.4}$$

  In general, the value of the quantum efficiency has a maximum between 20-30%.

- **Photomultiplier construction**

  1. **Photocathode materials: Bialkali**

     In general photocathodes are made of alkali materials which are composed of potassium, antimony and cesium (K-Sb-Cs). Bialkali photocathodes are widely used due to their high sensitivity in the blue region which makes them particularly useful for scintillation counting [NHIM10].

  2. **Window materials: Borosilicate glass**

     Borosilicate glasses are generally used as window materials in the photomultiplier due to their low cost and adequacy for wavelengths higher than $\sim$ 300 nm. In addition, this material works well in combination with bilakali materials [Ham15].

- **The gain**

  In a PMT, the gain G is defined as the the ratio between the current from the anode (I_a) and the current from the photocathode (I_c):

  $$G = \frac{I_a}{I_c}$$

  The gain depends on the number of dynodes (n), the fraction of all photoelectrons collected along the multiplier structure (α), and the coefficient of secondary emission

(ρ), which will depend on the energy of the primary electron. The gain can be written as [Kno00]:

$$G = \alpha \times \rho^n.$$

For example, for α close to one, a factor of secondary emission of 5 and 11 gain stages/dynodes, the gain is about 5×10^7.

- **Hammamatsu R7600U**

Property	Value
Supply voltage (V)	800
Photocathode material	Bialkali
Window material	Borosilicate glass
Range (nm)	$300-650$
Peak wavelength (nm)	420
Gain	1.8×10^6
Time rise (ns)	1.2
Operating ambient temperature (°C)	-30 – $+50$
Dynode structure	Metal channel
Dynode stages	10

TABLE 3.3 The main properties of the photomultiplier Hamamatsu R7600U [Ham14].

The photomultiplier used for the prototype detector is a Hamamatsu R7600U-00-M4 [Ham14], a 2×2 multianode PMT tube widely used for scintillation counting. The photocathode material is Bialkali and its window is made of Borosilicate glass. This PMT operates at -800V which is applied to the cathode, with the anode at ground. The spectral response is within the range between 300 and 650 nm, with a peak at 420 nm. The main properties of this PMT are summarized in Table 3.3.

The dimensions of the PMT are shown in the schematic diagram in Figure 3.11. The photocathode has an area of 18×18 mm^2 which is the same as the cross–sectional area of the light guides for the prototype detector. PMT's are sensitive to magnetic fields, which affect the trajectories of the electrons inside the photomultiplier. Figure 3.12 shows how the output from the anode is affected as a function of the magnetic filed, for the R7600U PMT. From the graph, it is observed that the z-axis is the most sensitive; the

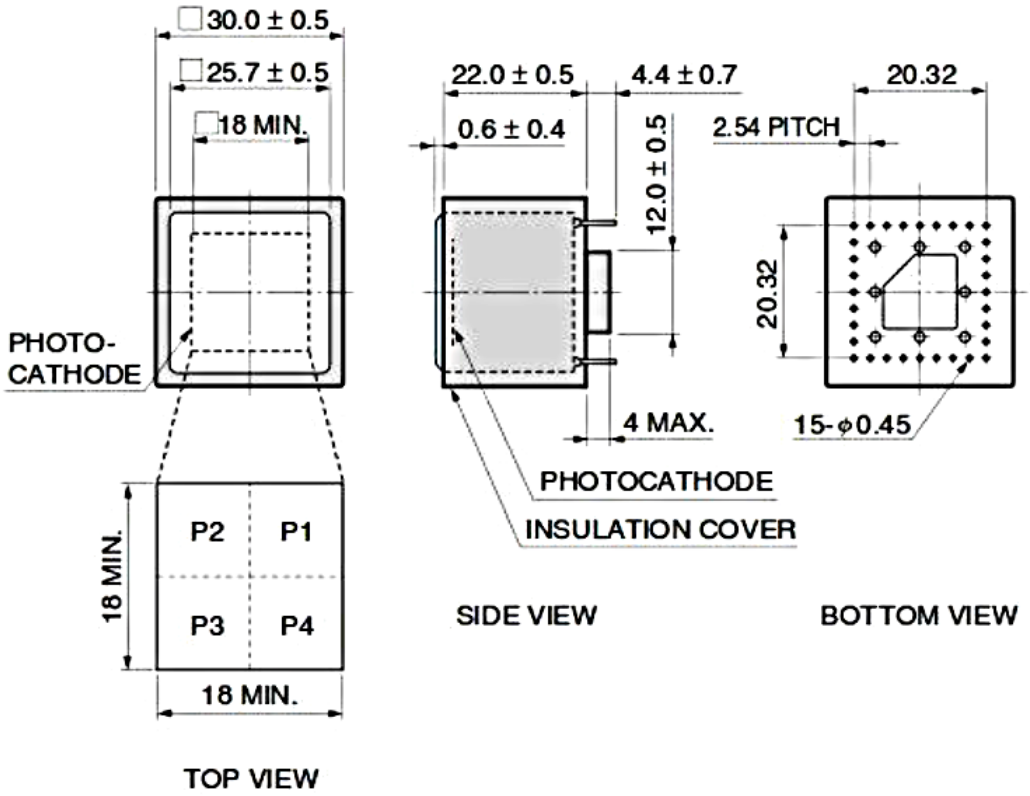

FIG. 3.11 Dimensions of Hamamatsu R7600U.

PMT's sensitivity is reduced 40% by a magnetic flux density around 10 mT aligned in this direction.

The quantum efficiency of the photocathode as a function of the wavelength is shown in Figure 3.13. In the graph, the curve labeled as type-00 corresponds to the PMT used for the prototype detector. The QE is approximately 24% averaged over the wavelength of interest for this device.

3.4 UCN DETECTOR

The nEDM measurement is based on the polarization of UCN after the Ramsey spin sequence described in section 1.1.4. Polarization of UCN will be determined by comparing transmission through a magnetized foil for the two neutron spin directions. In order to

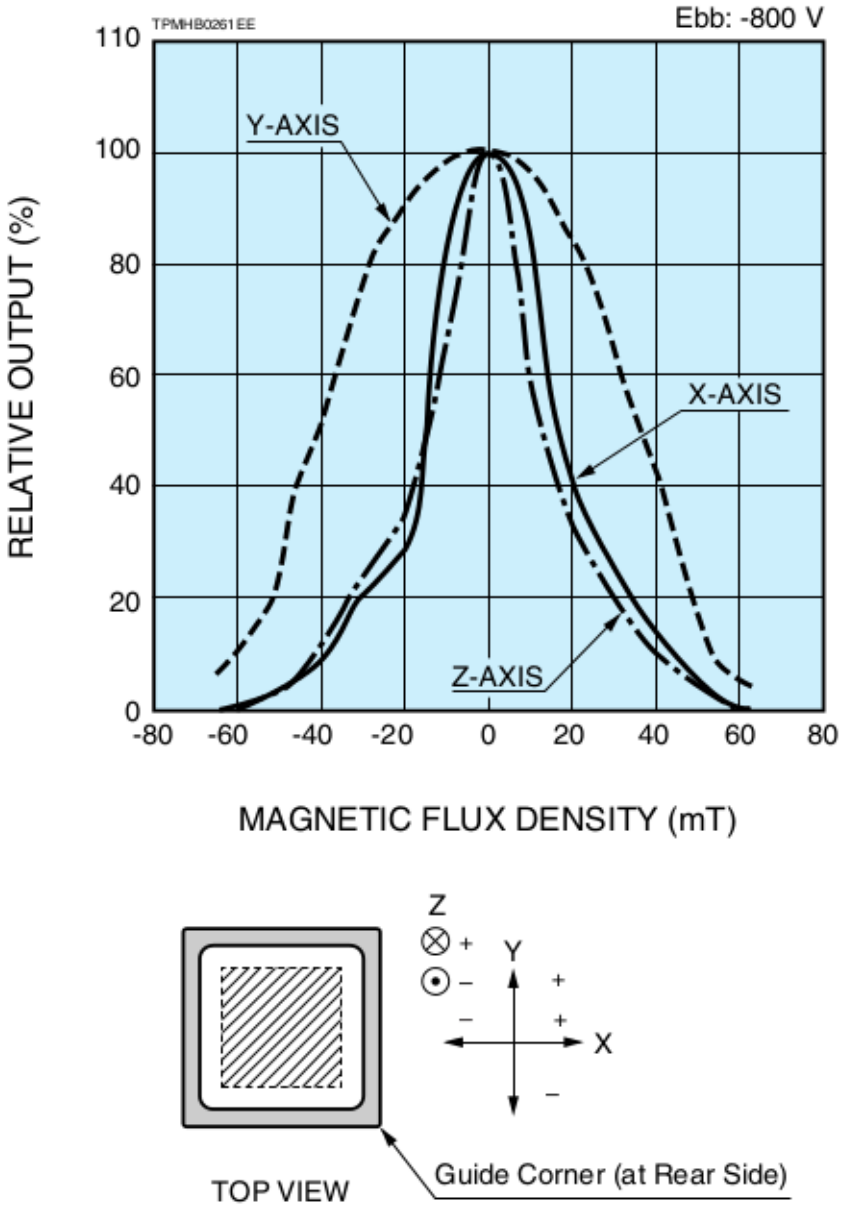

FIG. 3.12 Dimensions of Hamamatsu R7600U.

count the number of neutrons of each spin state, two phases will be considered for the detector [C15]. In the first phase, spin states will be sequentially selected; the entire detector will consist of a single spin flipper, a spin analyzer and a neutron counter coupled to a PMT (see Figure 3.14). In the second phase, a simultaneous spin measurement system

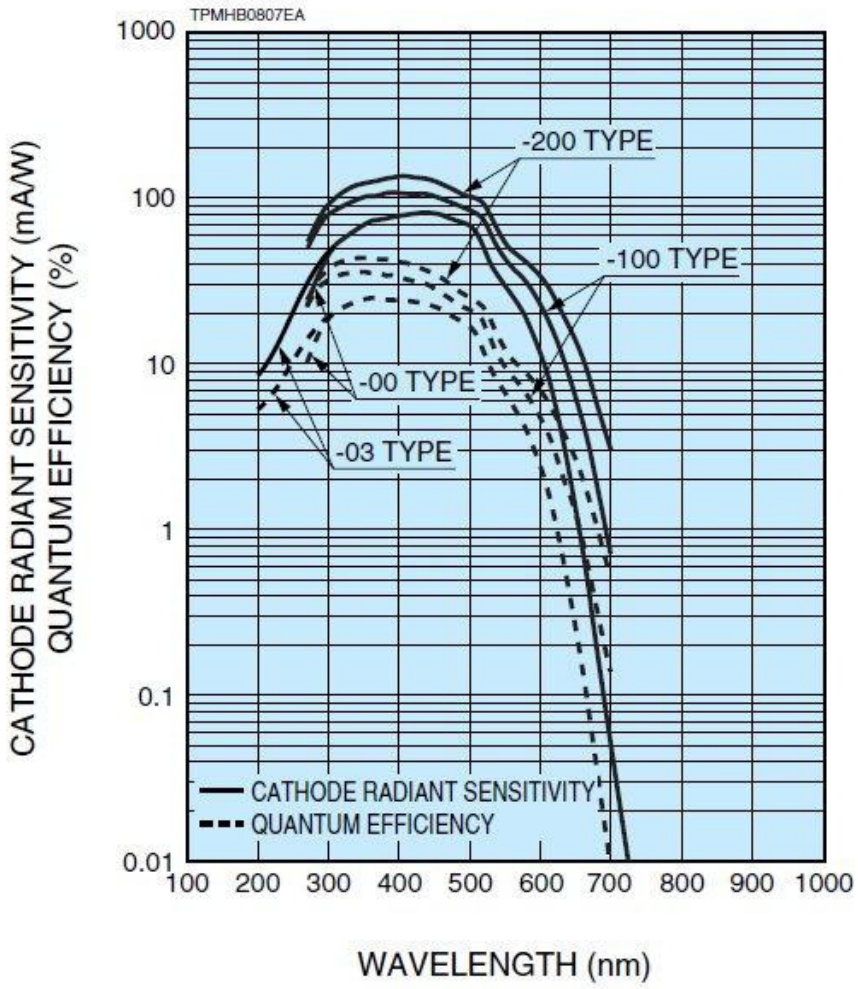

FIG. 3.13 Quantum efficiency of the photocathode for Hamamatsu phothomultipliers type R7600U-M4.

will be implemented[4], which will allow to count simultaneously both UCN spin states from both EDM cells and then to measure the UCN polarization with high efficiency. UCN from the two EDM cells will be guided to the UCN detector where neutrons with different spin orientations will be driven to different detector elements; the entire assembly set up for the UCN detector will consist of two sets of UCN spin flipper coils, four spin analyzing foils, and two UCN counters coupled to photomultipliers, as shown in Figure 3.15.

The analyzer foil will consist of a thin magnetized iron foil ($\sim$ 2 T) deposited on a

[4]This model is based on the one developped in the Université de Caen [HÍ14].

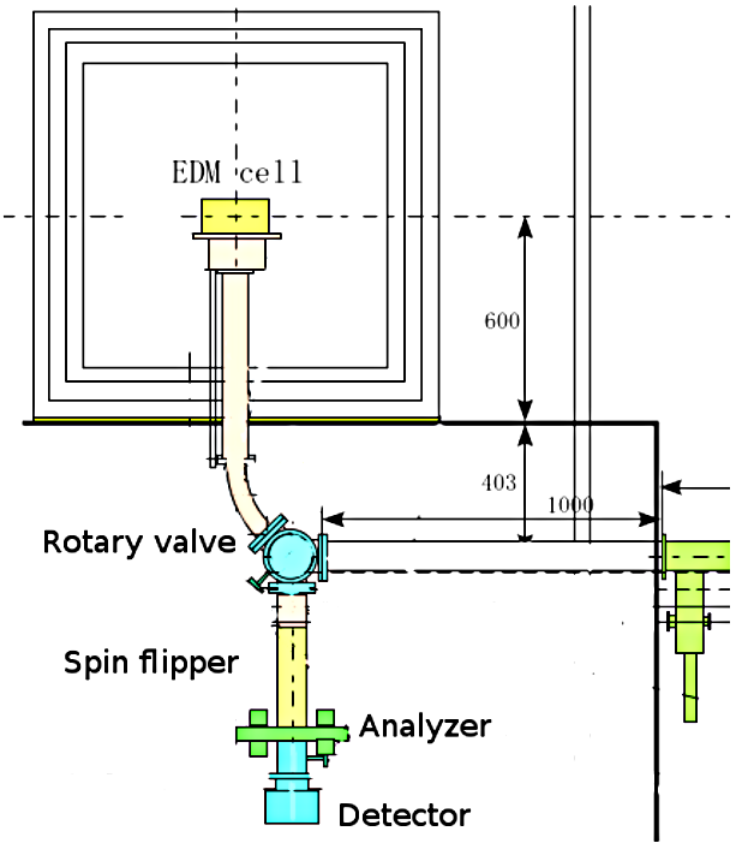

FIG. 3.14 A schematic diagram of the entire UCN detector in Phase 1. The UCN rotary valve is opened and ultra-cold neutrons will be dropped into the spin flipper, analyzer and UCN detector [C15].

thicker aluminium supporting substrate ($\sim$ 50 μm). A magnetic potential of 60 $\frac{\text{neV}}{\text{T}}$ will be used by the spin analyzer to filter the spin direction of UCN [C15]. UCN with their spins antiparallel to the analyzer magnetic field will pass through and be detected, the others will be reflected away from the detector.

Magnetic profiles from these analyzer foils were measured and simulated by the UCN detector group [Pie13] [Com14] (see Appendix C). From these results and considering the design of the experiment (see Figure 3.14), it is concluded that PMTs must be placed outside the magnetic field of spin analyzing foils by implementing light guides with a length of 12 cm, where the magnetic field at that distance will be less than 1 mT.

The prototype neutron EDM experiment at RCNP was implemented using a ^{3}He

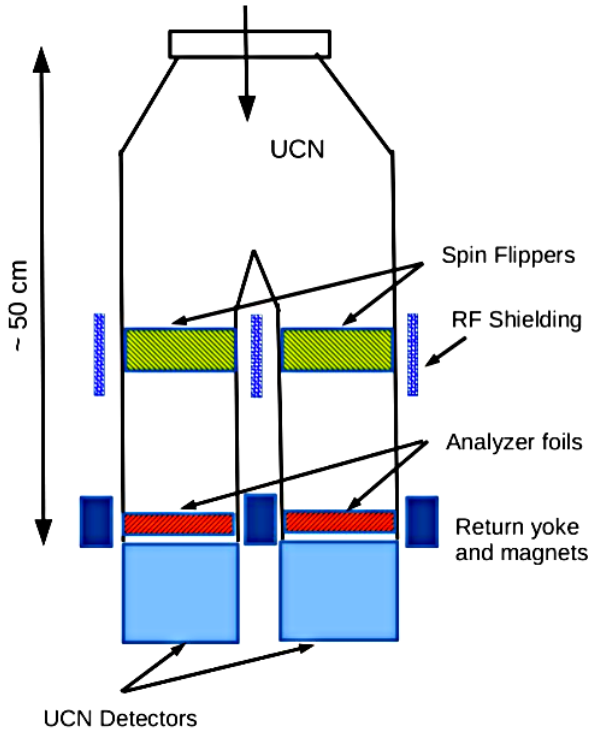

FIG. 3.15 A schematic diagram of the entire UCN detector in Phase II of the nEDM experiment at TRIUMF [Com14].

multi–wire proportional counter [C15] as a neutron detector. This will be used in the first phase of the nEDM experiment at TRIUMF. During the second phase, a design similar to that used in UCN experiments at PSI [Hí4] an described above, will be used. This includes ^{6}Li doped glass scintillators, which offer advantages such as a faster recovery time compared to gas counters.

The estimated number of UCN in the EDM cell when the TRIUMF source is fully operational is 6.6x10^{6} (using Geant4) [C15]. These will be transmitted through the UCN guide pipe (85 mm) to the entrance of the UCN detector (20 mm radius opening). Geant4 simulations show that the rate of UCN at the detector will be about 1.3 MHz (see Appendix D) [HJ12b].

For the final configuration, the detector will be segmented in order to reduce pile up, which occurs when more than one pulse arrives within the resolution time of the detector, leading to an incorrect measure of the pulse height [Dat77]. Considering a simple model

for pile–up with a pulse width of 250 ns, it was found that pile up was less than 10% for a counting rate less that 200 kHz [Com13], where this latter corresponds to the maximum rate calculated for an individual tile (29×29 mm^2 central detector). As a result, the segmented detector will consist of 29 mm square edge scintillator tiles arranged in a 3×3 array as shown in Figure 3.16. The entrance pipe of the detector will have a cylindrical shape with an inner diameter of 85 mm.

Scintillators will be optically bonded to light guides, and both parts will be placed inside the vacuum chamber, while PMTs will be outside the vacuum and at room temperature. For acrylic light guides, models implemented for testing at the Unversity of Winnipeg have a rectangular area of area 29×29 mm^2 connected to the PMT with a circular area of 18 mm diameter.

The efficiency of the existing ^{3}He detector at RCNP is around 80%. This sets a goal for the detector in the second phase of the experiment, which will use ^{6}Li doped glass scintillators. It is planned to maximize efficiency by limiting the width of dead zones the area of the detector in Figure 3.15 will have a 200 μm separation between tiles, which will reduce the efficiency by 1%, according to the study [Com13] and by setting a minumum thickness for the scintillation glass. The thickness of the glass pieces will be 60 μm and 100 μm for the GS30 and GS20 layers, respectively. These small thicknesses will reduce the thermal neutron capture and gamma ray sensitivities which are the two main backgrounds that will be present during the experiment. The glass layers will be molecularly bonded.

One type of background expected in the experiment is gamma–rays coming from experiments in the vicinity of the future nEDM experiment at TRIUMF. Measurements of gamma background in this area, were obtained from the the PiENU experiment at TRIUMF [HJ13]. These results were implemented in the Geant4 simulation for the UCN detector [Com13]; some of the distributions obtained are shown in Appendix E. From these results, it was found that 90% of the detected gamma–rays had energies below 3 MeV. Since this energy is comparable to one of the reaction products generated from a neutron capture, the energy deposited by both reaction products (alpha and triton) must be detected at the same time in order to prevent event losses [Com13].

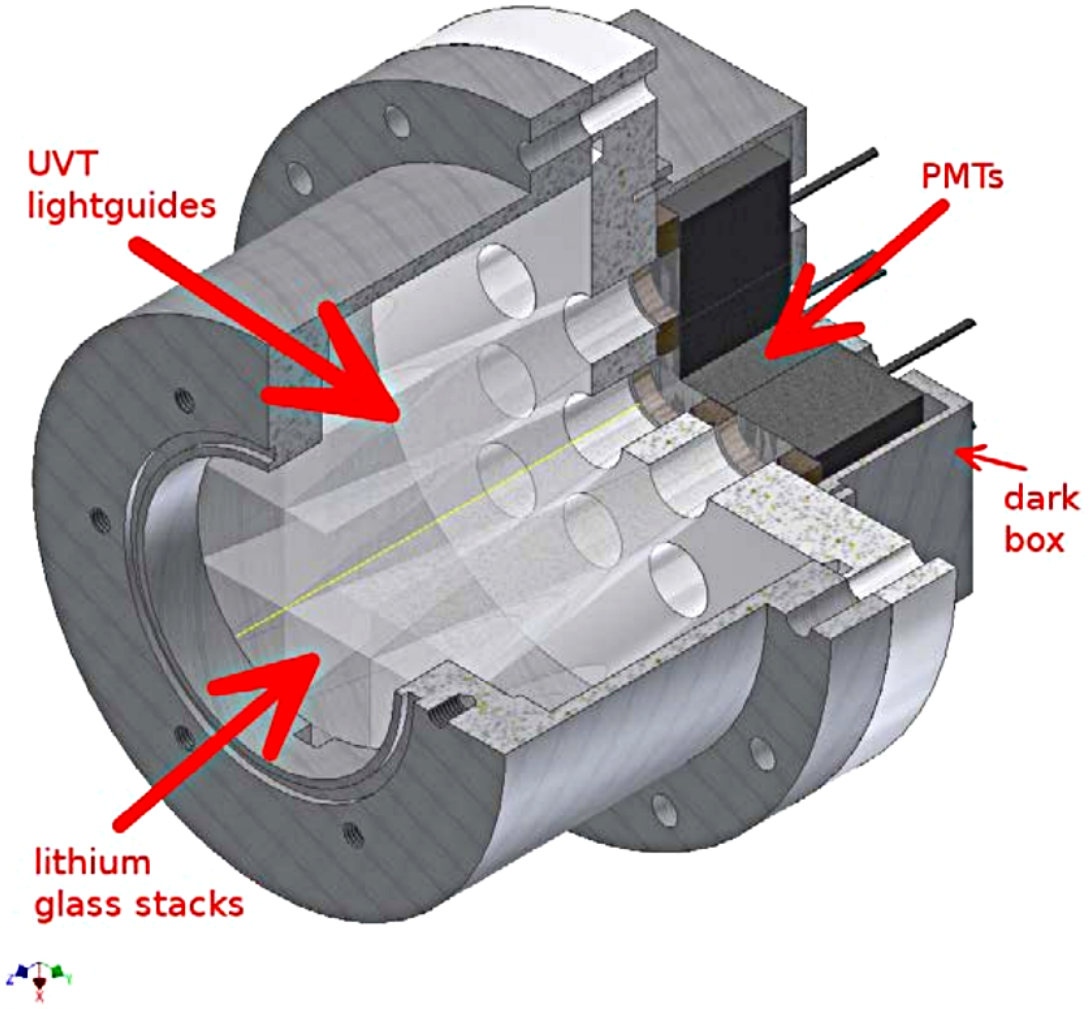

FIG. 3.16 3–Dimensional drawing for the final configuration of the segmented UCN detector [Com14].

4

SIMULATION AND TESTS OF THE PROTOTYPE DETECTOR

For the simulation study of the prototype detector two different types of light guides were considered, acryclic and air–core light guides. The light collection at the PMT is better for acrylic light guides since its index of refraction is very similar to the scintillator material, and therefore, a higher probability for scintillation photons to be transmitted to the light guide. However, if charged particle backgrounds are present in the experiment, these may generate Cerenkov light when passing through the acrylic, producing a background signal in competition with that from neutron capture events. In that situation, air–core light guides could be a better choice for the UCN detectors. In this work, a characterization of both types of lightguides was made, as will be discussed below.

4.1 Introduction to Geant4

This brief introduction to Geant4 is based on the article from S. Agostinelli et al. [Aea03]. Geant4 is an object-oriented simulation developed with the aim to accurately model processes involving the interaction of particles and matter in a range of energy from $\sim$ 250 eV to $\sim$ TeV.

Geant4 is ideal for the development of high precision simulations for particle detectors. This "object-oriented simulation toolkit" consists of a set of software components which can be used to construct and simulate a broad range of real experiments. A Geant4 simulation includes the following features:

- The geometry of the system.
- Materials involved.
- Particles of fundamental interest.
- Generation of primary particles.
- Tracking of particles.
- Physics process governing particle interactions.
- The response of sensitive detector components.
- The generation of event data.
- The storage of events and tracks.
- The visualisation of detector and particle trajectories.

This structure for Geant4 was developed considering the content requirements for the basic body of a software system: an event generator, detector simulation, reconstruction and analysis; all these are included in the list above. Geant4 includes a set of class categories[1] linked to each of the mentioned items, which together facilitate an accurate simulation of the passage of particles through matter.

4.2 Previous work

The prototype detector simulation described here is based on previous work described in [Com14]. In this simulation, the detector consists of a stack glass (GS20 - GS30) coupled to a photomultiplier. In Figure 4.1, the scintillator stack is represented by a rectangular box of dimensions $2.0 \times 2.0 \times 0.1$ cm^3. In the simulation, a neutron is captured by a ^{6}Li glass dopant, emitting an alpha and triton particle in opposite directions, and their energy is fully deposited in the glass. This energy is re-emitted by the material

[1] These correspond to each of the logical units that make up the Geant4 logical system, which can be modified independently without interfering with each other.

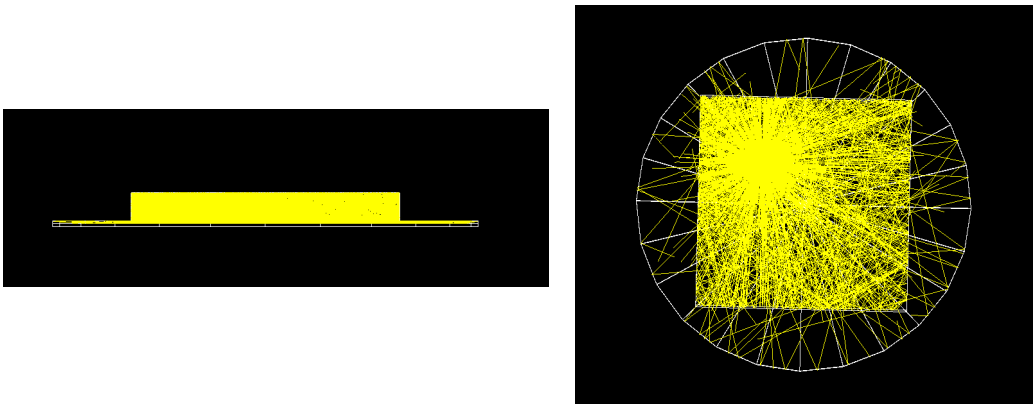

FIG. 4.1 Simulation visualization for the detector developed in the previous work [Com14].

as visible photons represented in the same figure by yellow rays. The released light is detected by the photomultiplier, corresponding to a circular tube in the simulation.

4.3 IMPROVED SIMULATION FOR THE PROTOTYPE DETECTOR (THIS THESIS WORK)

The simulation previously described was modified by introducing light guides and their optical parameters, in order to compare simulations and experimental results, obtained from benchmark tests with various prototypes. In the following, I present the various Geant4 data classes that were modified, including a description of the changes implemented in each case.

1. **Materials**

   For declaring materials in Geant4 it is necessary to define their composition in terms of elements and atomic isotopes. Most of the elements used in this thesis are contained in the Geant4 database, but in the case of specific materials, these must be defined in the simulation.

   The Geant4 user's class in which materials are declared is named LiGDectectorConstruction. In the previous simulation, most of the materials that will be used in this work were declared, including the glass types GS20, GS10, GS30. The materials

that were added to this class, in the work performed for this thesis are: acrylic, aluminized mylar and Miro.

The acrylic was used to simulate a light guide with trapezoidal cross sectional area, as shown in Figure 3.8. To minimize losses of light rays that were not confined to the acrylic by total internal reflection, aluminized Mylar was used as a wrapping material for this light guide. Acrylic and Mylar are composed of Carbon (C), Hydrogen (H) and Oxygen (O), but each material has a different mass fraction of these elements. The densities considered for Acrylic and Mylar are 1.19 g/cm^3 and 1.397 g/cm^3, respectively.

Air–core light guides, shown in Figure 3.9, were simulated using Miro–2 and Miro Silver confining materials which are specular aluminum sheets with a high reflectivity[2] and thickness $\sim$ 0.08 mm, developed by the company Alanod [Ala14]. The composition of these materials is very close to those for an aluminium sheet, which is predefined in Geant4. Therefore, the Geant4 aluminum composition was used to define the Miro material, and the specific values of the reflectivity for Miro–2 and Miro Silver, were used to characterize each of the Alanod materials.

2. **Geometry and volumes for the prototype detector**

The entire detector was constructed inside a big box denoted *experimental hall*, of volume $\sim$ 27 m^3 and filled with vacuum. The class in which all the volumes are constructed is denoted LiGMainConstruction; basic forms such as trapezoids and rectangles were used to build the different elements of the detector, which in turn are associated with specific materials. The simulated volumes for the acrylic and air–core lightguides are shown in Figures 4.2 and 4.3, respectively.

The scintillator was placed at the origin of the coordinate system and from there, locations and geometries of all the other elements were defined. The lightguide connected the ^{6}Li glass to the photomultiplier, where physical information about

[2]The reflectivities for Miro–2 and Miro Silver are around 95% and 98%, respectively according to [Ala14].

light collection was recorded. For this purpose, the PMT had to be defined as a *sensitive detector*, as will be discussed in the following section.

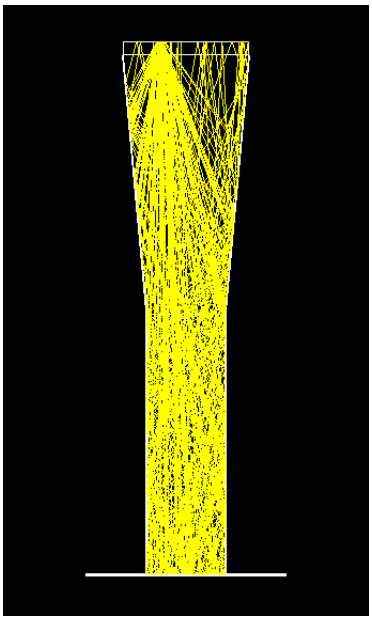

FIG. 4.2 Simulation visualization of the prototype detector with an acrylic light guide.

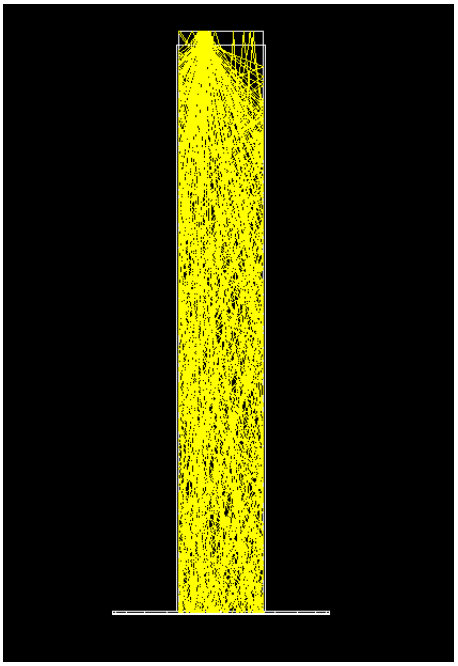

FIG. 4.3 Simulation visualization of the prototype detector with air-core light guides.

3. **Generation of primary particles**

From neutron capture on ^{6}Li in the scintillator, alpha and triton particles are released in opposite directions (180°). This physical process taking place in the glass stack is defined in the Geant4 class LiGPrimaryGeneration. The light generated from the scintillation process is collected by the PMT and data on the energies and ranges of the incident particles, can be collected in an output file.

The kinetic energies released in a neutron capture on ^{6}Li by the alpha and triton are 2.05 MeV and 2.75 MeV, respectively, according to reaction (3.2). These energy values were introduced in this Geant4 class. Alpha and triton particles have very short ranges around 6 μm and 37 μm respectively, in the lithium–6 glasses. These values can be obtained from the information collected in the LiGTrackingAction class; the simulated range distributions of both particles are shown in Figure 4.4.

4. **Optical properties**

Optical properties must be implemented for the prototype detector for the scintillator glass, the air-core lightguides and the wrapping material of the acrylic lightguide. The scintillator properties were specified as part of a previous work (see section 4.2). In my work for this thesis, optical properties were implemented for the lightguides, and adjusted for the photomultiplier of the prototype detector.

The scintillator in Geant4 is represented in terms of its photon emission spectrum and the exponential decay time spectrum, this latter described by a fast and slow time constant (see subsection 3.3.2). Therefore, in the simulation were specified the Geant4 variable SCINTILLATIONYIELD and the two time constants FASTTIMECONSTANT and SLOWTIMECONSTANT (50 ns and 70 ns, respectively). In our case, GS20 and GS30 glass types exhibit an emission spectrum that varies between 330 and 500 nm [Spo77]. Other properties of the material such as the index of refraction (RINDEX) and absorption length (ABSLENGTH) were also defined. An extract of the code implemented in the simulation for the scintillator is shown in Appendix F.

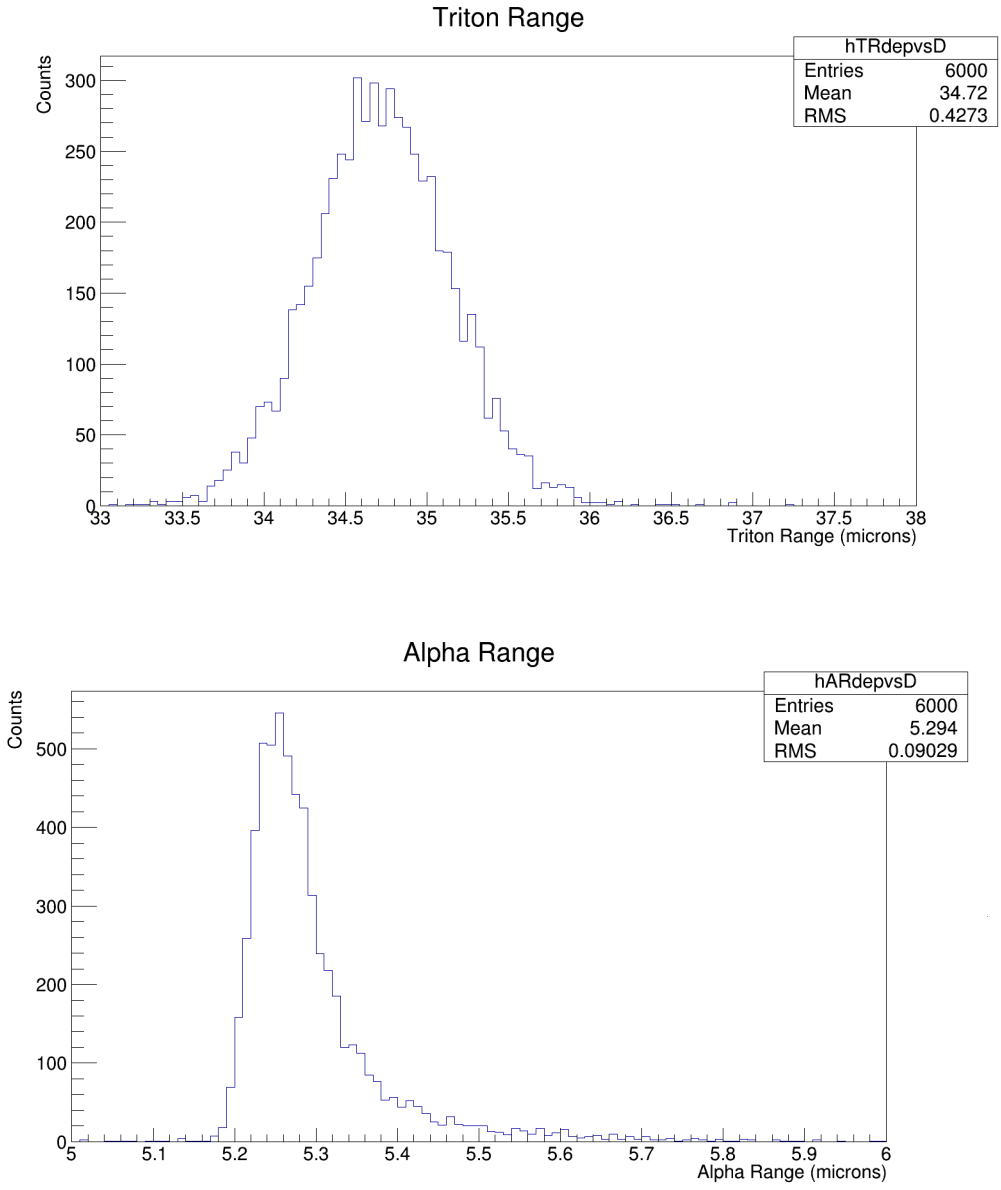

FIG. 4.4 Range distributions of alpha and triton particles in 6-lithium glass.

As a result of the scintillation process in Geant4, optical photons are generated and these latter undergo refraction, reflection or absorption at medium boundaries depending on the specifications given by the user of the code. Properties of the surface and reflectivity of the materials must be specified according to those used in the experiment in order to obtain accurate results from simulation.

Boundary processes in Geant4 are responsible for providing physical information

about surfaces. For a photon passing from one medium to another, the behaviour is affected by several surface parameters: the interface type, the physics model to be used and the surface finish. The models for surfaces available are glisur, where only efficiency and reflectivity need to be specified; and unified, which also requires that reflection probability constants be defined [Gea15a].

For an interface between two dielectric media, the type is set as dielectric–dielectric and the model chosen is unified. Photons in this case may undergo refraction, reflection or total internal reflection, and the latter will depend on the values of the angle of incidence and refraction index, which are determined by the energy of the incident photon[3].

In the case of an incident photon from a dielectric to a metal (dielectric–metal), it may be either reflected back or absorbed by the metal; the model applied in this case is glisur. Along with these specifications, values for the reflectivity of the material as a function of photon energy must be set in the code.

For aluminized mylar, the optical interface selected was dielectric–metal and therefore the model chosen was glisur and a polished surface. This material exhibits a high reflectivity, around 90%.

For Miro air–core light guides, photons travel from the scintillator to the PMT through total external reflection, and the same optical properties selected for aluminized mylar can be applied in this case: a *dielectric–metal* interface type, *glisur* model and a *polished* surface. Values for reflectivity depending on the energy were introduced in the simulation depending on the material. For Miro Silver a reflectivity around 98% [Ala14] was considered. In the case of Miro–2, its reflectivity was defined around 93% based on the spectrum for Miro materials in Figure G.1 and the results obtained by R. López in [Lóp10]. As an example of the optical properties implemented in the simulation, an extract of the code for the Miro Silver light guide is shown in Appendix G.

[3] Note: In the case when a perfectly smooth surface is simulated and no additional parameters are introduced, the probabilities of reflection and refraction are calculated according to the Snell's law. Indices of refraction of both materials need to be defined [Gea15c].

4.3.1 PMT for the prototype detector

In the simulation, the PMT entrance is modeled as a glass with an aluminum plate at the back (0.32 mm thick). This corresponds to a rough aproximation of a real photocathode, and this model was based on one of the extended optical examples of Geant4 [Gea15b]. In order to model the experimental prototype, specifications from the real photomultiplier (see subsection 3.3.4) were considered. In particular, the values of quantum efficiency as a function of the wavelength from Figure 3.13 were introduced in the simulation code as shown in Appendix H.

4.3.2 Simulation of the test experiment

As the next section will describe, an experimental test was performed in the laboratory at the University of Manitoba using a prototype detector and an ^{241}Am radiative source. In order to compare and test the simulation made for a neutron capture discussed throughout this section, a simulation of the experiment using an alpha source was developed.

The main modifications to the simulation required for alpha detection were made in classes LiGMainVolume and LiGPrimaryGeneration. Alpha particles were generated at the top and outside the volume of the scintillator glass, and each particle was directed downward with a randomized angle (see Figure 4.5). Subsequently, alpha particles entered the scintillator stack. These modifications can be described according to the type of light guide used in each case as follows:

- For the prototype set up with an acrylic light guide as shown in Figure 4.2, the alpha source was placed touching the GS30 glass of the scintillator stack. It was assumed that the energy reaching the glass was 5.5 MeV, the typical value for an ^{241}Am source.

- For the air-core light guide configuration (see Figure 4.3), in the experimental set up there is an air gap ($\sim$ 5 mm) between the scintillator stack and the 241-americium source. Once the alpha particles have reached the scintillator, their energy is reduced

to an approximate value of 5.01 MeV [Y+03], the energy value implemented in the simulation.

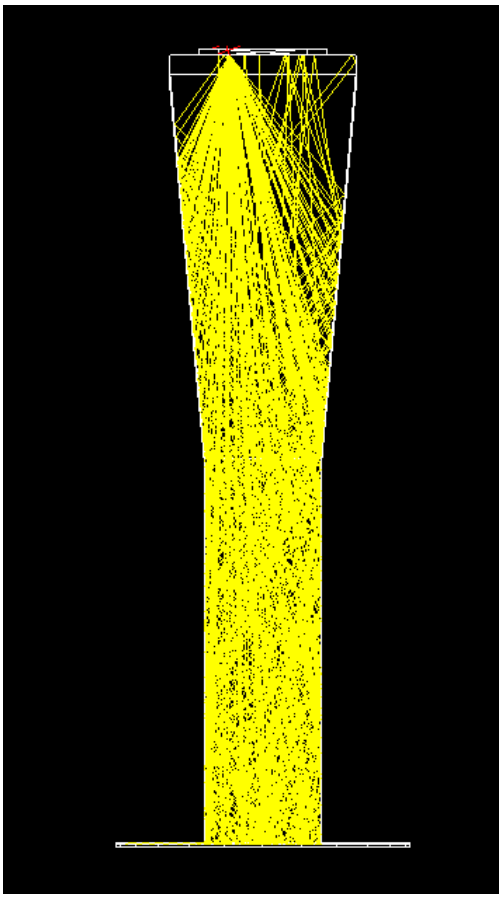

FIG. 4.5 Simulation visualization of the prototype detector with an acrylic light guide and an alpha source (the red rays at the top of the figure).

4.3.3 Simulation results

In order to study the number of scintillation photons collected from the 6-Lithium glass in our prototype experiment, simulations in Geant4 were developed, as described in this section. The number of photons hitting the photomultiplier (N_{ph}) were saved in a ROOT [Roo16] file; these results were used to generate histograms for each light guide attached to the prototype detector. From these distributions, the number of photoelectrons (N_{pe}) was obtained via the following expression [Nae07]:

$$N_{pe} = QE \times N_{ph} \quad , \tag{4.1}$$

where QE denotes the quantum efficiency which is around 24% for wavelengths between 300 nm and 478 nm, as shown in Figure 3.13.

- **Neutron capture (alpha and triton particles) simulations**

Light guide	Mean (Npe)	Standard deviation
Acrylic	(37.25 ± 0.03)	(2.96 ± 0.02)
Air–core Miro–2	(37.31 ± 0.03)	(2.91 ± 0.02)
Air–core Miro Silver	(22.63 ± 0.02)	(2.31 ± 0.02)

Table 4.1 Table with values of mean (μ) and standard deviation (σ) from Gaussian fits to the neutron capture simulations. These results were obtained from simulations of neutron capture in glass stack.

The simulation was run for 9060 neutron captures in the glass stack; the corresponding outputs for the acrylic and air-core lightguides are shown in Figures 4.6(a), 4.6(b) and 4.6(c). These distributions were fitted in ROOT using a Gaussian function for this purpose[4]. Values of the mean and standard deviation were extracted from simulated results, and these are shown in Table 4.1. Statistical errors on the mean and standard deviation are calculated as the fitted standard deviations divided by the square root of the total number of events (9060).

[4]Gaussian functions were used, since we have a large number of events which are symmetrically distributed around a mean value.

When comparing simulation results for the air–core Miro Silver and Miro–2 light-guides, the number of photoelectrons detected for the latter case was significantly greater. This illustrates the dependence of the number of photons reaching the PMT on the reflectivity as a function of the wavelength. The Miro Silver material has a higher reflectivity ($\sim 98\%$) than Miro-2 ($\sim 95\%$); however, for the wavelengths with the higher values in the 6–Lithium glass emission spectrum [Spo77], the reflectivities in Miro–2 are probably higher compared to those in Miro Silver (see Figure G.1).

From Table 4.1, it is seen that prototypes with Miro–2 and Acrylic light guides lead to a greater number of photoelectrons (about 14 p.e. more) compared to the Miro Silver light guide. The mean value for the number of photoelectrons collected using the Miro–2 light guide is very similar to that of the acrylic light guide.

- **Alpha source test simulations**

Light guide	Mean (Npe)	Standard deviation
Acrylic	(41.22 $\pm$ 0.04)	(3.12 $\pm$ 0.03)
Air–core Miro–2	(38.24 $\pm$ 0.04)	(3.10 $\pm$ 0.03)
Air–core Miro Silver	(23.27 $\pm$ 0.03)	(2.37 $\pm$ 0.02)

TABLE 4.2 Table with values of mean (μ) and standard deviation (σ) from Gaussian fits. These results were obtained from the simulation of the ^{241}Am source test experiment.

For the simulation of the test experiment using the ^{241}Am source, spectra for the number of photoelectrons for acrylic and air–core lightguides were also obtained. These results were plotted and fitted to Gaussian functions in ROOT, as shown in Figures 4.7(a), 4.7(b) and 4.7(c). Similar conclusions to those for neutron capture simulation results may be reached, by comparing the values of the centroids in Table 4.2 for the different types of light guides. The main difference, however, lies in the number of photoelectrons detected with the acrylic light guide which is higher compared to the Miro–2 (by around 10%).

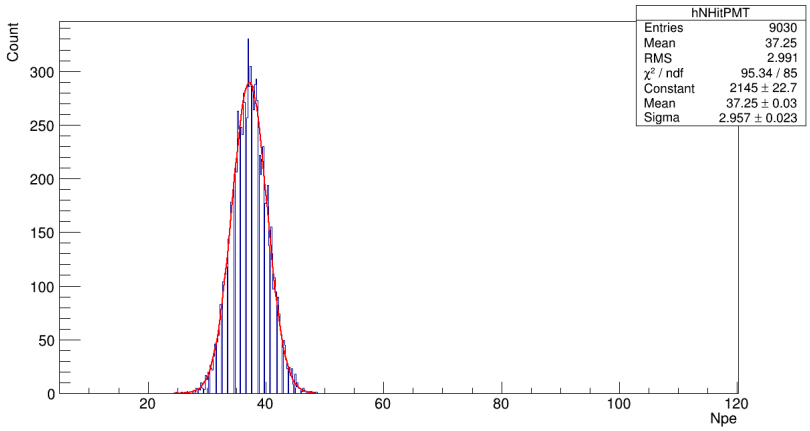

(a) Npe distribution for Acrylic light guide.

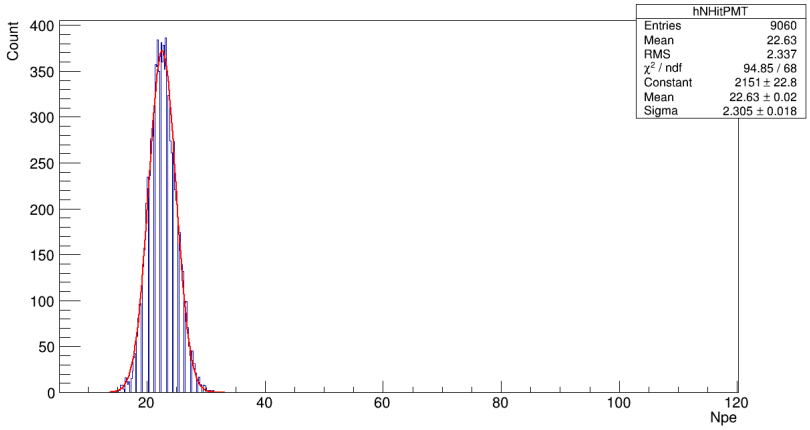

(b) Npe distribution for Miro Silver light guide.

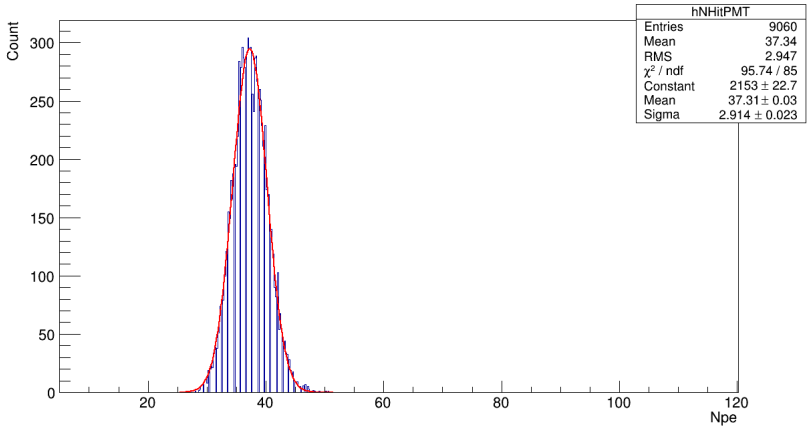

(c) Npe distribution for Miro-2 light guide.

FIG. 4.6 Number of photoelectrons distribution for Acrylic, Miro Silver and Miro-2 light guides obtained from neutron capture simulations. Vertical scales are not the same for all distributions.

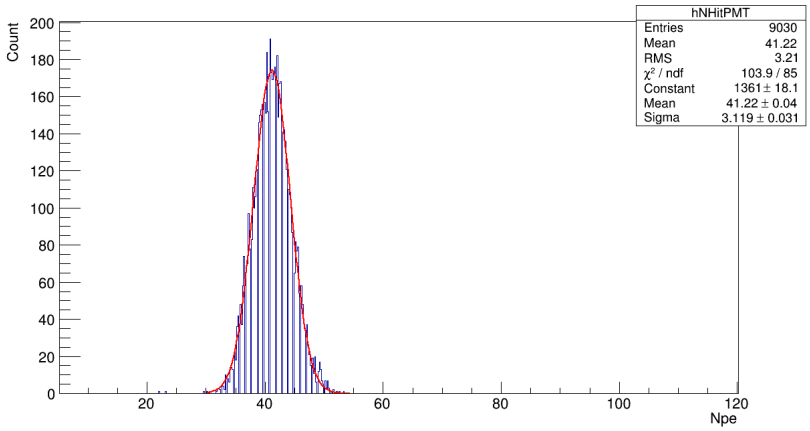

(a) Npe distribution for Acrylic light guide.

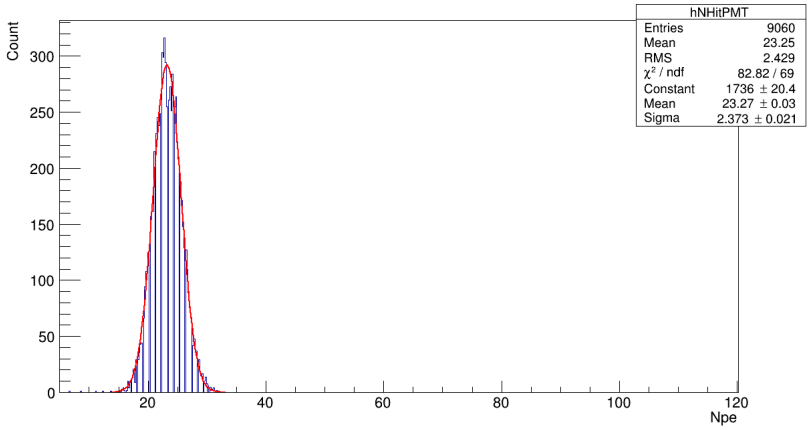

(b) Npe distribution for Miro Silver light guide.

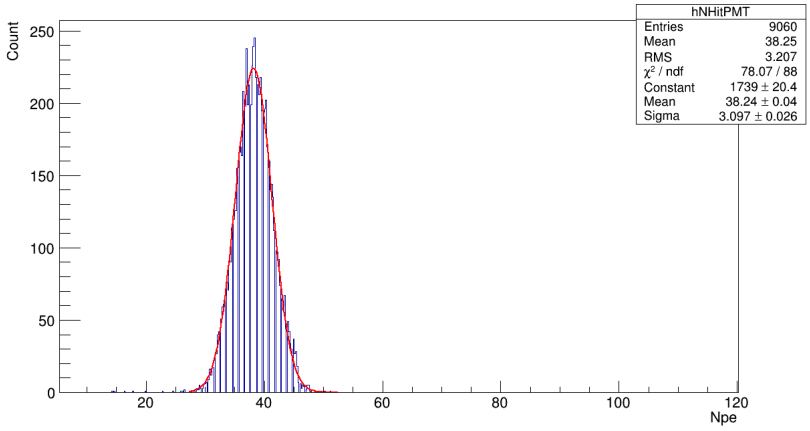

(c) Npe distribution for Miro-2 light guide.

FIG. 4.7 Number of photoelectrons distribution for Acrylic, Miro Silver and Miro–2 light guides obtained from simulations of the ^{241}Am source test experiment. Vertical scales are not the same for all distributions.

4.4 Experimental tests

4.4.1 Prototype detector description

A study of the number of photons collected from the glass stack was performed using prototype detectors at the University of Manitoba. These were constructed using as reference the description made in Section 3.3. In all setups, the detector consisted of a glass stack, a light guide and a photomultiplier; most of these elements were provided by the University of Winnipeg except for the air–core lightguides that were built at the University of Manitoba.

The glass stack was constructed by optically bonding glass types GS20 and GS30. They appear identical. The PMT used for experimental tests was a Hamamatsu R7600U; the glass stack and the photomultiplier were common elements of all experiments. Two different experimental setups were considered: one for the acrylic light guide and another for air–core lightguides.

- **Acrylic light guide**

  This prototype detector consists of a glass stack, an acrylic light guide and the PMT, as specified in section 3.3. The acrylic light guide (see Figure 4.8) was provided by the University of Winnipeg, and it was cleaned prior to use in the setup. After cleaning, this light guide was wrapped with aluminized mylar and bonded with the glass stack and PMT, using optical grease.

  In order to keep all the components together, a metallic box was adapted to hold the PMT and light guide in contact by using clamps (see Figure 4.9); the glass stack did not need to be fixed using an external support, since the optical grease was enough for this purpose. A ^{241}Am source was placed right above the glass stack and the entire setup was placed inside a black box as shown in Figure 4.10; once the box was closed, it was covered with a black cloth to prevent light from entering.

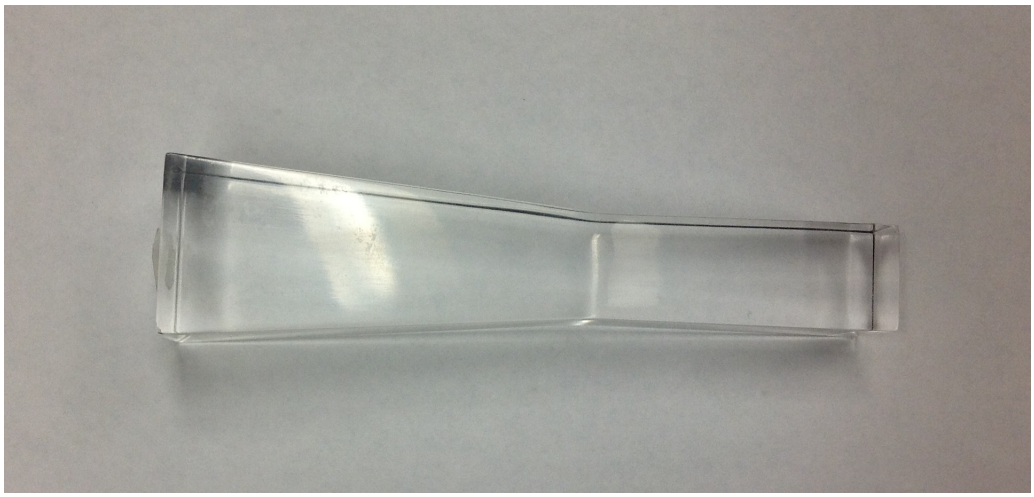

FIG. 4.8 Acrylic light guide used in experimental test.

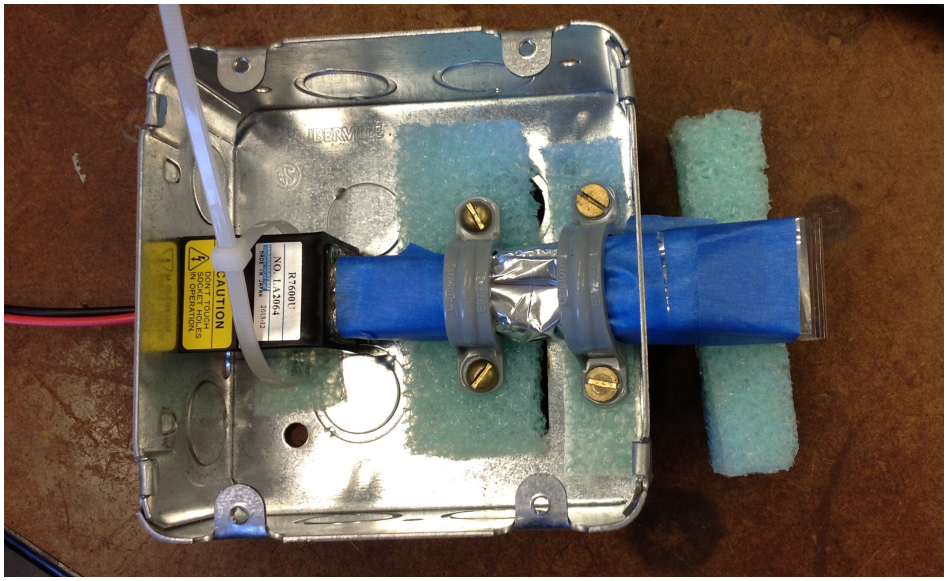

FIG. 4.9 Prototype detector using the acrylic light guide.

- **Air–core light guides**

  Air–core lightguides were constructed from two different pieces of material, Miro Silver and Miro–2. These were folded into a rectangular form to build each tube (dimensions 18mm×18mm×12cm), and then wrapped with black electrical tape. The resulting light guides are shown in Figure 4.11. In order to support and couple the PMT to the air–core light guides, a plastic rectangular tube was built, with

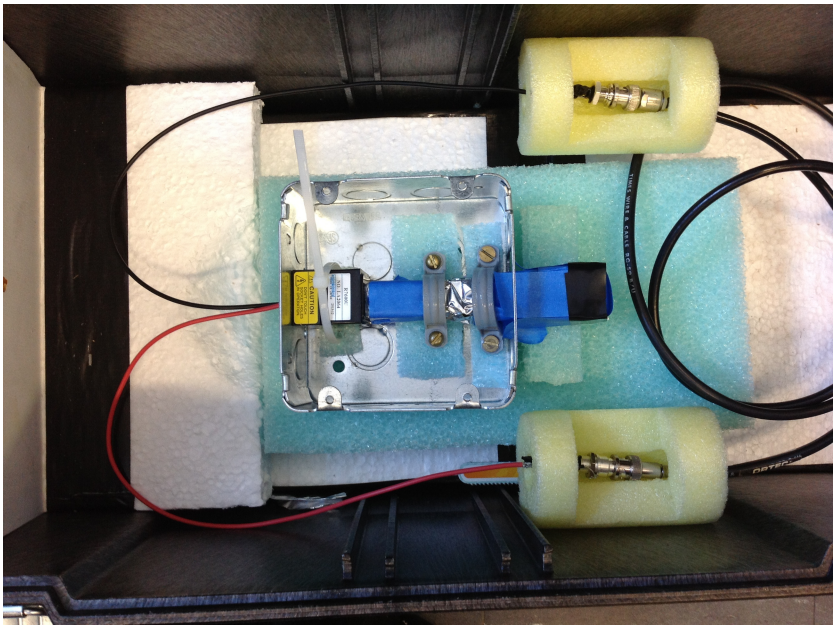

FIG. 4.10 Prototype detector using the acrylic light guide; the set up was placed inside the dark box.

dimensions 30mm×30mm×13cm (see Figure 4.12). Air–core lightguides were placed inside this rectangular box between foam spacers in order to keep them in the center of the larger plastic tube, in such a way that the effective area of the PMT matched with the area of air–core lightguides (see Figure 4.13). The Americium source was attached to a piece of foam and placed close to the entrance of the light guides (∼ 5mm apart); the complete set up for these prototype tests is shown in Figure 4.14. Finally, this assembly was placed inside a black box and covered with a black cloth, to perform the experiment.

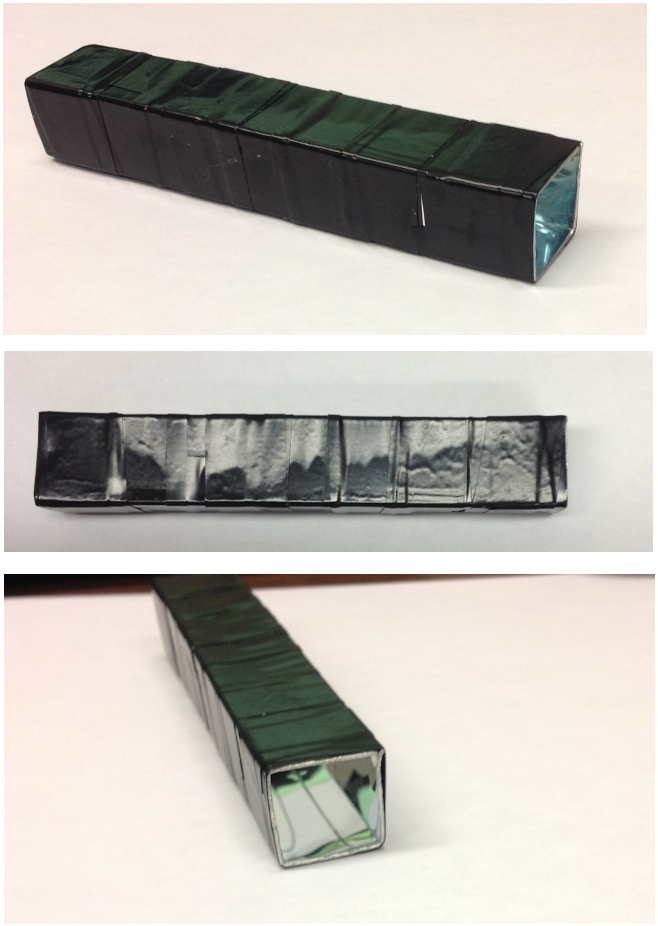

FIG. 4.11 Air-core light guides built using Miro Silver and Miro-2 materials.

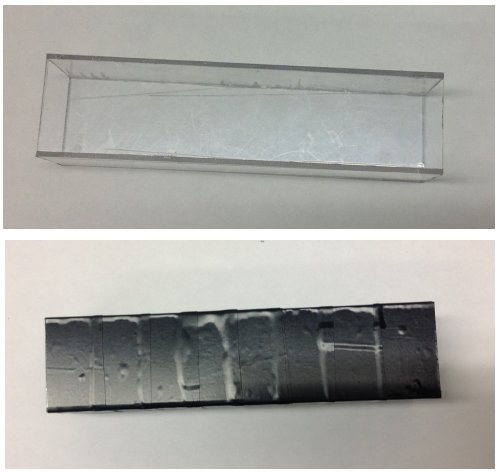

FIG. 4.12 Plastic box used to construct prototype detector for air-core light guides.

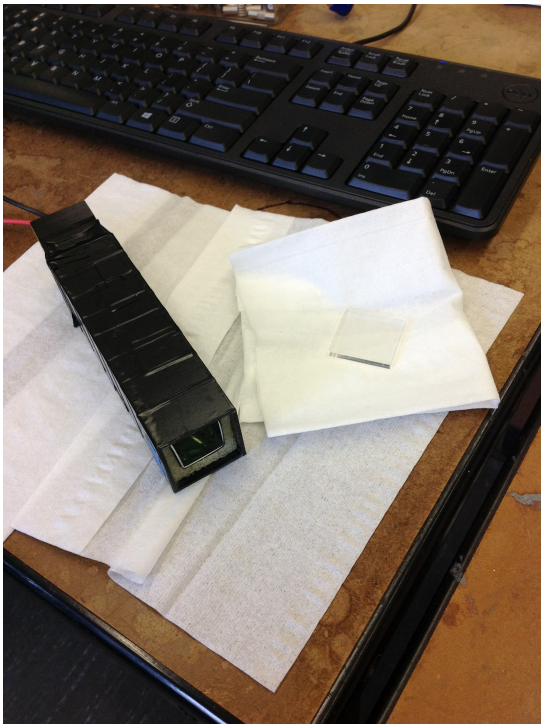

FIG. 4.13 To the left, prototype detector for air-core light guides. To the right, glass stack before placing it at the top of the plastic box.

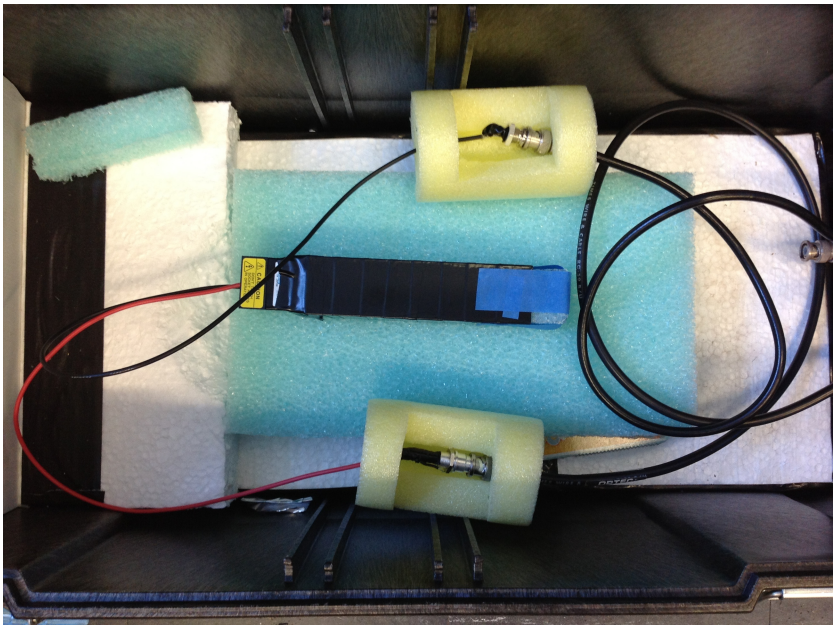

FIG. 4.14 Prototype detector for air–core light guides inside the black box.

4.4.2 Data Acquisition System

The incoming signal from the PMT was sent to an electronic system which processed the output and was read by a computer. The data acquisition system (DAQ) consisted of an amplifier, discriminator and Charge–to–Digital Converter (QDC) as shown in Figure 4.16. In order to communicate with these devices, a data acquisition program was needed. The setup used CAEN VME boards and the DAQ program was based on the basic software provided by CAEN. A brief discussion about each element is given below.

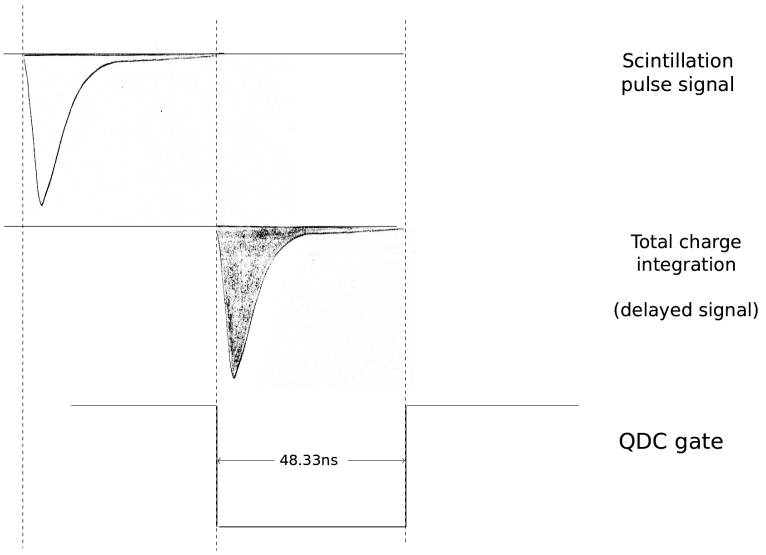

Fig. 4.15 Timing diagram of the QDC gate and the output signal from the PMT.

- **High voltage source**

  The photomultiplier was biased with a negative high voltage of -800V, from an *ORTEC 428 High voltage power supply*, which has an output range between 0 and 1000 V, of positive or negative polarity.

- **Amplifier V974**

  Since the PMT signal obtained was small, amplification was required. A *CAEN V974 Amplifier* was used for this purpose; it consisted of 4 channels, with a maximum gain of 10 in each of them. The gain of the experimental setup was 10.

- **Discriminator V814**

  The *CAEN Discriminator V814* corresponds to a 16 Channel Low Threshold Discriminator [CAE15a]. The discriminator was used to generate a gate that had a specific duration, which was used to trigger the QDC. The communication with this unit was done via VME, by introducing a 8-bit word. Two parameters need to be set: the threshold, which can be programed to a value between -1 mV and -255 mV, and the width, which can be selected between 6 and 95 ns. For the purpose of our experiment, a gate of 48.33 ns was configured and used as a trigger for the delayed gate signal of the QDC, which integrated the collected charge (see Figure 4.15).

- **QDC V792**

  The *CAEN QDC V792 Charge–to–digital converter* was used to integrate the input signal. The input range of the charge is between 0 and 400 pC. This unit has 32 conversion channels, of which only channel 0 was used in our experiment. There is one gate input common to all channels, used to define the signal integration time.

  The input charge was converted into a voltage value inside the QDC[5] by a Charge to Amplitude Conversion (QAC) stage, with an ADC channel resolution of 1 mV. In this way, the input analog signal is converted into a digital value (ADC count), which is proportional to the input charge:

$$\begin{aligned} Q &= C \times V \\ &= 0.1 \times \text{channel} \quad (\text{pC}) \,. \end{aligned}$$

[5]The internal capacitance is 100 pF [CAE15b].

From the expression above, the value of the input charge in terms of ADC channels from the pedestal and data is:

$$\mathrm{Q} = 0.1 \times (\mathrm{ADC}_{Data} - \mathrm{ADC}_{Pedestal}) \quad \mathrm{pC}, \tag{4.2}$$

where $\mathrm{ADC}_{Pedestal}$ is the chrage recorded by the ADC for zero input signal.

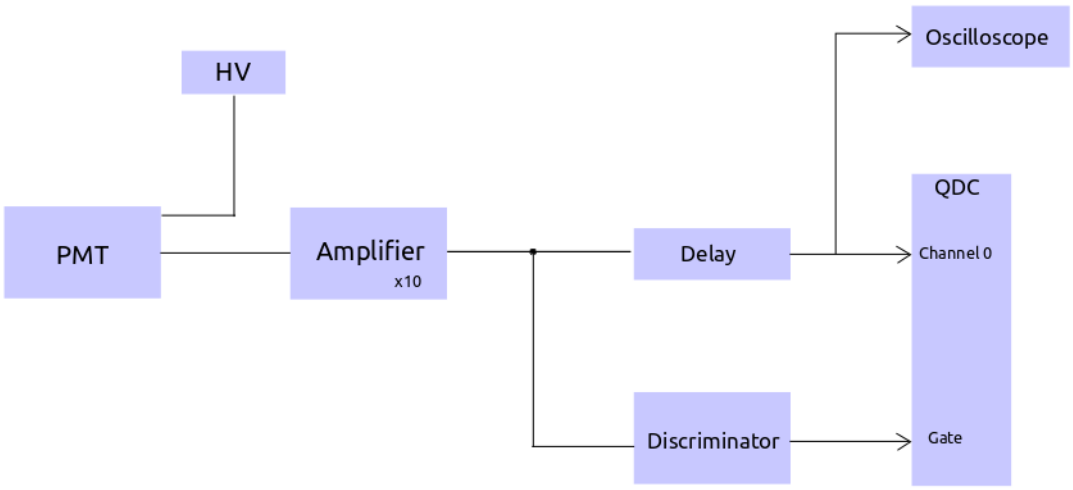

FIG. 4.16 A schematic diagram of the DAQ for the experimental set up.

- **Connection via VME**

  The DAQ software has an interface adapted to the Linux operating system, denoted The CAEN VME Manual Controller. The CAEN Software provides a program denoted CAENVMEDEMO which is used to communicate with one board at a time; this process is done via an *Optical Link V2718* which transmits the information to a desktop computer. The CAENVMEDEMO program opens a terminal session in Linux, and a screenshot of this window is shown in Figure 4.17. In order to work with a specific unit, the BASE ADDRESS must be introduced. Other values such as ADDRESS are adjusted according to the parameters required in the experiment, following the instructions in each manual [CAE15a] [CAE15b].

Options READ and WRITE are available during the entire process to read and introduce information from the board. Experimental data were read after each event and accessed in *Chained Block Transfer mode* [CAE15c], which in turn was saved in a text file on the hard drive. The file has a register of counts per channel in the form of 12-bit values. Collected files were processed, but only data from channel 0 were saved for analysis. This information was converted from hexadecimal to a decimal number. Finally, frequency histograms were constructed from data collected using ROOT. A C++ program was written in order to perform the data analysis.

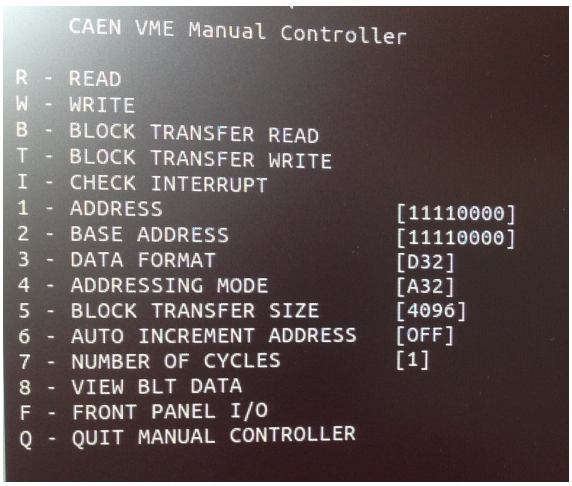

FIG. 4.17 Screenshot of terminal session in Linux for the CAEN VME Manual Controller.

4.4.3 EXPERIMENTAL RESULTS

The output signal from the PMT was amplified and split into two intermediate signals; one signal was delayed and sent to the QDC for integration to deduce the charge collected at the PMT; the other was discriminated and used to build a gate to define the QDC integration time. An oscilloscope was used to monitor the signals coming from the QDC and discriminator (see Figure 4.16). In total, 9060 events were collected by the data acquisition system for each prototype test. A photo of the experimental setup for prototype testing is shown in Figure 4.18.

To calibrate the QDC, pedestal measurements were performed in our experiment. A

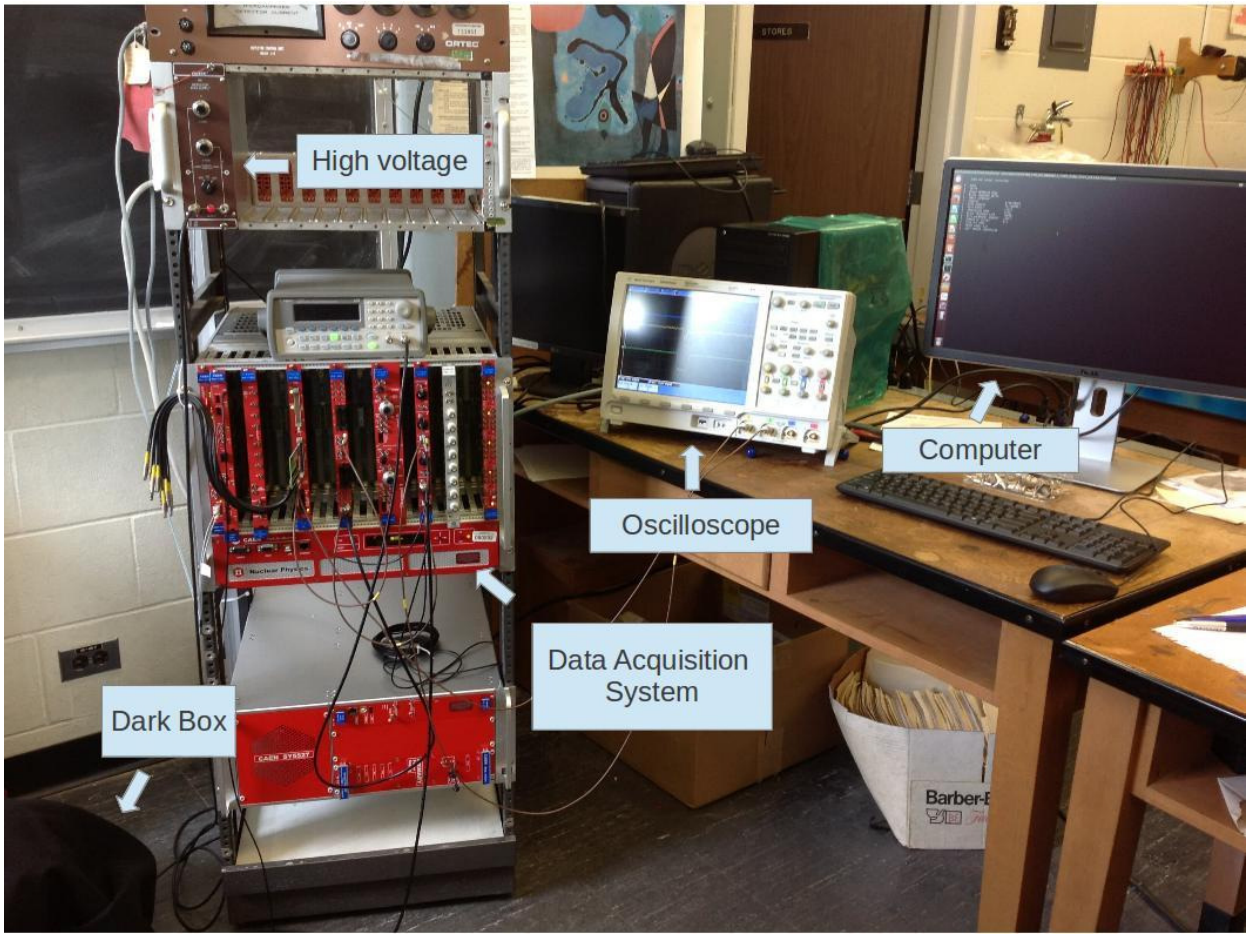

FIG. 4.18 Experimental setup for prototype tests including data acquisition system.

pedestal is the measurable offset value when no signal is present. This was done by adding a new QDC gate signal to the system from an *Agilent 33220 20MHz Waveform generator*, without altering the original experimental setup. The signal from this unit was input to a different channel in the discriminator. Since the generator signal was out of time with the ^{241}Am source events, it would cause the QDC to integrate a "zero input" pulse condition and thus allow the QDC zero channel to be determined. When all events were integrated by the QDC, these zero deposited charge events formed a visible peak which could be collected simultaneously with data from the ^{241}Am source. The introduced pulse was chosen to have a similar duration and frequency to that generated by the discriminator in each test of the detector prototype[6]. Via this technique, histograms showing alpha source

[6]The width of the pulse was chosen to be 50 ns in all cases; frequency values were adjusted in each

data along with pedestal values in ADC counts, were obtained, as illustrated in the next section.

- **Acrylic light guide**

  For the prototype detector using the acrylic light guide, an oscilloscope trace showing the analog PMT signal was obtained from the data acquisition system as shown in Figure 4.19. These results were analyzed and plotted in ROOT; Figure 4.20 shows the results for the pedestal and ADC values for the prototype test with the acrylic light guide. Spectra were obtained using a gate of 48.33 ns and a threshold value of 30 mV in the discriminator. Additionally, a Gaussian fit was performed for each peak in order to find values for the mean, needed for subtracting the pedestal from the source data. These results are summarized in Table 4.3.

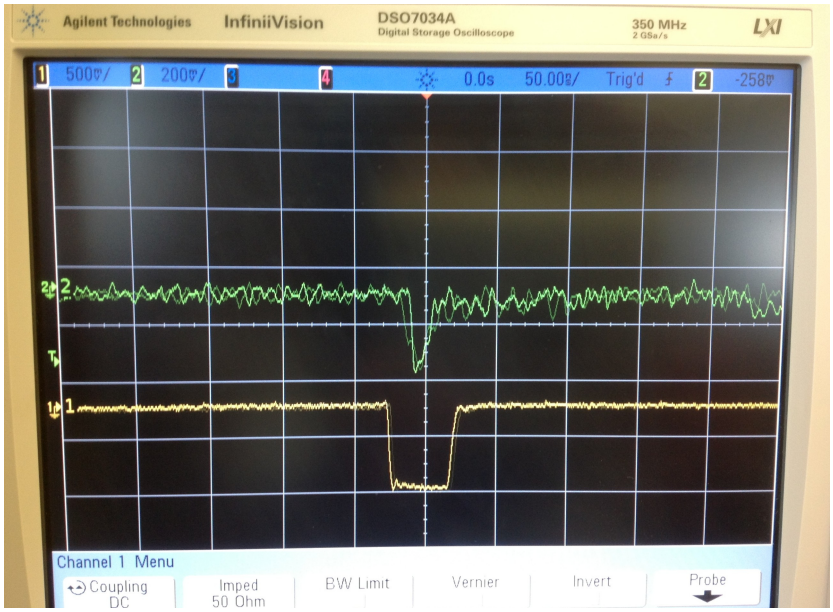

FIG. 4.19 Signal obtained from PMT, after amplification, using the prototype detector with the acrylic light guide and a ^{241}Am test source. Oscilloscope scale settings are 50 ns and 200 mV per major scale division.

Once the results for data and pedestals were obtained, these were converted into charge by using equation 4.2. The charge is proportional to the number of photo-electrons (N_{pe}) produced by scintillation light as follows:

experiment.

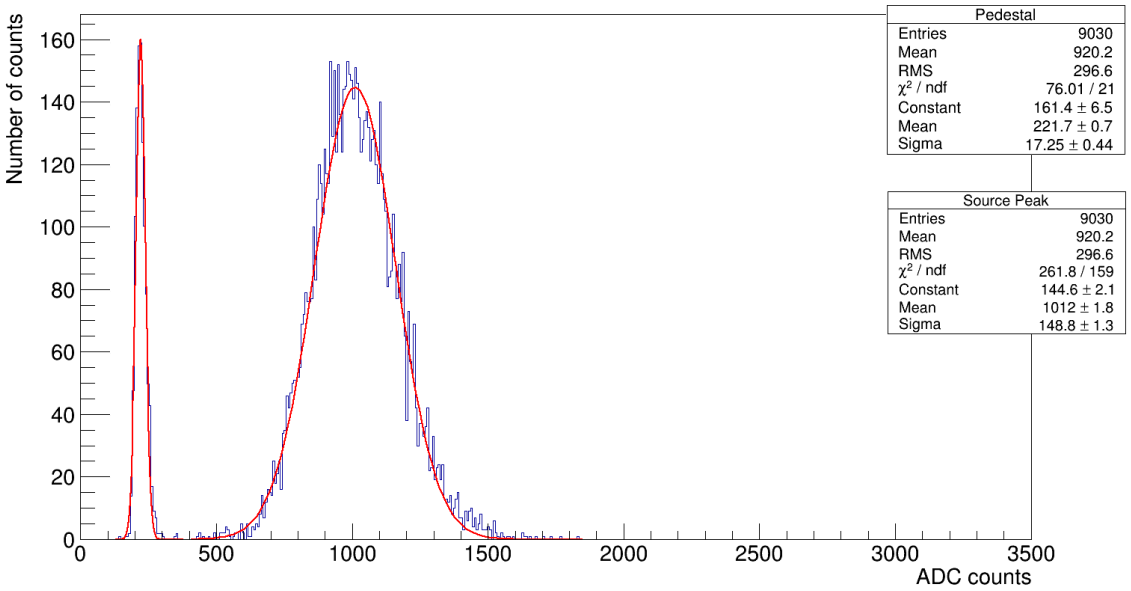

FIG. 4.20 Experimental data for the prototype detector using an acrylic light guide and a ^{241}Am test source. Gaussian fits have been adjusted to the pedestal (left graph) and data (right graph) spectra. The statistical information of the Gaussian distributions are placed in the top and bottom boxes for the pedestal and source peak, respectively.

$$Q = N_{pe} \times q_e \times G_{Amplif} \times G_{PMT}, \tag{4.3}$$

where q_e denotes the charge of the electron, G_{PMT} is the gain of the photomultiplier and G_{Amplif} the gain due to the amplifier, whose values are given in Table 4.4. The PMT gain was taken from the manufacturer's specifications for the applied high voltage. It is assumed to be accurate to $\pm 5\%$. From equations 4.2 and 4.3, a relation for the number of photoelectrons in terms of the mean ADC values for data and pedestal was obtained. This resulting expression was introduced in the C++ program used for data analysis, in order to generate histograms for the number of photoelectrons for the prototype detector with the acrylic light guide, as shown in Figure 4.21.

	Mean (ADC counts)	Standard deviation
Pedestal	(221.7 ± 0.7)	(17.2 ± 0.4)
Data	(1012 ± 2)	(149 ± 1)

TABLE 4.3 Table with values of mean (μ) and standard deviation (σ) from Gaussian fits. These results were obtained using the prototype detector with an acrylic light guide, and a ^{241}Am test source.

q_e	G_{PMT}	G_{Amplif}
1.6×10^{-19}	1.8×10^{6}	10

TABLE 4.4 Table with values for the electron charge and the gain.

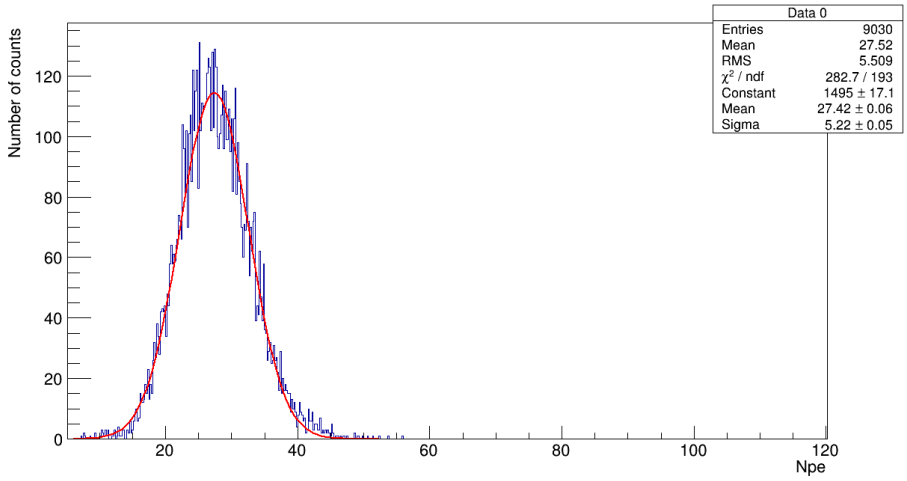

FIG. 4.21 NPE spectrum for the prototype detector using an acrylic light guide and a ^{241}Am test source. A Gaussian distribution was fitted to the data.

- **Air-core light guides**

  Figure 4.22 shows an oscilloscope trace of the PMT output signal from electronics for the prototype detector with the Miro Silver air-core lightguide. Spectra were obtained using a gate of 48.33 ns and a threshold value of 24 mV, in both experimental tests (Miro-2 and Miro Silver).

  For the ^{241}Am source, distributions for data and pedestal in ADC values were obtained. Each peak was fitted with a Gaussian in order to find mean values of the

pedestal and data, which were used to extract the experimental results. These graphs are shown in Figures 4.23(a) and 4.23(b) for Miro Silver and Miro-2, respectively. Values for the mean and standard deviation from these graphs are shown in Tables 4.5 and 4.6. Distributions for the number of photoelectrons are obtained, as shown in Figures 4.24(a) and 4.24(b) for Miro Silver and Miro-2, respectively.

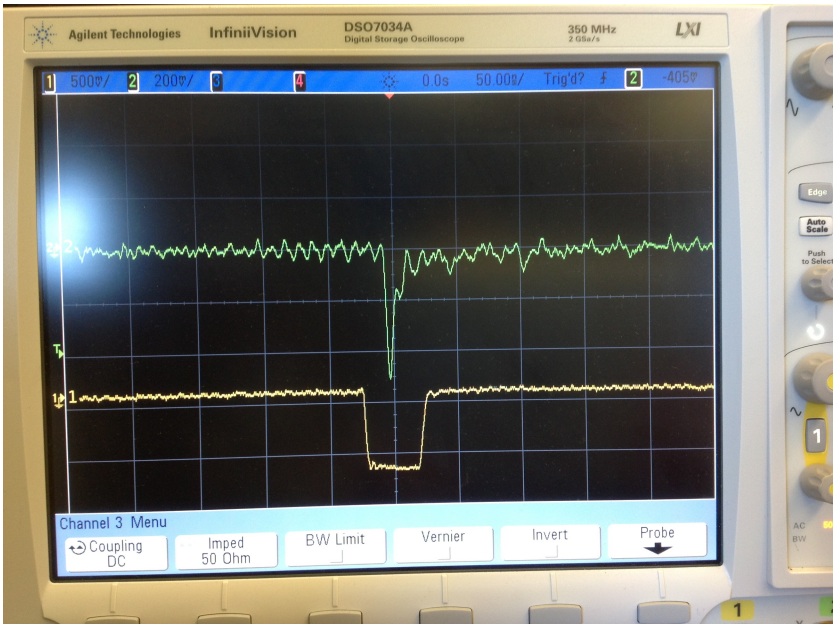

FIG. 4.22 Signal obtained from the PMT, after amplification, using the prototype detector with the Miro Silver light guide and a ^{241}Am test source. Oscilloscope scale settings are 50 ns and 200 mV per major scale division.

	Mean (ADC counts)	Standard deviation
Pedestal	(238.8 ± 0.7)	(22.0 ± 0.4)
Data	(786 ± 1)	(117 ± 1)

TABLE 4.5 Table with values of mean (μ) and standard deviation (σ) from Gaussian fits. These results were obtained using the prototype detector with a Miro Silver light guide, and a ^{241}Am test source.

	Mean (ADC counts)	Standard deviation
Pedestal	(178.7 ± 0.4)	(10.3 ± 0.4)
Data	(882 ± 2)	(154 ± 1)

TABLE 4.6 Table with values of mean (μ) and standard deviation (σ) from Gaussian fits. These results were obtained using the prototype detector with a Miro-2 light guide, and a ^{241}Am test source.

A summary of experimental values obtained from spectra of the number of photoelectrons is shown in Table 4.7. The prototype with the acrylic light guide had a significantly greater number of photons collected by the PMT, compared to the air–core light guides; the Miro Silver guide delivered about 30% fewer photons to the PMT.

Light guide	Mean (Npe)	Standard deviation
Acrylic	(27.42 ± 0.06)	(5.22 ± 0.05)
Air–core Miro–2	(24.43 ± 0.06)	(5.32 ± 0.04)
Air–core Miro Silver	(18.99 ± 0.05)	(4.00 ± 0.04)

TABLE 4.7 Table with values of mean (μ) and standard deviation (σ) from Gaussian fit. These results were obtained from experimental tests of the prototype detector using different light guides and a ^{241}Am test source.

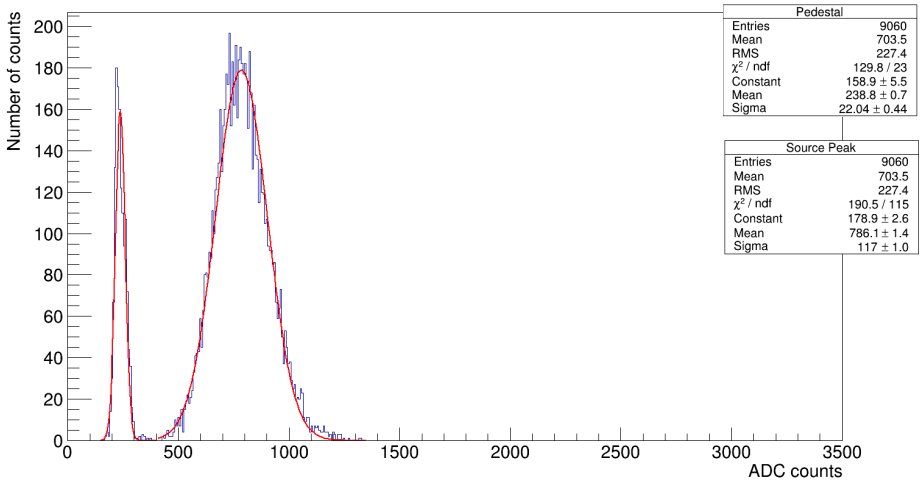

(a) Experimental data using a Miro Silver light guide.

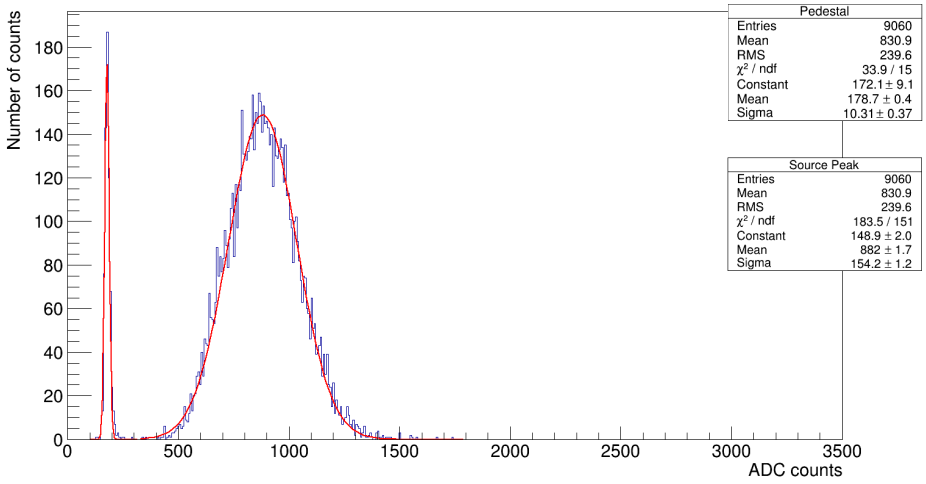

(b) Experimental data using a Miro-2 light guide.

FIG. 4.23 Experimental data for the prototype detector using acrylic, Miro Silver and Miro–2 light guides and a ^{241}Am test source. Gaussian fits have been made to the pedestal (left graph) and data (right graph) peaks. The statistical information for the Gaussian distributions are placed in the top and bottom boxes for the pedestal and source peak, respectively.

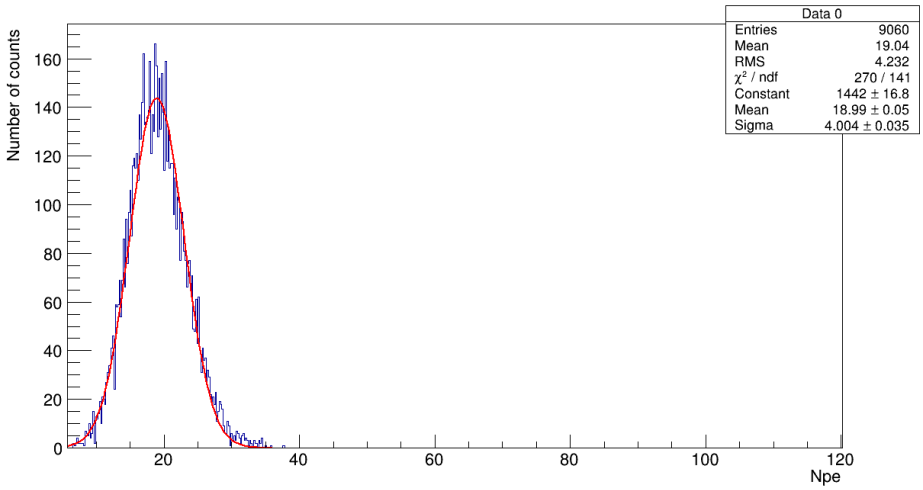

(a) Npe distribution for Miro Silver air-core light guide.

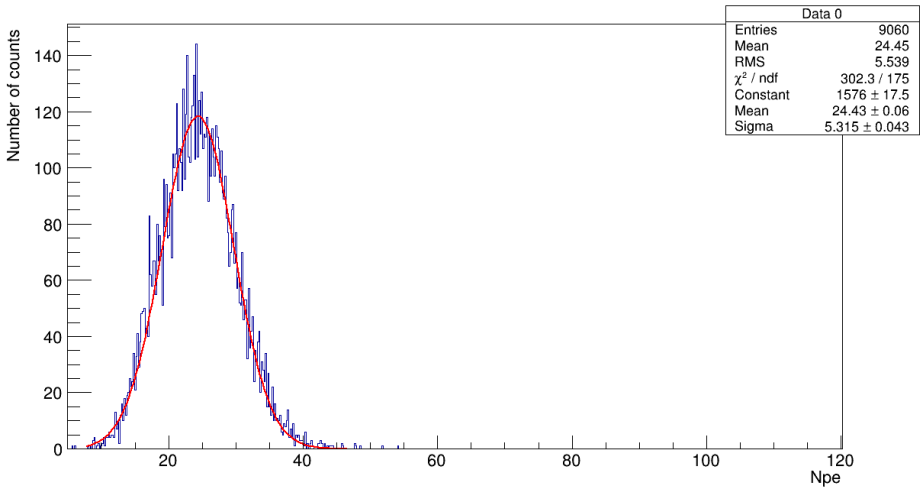

(b) Npe distribution for Miro-2 air-core light guide.

FIG. 4.24 NPE spectrum for the prototype detector using an Acrylic, Miro Silver and Miro-2 light guides and a ^{241}Am test source. A Gaussian distributions were fitted to the data.

4.5 Comparison of results

Distributions for source test data collected from the PMT can be compared with those obtained from Geant4 simulations. Experimental results were discussed in subsection 4.4.3; simulation results were discussed in subsection 4.3.3. All spectra obtained proved to be normally distributed; therefore, a Gaussian fit was applied to each of these graphs, and values for the mean and standard deviation found from this process, were summarized in Tables 4.1, 4.2 and 4.7.

4.5.1 Alpha source simulations vs Experimental tests

Results for the number of photoelectrons obtained from the simulation of the prototype detector using an alpha source were compared with those found in experimental tests. A superposition of both distributions (simulated and experimental) was made for visual comparison; a typical graph is shown in Figure 4.25 for the prototype detector with the acrylic light guide and the ^{241}Am test source. As seen in the figure, the peak of the simulation distribution is at significantly larger Npe and is about 40% narrower than the test data.

A comparison of all Npe simulations and experimental tests is given in Table 4.8. Values for the collected number of photoelectrons are listed in descending order; the best light collection is obtained using the prototype detector with the acrylic light guide, followed by the one with a Miro–2 light guide and Miro Silver in the last place. This behaviour is observed for both experimental and simulation results.

Table 4.8 also shows the ratio of simulation to experiment values for the mean and standard deviation, for the different light guides of the prototype detector. While both simulation and experiment are in agreement on the relative performance of the three light guides under consideration, the simulations overpredict the observed values by around 50%, with somewhat better agreement for the Miro Silver case. This latter may be due to the fact that the spectrum of the reflectivity as a function of the wavelength was provided directly by the manufacturer, which led to more accurate simulation results. Overall sources sources of disagreement may include imperfect knowledge of the reflectivity as a

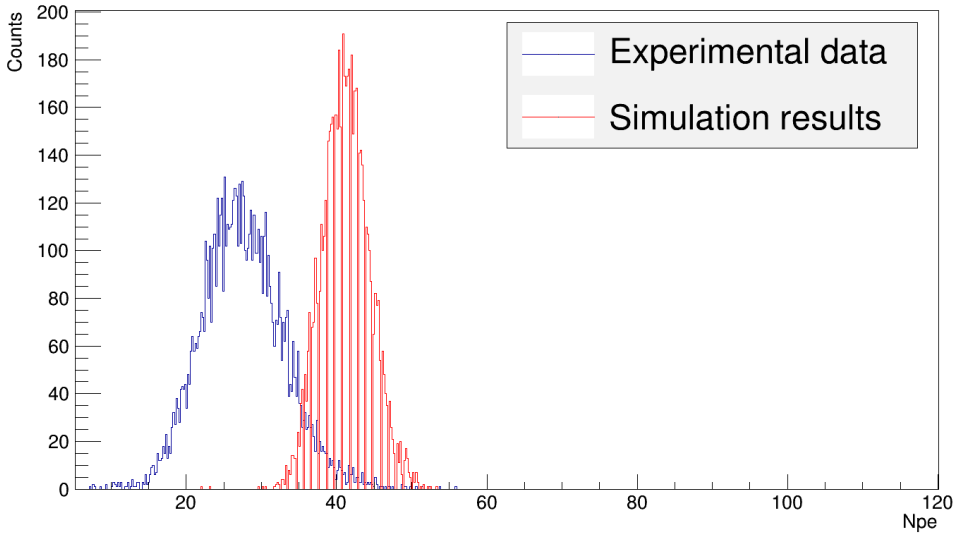

FIG. 4.25 Superposition of distributions for the number of photoelectrons obtained for the prototype detector with the acrylic light guide for a total of 9030 events: to the right, the spectra from the simulation using an ^{241}Am test source; to the left, the spectra from experimental test using an ^{241}Am test source.

function of wavelength for the simulations, imperfections in the light guide fabrication, and innacurate knowledge of the PMT gain, which was not separately measured. Considering standard deviation values, those obtained from experimental tests are larger than from the Geant4 simulations. This suggests the presence of a factor contributing to the broadening that was not considered in the simulations (as will be discussed later in this chapter), leading to a ratio among values around 0.6 for each light guide. Similar conclusions can be stated when comparing simulated and experimental data for all 3 light guides.

	μ_{sim} (Npe)	μ_{exp} (Npe)	μ_{exp}/μ_{sim}	σ_{sim} (Npe)	σ_{exp} (Npe)	Ratio
Acrylic	41.22±0.04	27.42±0.06	0.66	3.12±0.03	5.22±0.05	0.60
Air–core Miro-2	38.24±0.04	24.43±0.06	0.64	3.01±0.03	5.32±0.04	0.57
Air–core Miro Silver	23.27±0.03	18.99±0.05	0.82	2.37±0.02	4.00±0.04	0.59

TABLE 4.8 Table with values of mean (μ) and standard deviation (σ) from Gaussian fits to the Npe distributions, and a ratio between different values which is used for comparison. These results were obtained using experimental and simulation results for the prototype detector with different light guides, using a ^{241}Am test source.

One class of systematic error in the simulations is due to incomplete knowledge of the optical properties of the materials used. Firstly, we do not know for the Miro–2 air–core light guide the specific relation between wavelength and reflectivity for this material. The manufacturer states a reflectivity value >95%. The values implemented in the simulation are based on the Figure G.1[7], and the experimental measurements performed by R. López in [Lóp10]. Similarly, the values implemented in the simulation of reflectivity and wavelength for Aluminized Mylar were not directly provided by the manufacturer, which could have also contributed to the error in our simulation results. We also had no information on the reflectivity as a function of incident angle; it was assumed to be angle–independent in the simulations.

Secondly, the simulation was performed using a simplified model for the 241-Americium source. The simulation was performed using monoenergetic alpha particles (5.49 MeV and 5.01 MeV for acrylic and air–core light guides, respectively, as described in section 4.3.2). The energy values take into account the approximate distance that alpha particles traveled in air from the alpha source to the scintillator glass, according to experimental conditions. The initial energies are only an average value from a range of high–energy alphas and low–energy gamma rays[8] emitted by the ^{241}Am test source. The latter is related to the broadening of distributions, and an estimation of this effect gives a value of $\sigma \sim 5.2$ p.e., close to what is observed.

The experimental factors that might have contributed to systematic errors include the following. First, the glass stack was not wrapped with any reflective material which might have led some photons to escape from the scintillator. In addition, during the experimental test using the acrylic light guide, it is possible that a reduction of the contact area of the light guide with the PMT (e.g. a portion of the area might have been unstuck while performing the experiment) may have occurred, reducing the number of collected photoelectrons.

As mentioned in subsection 4.4.1, air-core light guides were manually constructed,

[7]This graph contains a generalization for Miro materials and does not corresponds to the specific case of Miro–2.

[8]The 241–Americium source emits alphas with the following energies: 5.443 MeV (13.0%), 5.486 MeV (84.5%) and 5.388 MeV (1%) [F+15].

and some defects on the final ends of these light guides may have remained. This could contribute to some light losses at the very end of the tubes, instead of being reflected, resulting in a reduction of the number of photons collected by the PMT in these cases.

Other aspects that might have contributed to systematic errors in test experiments and simulations, are the values of the Gain and Quantum efficiency of the PMT. We did not perform an experimental measurement of these values and we used the values provided by the manufacturer [Ham14] in the simulations, which may not be accurate for our particular unit.

4.5.2 Comparison of neutron capture and α source simulations

Spectra obtained from simulation results for neutron captures in the glass stack, and those from simulations of the ^{241}Am source, can be also placed in the same graph for visual comparison. A typical normalized graph from this procedure is shown in Figure 4.26. As seen in the figure, the two peaks are almost identical.

	μ_{simN} (Npe)	μ_{simA} (Npe)	μ_N/μ_A	σ_{simN} (Npe)	σ_{simA} (Npe)	Ratio
Acrylic	37.25±0.03	41.22±0.04	0.90	2.96±0.02	3.12±0.03	0.95
Air–core Miro-2	37.31±0.03	38.24±0.04	0.98	2.91±0.02	3.10±0.03	0.94
Air–core Miro Silver	22.63±0.02	23.27±0.03	0.97	2.31±0.02	2.37±0.02	0.98

Table 4.9 Table with values of mean (μ) and standard deviation (σ) from Gaussian fit, and a ratio between different values which is used for comparison. These results were obtained using simulation results of the prototype detector with different light guides. Simulations were performed for an alpha source (μ_{simA} and σ_{simA}) and neutron capture in the glass stack (μ_{simN} and σ_{simN}).

Table 4.9 shows the ratio of the mean and standard deviation values for both simulations of the prototype detector. The ratio of the simulated mean Npe for neutron capture and the α source in all light guides, gives a value close to unity. This suggests that comparisons between data from ^{241}Am test source experiments and alpha source simulations can be extended to the other simulations in this work; i.e., experimental tests may be

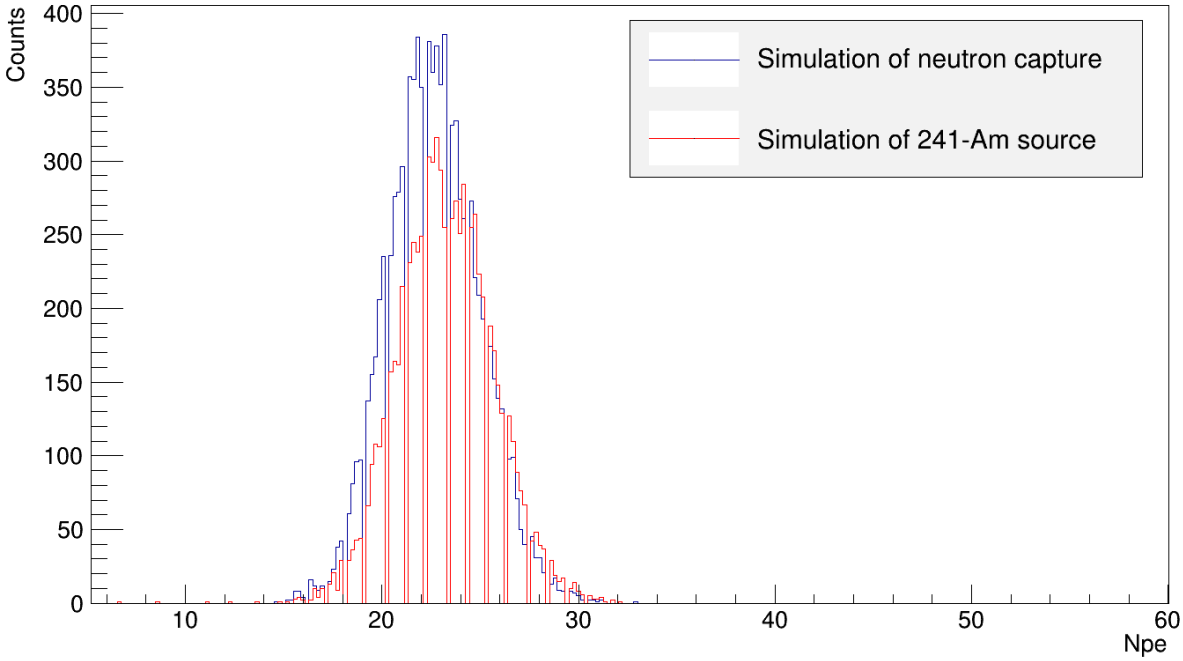

FIG. 4.26 Superposition of distributions for the number of photoelectrons obtained for the prototype detector with the Miro Silver light guide: the red graph, the spectra from simulation of ^{241}Am test source; the blue graph, the spectra from the simulation of neutron capture in the glass stack.

used to benchmark simulations of the distribution of photons for the prototype detector obtained from neutron capture in the glass stack.

4.6 Geometry study

As studied so far, the light guide prototypes had two different geometries: a trapezoidal acrylic light guide with rectangular cross section, and rectangular air–core light guides. In this section, additional simulations of all three light guides having the same geometry are reported. Additionally, simulations were performed with different lengths of acrylic light guides (see subsection 4.6.3).

4.6.1 Light guides with rectangular shape

The acrylic light guide was simulated as a rectangular tube, with the same shape as was used for the air-core light guides. The results obtained are shown in Figure 4.27, for Acrylic, air–core Miro Silver and air–core Miro–2 light guides. The only difference compared to the previous study is that the acrylic light guide is now rectangular; its signal is more than doubled compared to the trapezoidal shape.

4.6.2 Trapezoidal lightguides

In this subsection, air–core light guides were simulated using the same geometry of the acrylic light guide. A trapezoidal shape with a rectangular cross-section was chosen for all light guides. The number of photoelectrons obtained from these simulations is shown in Figure 4.28. Compared with previous results, the signals obtained from the air–core light guides are suppressed about a factor of 2 in the trapezoidal geometry. The much smaller signals in these cases are not useful for the planned nEDM experiment.

4.6.3 Light guides of different lengths

A length of 12 cm was chosen for the light guides in the prototype detector. Other lengths for the light guide were simulated in Geant4 in order to observe the number of photoelectrons collected in each case: 0 cm, 6 cm and 18 cm. The results from these distributions were used to be compared with the mean and standard deviation values of the prototype detector with the acrylic light guide of 12 cm length (see Figure 4.30).

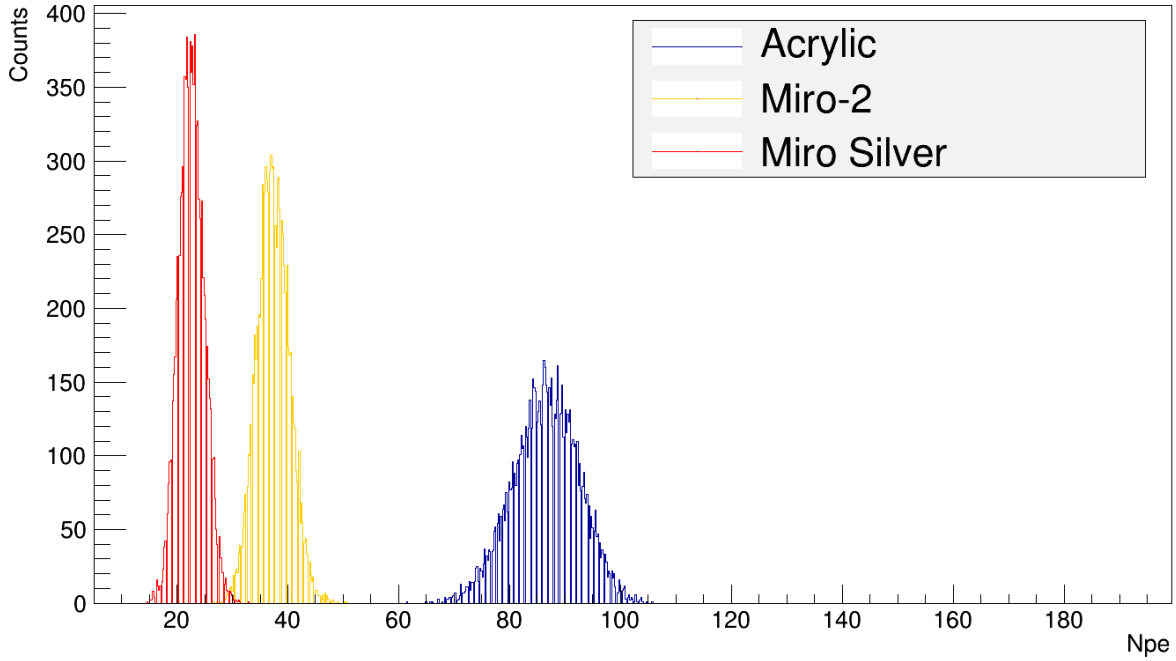

FIG. 4.27 Number of photoelectrons distribution for acrylic, Miro Silver and Miro-2 light guides obtained from neutron capture simulation. All light guides have a rectangular shape.

Without light guides (zero length), the number of photoelectrons is 390, which exceeds the value obtained with the acrylic light guide by a factor of about 10. The number of photoelectrons decreases as the length of the guide increases.

The simulated mean Npe versus length data in Table 4.10, are plotted as a function of the length in Figure 4.29. The resulting curve could not be fitted to a simple function (eg. exponential function). When the light passes through the acrylic light guide, is internally reflected at the boundaries for incident angles greater than the critical angle; the light suffers attenuation at every bounce and it will be greater for trajectories with a large number of bounces.

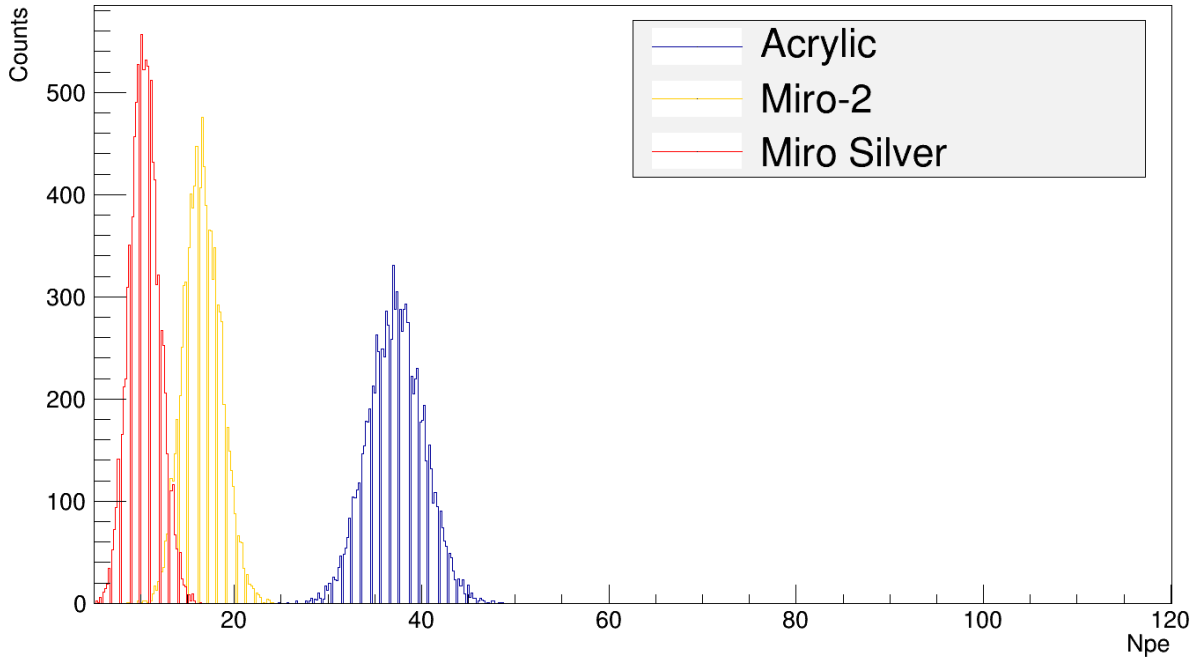

FIG. 4.28 Number of photoelectrons distribution for acrylic, Miro Silver and Miro-2 light guides obtained from neutron capture simulation. All light guides have a trapezoidal shape with rectangular cross section.

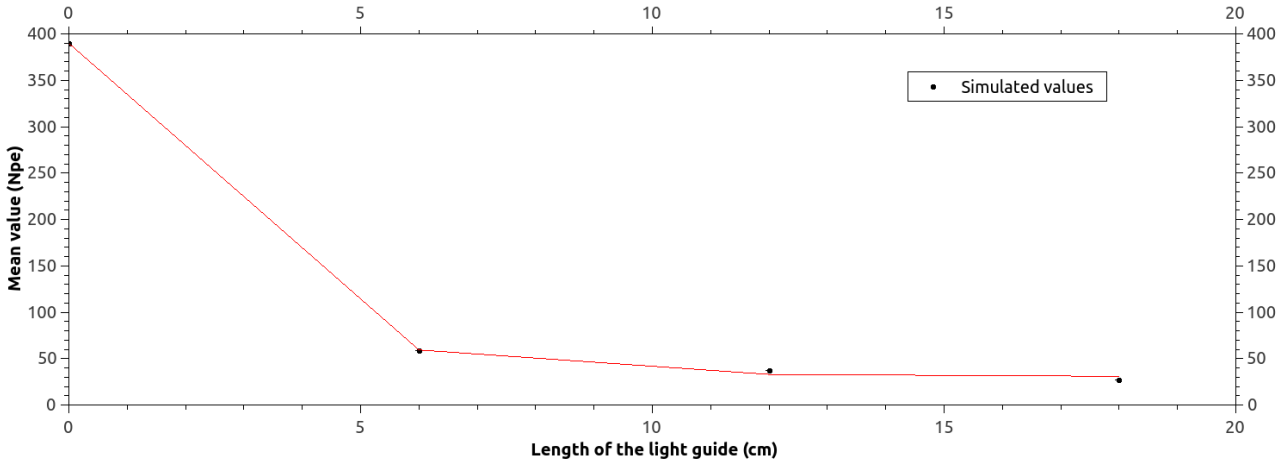

FIG. 4.29 Number of photoelectrons as a function of the distance for light guides of lengths 0 cm, 6 cm, 12 cm and 18 cm.

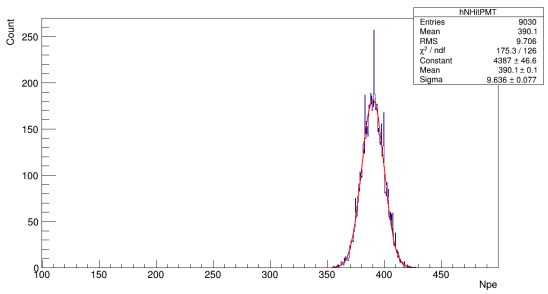

(a) Npe distribution without light guide.

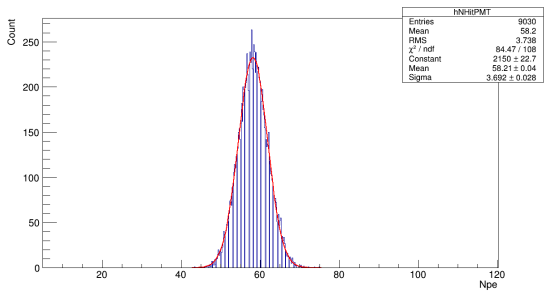

(b) Npe distribution for a light guide with a length of 6 *cm*.

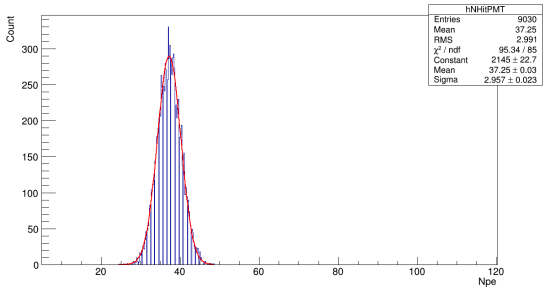

(c) Npe distribution for a light guide with a length of 12 *cm*.

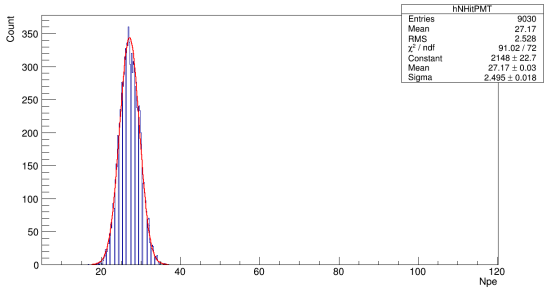

(d) Npe distribution for a light guide with a length of 18 *cm*.

FIG. 4.30 Number of photoelectrons distribution for the prototype detector without light guide and with an acrylic light guide of lengths 0 *cm*, 6 *cm* and 18 *cm*, obtained from neutron capture simulation.

A summary of the mean and standard deviation from Gaussian fits in Figures 4.27, 4.28 and 4.30, is shown in Table 4.10. The column including the ratio values, consists of the comparisons made between the acrylic light guide and air-core light guides for the first two cases. In the last part of the table, the comparison is between the prototype detector with the acrylic light guide of 12 *cm* long and the same prototype with light guides of different length. The same calculation was performed for the standard deviation in each case; the results showed that in cases where the number of photoelectrons was significantly larger, the width of the Gaussians were also higher.

	Materials	μ_{sim}	Ratio	σ_{sim}	Ratio
Rectangular shape (subs. 4.6.1)	Acrylic	(86.48±0.06)	—	(5.89±0.05)	—
	Miro–2	(37.31±0.03)	2.32	(2.91±0.02)	2.02
	Miro Silver	(22.63±0.02)	3.82	(2.31±0.02)	2.55
Trapezoidal shape (subs. 4.6.2)	Acrylic	(37.25±0.03)	—	(2.96±0.02)	—
	Miro–2	(16.63±0.02)	2.24	(1.94±0.01)	1.47
	Miro Silver	(10.41±0.02)	3.58	(1.59±0.01)	1.80
Different lengths (subs. 4.6.3)	0 *cm*	(390.1±0.1)	—	(9.64±0.08)	—
	6 *cm*	(58.21±0.04)	—	(3.69±0.03)	—
	12 *cm*	(37.25±0.03)	—	(2.96±0.02)	—
	18 *cm*	(27.17±0.03)	—	(2.50±0.02)	—

TABLE 4.10 Values obtained from Gaussian fits of distributions in Figures 4.27 and 4.28 and 4.30. The ratio is calculated in each category as the ratio of the first value to the others.

5

SUMMARY AND OUTLOOK

The proposed nEDM experiment at TRIUMF plans to make use of the anticipated highest density of ultra-cold neutrons in the world, to achieve a new precise limit on the measurement of the neutron Electric Dipole Moment. A high rate of UCN requires detectors capable of high counting rates. A multi–element detector that satisfies this requirement consists of ^{6}Li–doped glass scintillators, light guides and photomultipliers.

The main focus of this work was in the study of the light collection of a prototype ^{6}Li glass detector for three different materials of light guide: acrylic, air–core Miro Silver and air–core Miro–2. This process was carried out in two parts: simulations in Geant4, and data taking and analysis performed at the University of Manitoba. The first stage concerns a simulation of the prototype detector for neutron capture in the glass stack. In addition, simulations with an alpha source were performed to be compared with the experimental tests. Both the results from alpha source simulations and experimental tests showed a larger number of photoelectrons collected by the prototype detector with the acrylic light guide, with a mean value of 41 p.e from simulation results. On the other hand, from simulations of neutron capture, there was not significant difference between acrylic and Miro–2. The comparison between simulations of neutron capture and α source signals (μ_{simN}/μ_{simA}) gave ratios very close to one: 0.90, 0.98 and 0.97, for acrylic, Miro–2 and Miro Silver, respectively.

From simulation results, it was observed that the collection of light with Miro–2 and acrylic light guides, were better than with the Miro Silver light guide, by about 15 p.e. From comparing experimental and simulation results, it was found that a lower bound for experimental results may be set around 25 p.e., for neutron capture in the prototype

detector with the acrylic light guide.

Additional simulations were performed with different geometries in such a way that all light guides had the same shape. The results showed a significant difference between air-core and acrylic light guides, where the latter showed a larger number of photoelectrons collected at the PMT. When comparing the light collection for different lengths of the light guide, it was observed that a larger collection was obtained with a shorter light guide and without light guide; however, the width of Gaussian distributions were increased about 1.2 and 3.3 times, respectively.

In the future, one of the goals of further simulation efforts might be to implement ultra–cold neutrons in Geant4, in order to simulate these being captured in the stack glass. This will allow to improve the simulations for the UCN detector of the neutron EDM experiment at TRIUMF. Another goal might be the simulation of a 9×9 array of prototype detectors, as shown in Figure 3.16. These results may be used to compare the simulations to the experimental data collected with the detector constructed at the University of Winnipeg, which was tested with UCN in August of 2015 at PSI (rate comparisons between the detectors and channels are among the planned analysis to perform from the data collected [BJ15]).

Appendix A

LIFETIME OF UCN IN SUPERFLUID HE-II

Figure A.1 shows the loss rate as a function of the temperature for UCN interacting with superfluid He-II. The graph was extracted from the work developed by Golub et al. in [G+83].

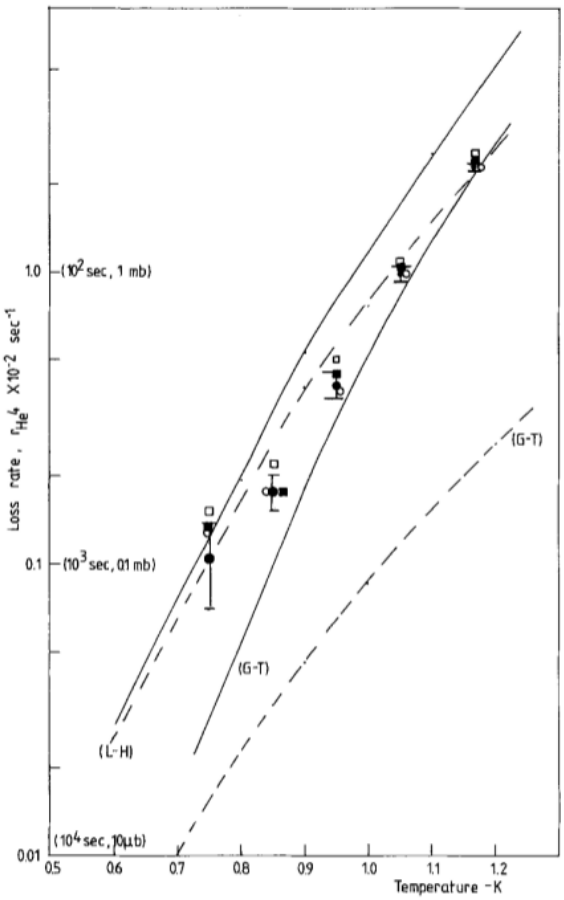

Fig. A.1 Lifetime of UCN in superfluid He-II [G+83].

Appendix B

STORAGE TIME IMPROVEMENTS AT RCNP

Table B.1 shows the evolution of the UCN production by using a superthermal He-II source at RCNP. It includes information about the year, proton beam current (I_p), storage time (τ), temperature inside the Helium-II bottle and a comment about each limit reached. The UCN density at the experimental port was improved from $\rho = 0.7$ UCN/cm^3 obtained in 2002 to $\rho = 26.0 \pm 2.0$ UCN/cm^3 reached in 2011 [Mat13] [C15].

Year	I_p	τ	T_{HeII}	Comment
2002	200nA	14s	1.2K	First UCN production
Jun-2006	1μA	29s	0.9K	Use ^{3}He cryostat
Nov-2006	1μA	34s	0.8K	Improve cryostat
Jul-2007	1μA	39s	0.8K	Remove ^{3}He contamination
Apr-2008	1μA	47s	0.8K	Fombling coating
Dec-2009	1μA	61s	0.8K	Alkali cleaning
Feb-2011	1μA	81s	0.8K	High temperature baking

Table B.1 Storage time improvements implemented in the experiment at RCNP [C15].

Appendix C

MAGNETIC FIELD OF THE ANALYZER AT RCNP

Figure C.1 shows the magnetic field of the analyzer at RCNP as a function of the distance from the center, measured by E. Pierre [Pie13]. The distance from the analyzer to the PMT will be 22 cm [C15].

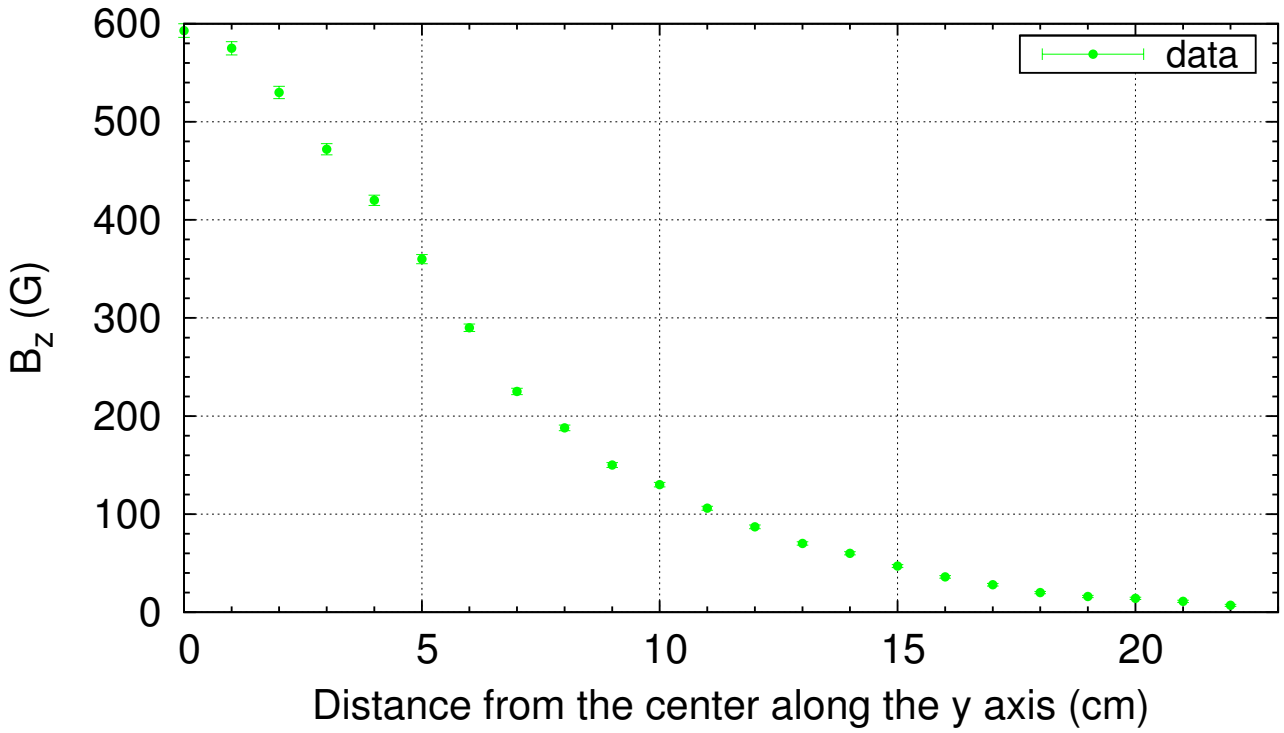

Fig. C.1 Magnetic field of the analyzer at RCNP as a function of the distance. z and y axes correspond to the beamline and vertical axes, respectively.

Appendix D

RATE OF UCN REACHING THE UCN DETECTOR (GEANT4 SIMULATIONS)

UCN will be transported from the EDM cell to the detector using a design similar to the one used in the UCN experiment at PSI [HÍ14]. After the spin precesion sequence has been completed, UCN will be allowed to fall freely in a vertical guide through a distance of $\sim$ 1.6 m, impinging on the detector at a total instantaneous rate of 1.3 MHz [Com13]. Simulations were performed by Hansen-Romu and Jamieson [HJ12b] in order to estimate the fraction of UCN reaching the UCN detector for different valve diameters. In particular, results for a 41 mm and 20 mm radius opening of the valve, are shown in this appendix in figures D.1(a) and D.1(b), respectively.

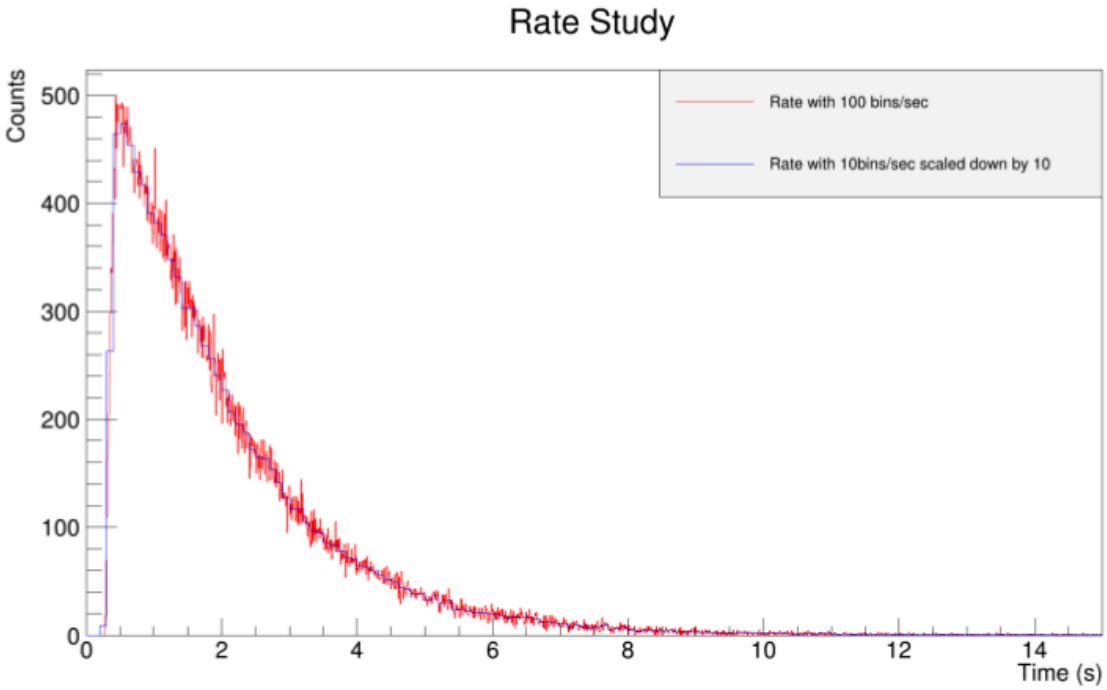

(a) UCN rate using a valve of 41 mm radius.

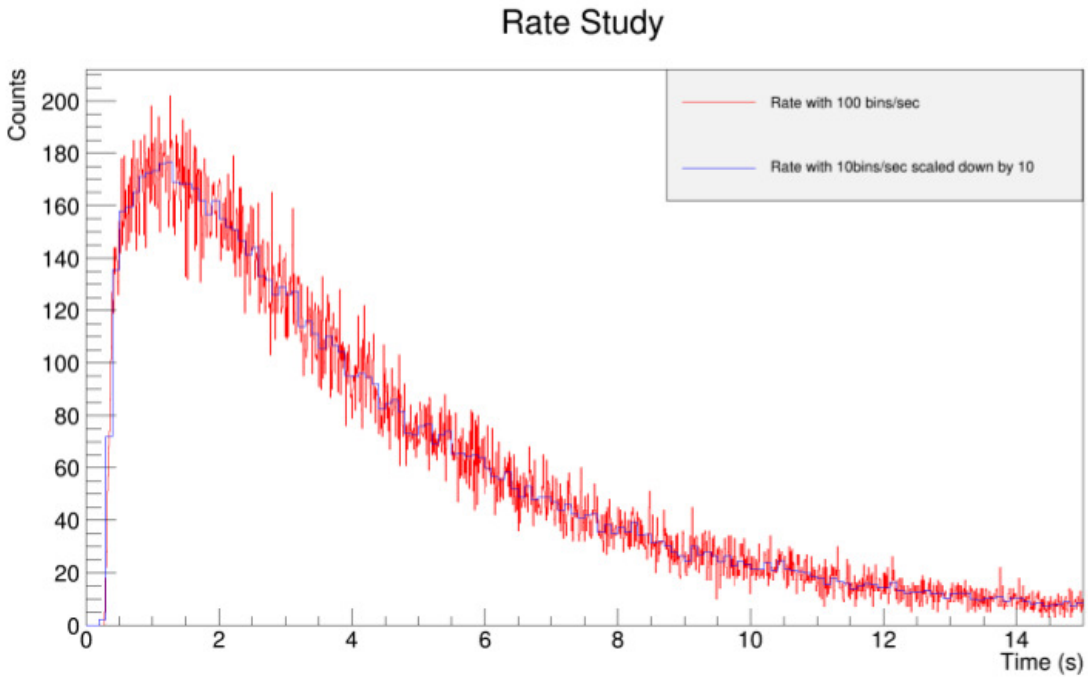

(b) UCN rate using a valve of 20 mm radius.

FIG. D.1 Distributions obtained from Geant4 simulations for the rate of neutrons reaching the detector for two different diameters of the valve [HJ12b].

Appendix E

NEUTRON CAPTURE SIMULATIONS IN THE PRESENCE OF GAMMA BACKGROUND AT DIFFERENT ENERGIES

Figures E.1(a) and E.1(b) show two of the simulation results obtained by Hansen-Romu and Jamieson [HJ13] for neutron captures in a lithium glass of 1 mm thickness, in the presence of gamma background at different energies. These simulations were run for 500000 events of gamma-rays at 5 MeV, 1 MeV, 500 keV, 100 keV and 50 keV. From these results, it was found that 90% of the detected gamma–rays had energies below 3 MeV.

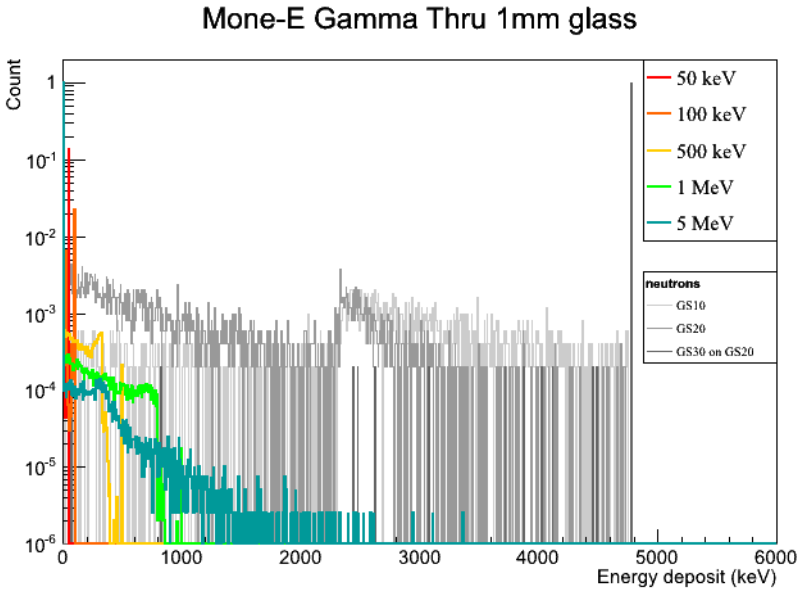

(a) Energy deposited by different gamma-rays and UCN in the lithium glass.

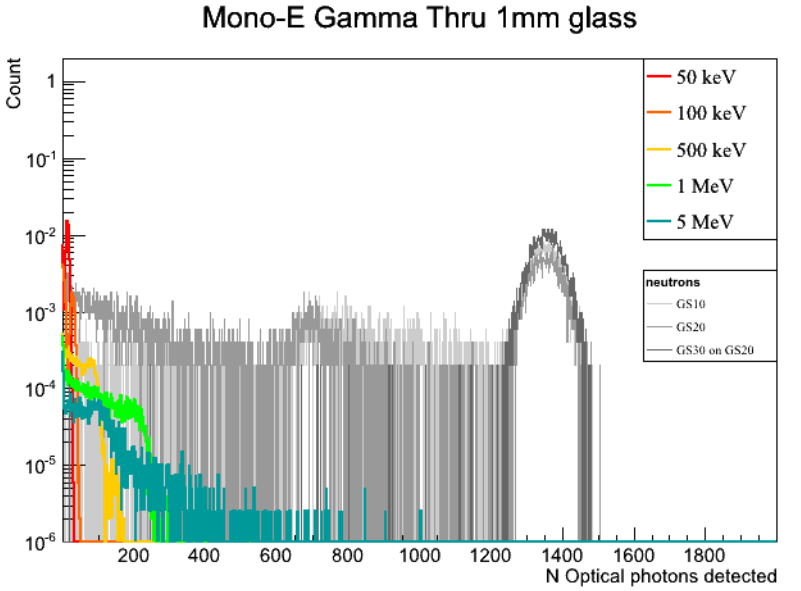

(b) Number of photons detected from gamma-rays at different energies and UCN captures.

FIG. E.1 Distributions obtained from Geant4 simulations of gamma-rays of different energies and UCN captures in the lithium glass [HJ13].

Appendix F

CERIUM ACTIVATED GLASS SCINTILLATORS IN GEANT4

Extract of the simulation code showing the implemented parameters in the 6-lithium glass stack. The emission spectrum of cerium activated glass scintillators is to the right in Figure F.1 [Spo77]; this spectrum exhibits a maximum emission for wavelengths around 395 nm. Values from the graph were used to define the emision energies of light in the 6-Lithium doped glass in the Geant4 class `LiGDetectorConstruction`. Another parameter defined in the simulation corresponds to the `scintillationyield`, measured by Spowart in [Spo69].

```
//**** 6-Lithium glasses property table ****//

   const G4int LiG_NUMENTRIES = 19;
  G4double LiG_Energy[LiG_NUMENTRIES] = {
    2.480*eV,
    2.530*eV,
    2.583*eV,
    2.638*eV,
    2.695*eV,
    2.755*eV,
    2.818*eV,
    2.883*eV,
    2.952*eV,
    3.024*eV,
```

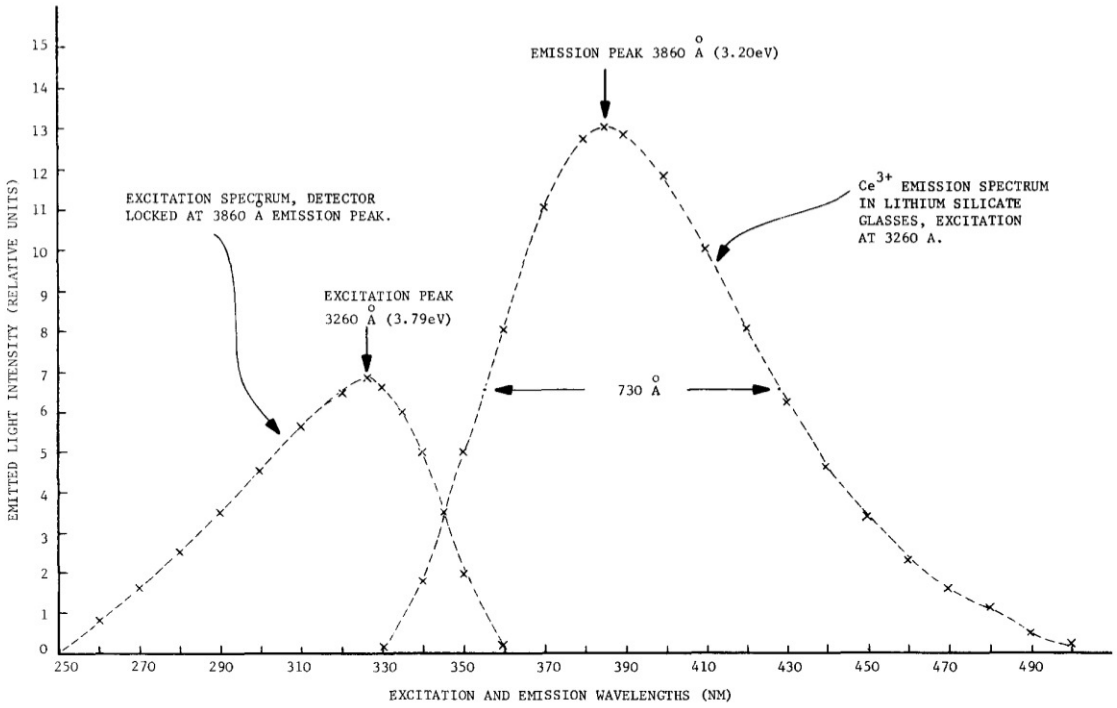

FIG. F.1 Excitation (left) and emission (right) distributions of cerium activated glass scintillators [Spo77].

```
    3.100*eV,
    3.179*eV,
    3.212*eV,
    3.263*eV,
    3.351*eV,
    3.444*eV,
    3.542*eV,
    3.647*eV,
    3.757*eV };


  G4double LiG_SCINT[LiG_NUMENTRIES] = {
    0.00088378,
```

```
  0.00353513,
  0.01060539,
  0.01679187,
  0.02209457,
  0.02739726,
  0.03977022,
  0.05214317,
  0.07070261,
  0.08572691,
  0.10251878,
  0.11400795,
  0.11489171,
  0.11224039,
  0.09721609,
  0.07070261,
  0.04242156,
  0.01590809,
  0.00044189};


G4double LiG_RIND[LiG_NUMENTRIES]  = { 1.55 , 1.55, 1.55,
                                       1.55 , 1.55, 1.55,
                                       1.55 , 1.55, 1.55,
                                       1.55 , 1.55, 1.55,
                                       1.55 , 1.55, 1.55,
                                       1.55 , 1.55, 1.55,
                                       1.55 };
G4double LiG_ABSL[LiG_NUMENTRIES]  = { 5.*m, 5.*m, 5.*m,
                                       5.*m, 5.*m, 5.*m,
```

```
                                        5.*m, 5.*m, 5.*m,
                                        5.*m, 5.*m, 5.*m,
                                        5.*m, 5.*m, 5.*m,
                                        5.*m, 5.*m, 5.*m,
                                        5.*m };
G4MaterialPropertiesTable* LiG_GS20 = new G4MaterialPropertiesTable();
LiG_GS20->AddProperty("FASTCOMPONENT", LiG_Energy, LiG_SCINT, LiG_NUMENTRIES);
LiG_GS20->AddProperty("SLOWCOMPONENT", LiG_Energy, LiG_SCINT, LiG_NUMENTRIES);
LiG_GS20->AddProperty("RINDEX",        LiG_Energy, LiG_RIND,  LiG_NUMENTRIES);
//ABSLENGTH is simply the distacne a poton will travel before geant kills it
LiG_GS20->AddProperty("ABSLENGTH",     LiG_Energy, LiG_ABSL,  LiG_NUMENTRIES);
// below number is form Spowart, NIM 75 (1969) 35
// 510 eV/photon
LiG_GS20->AddConstProperty("SCINTILLATIONYIELD", 1961./MeV);
LiG_GS20->AddConstProperty("RESOLUTIONSCALE", 1.);
LiG_GS20->AddConstProperty("FASTTIMECONSTANT", 50.*ns);
LiG_GS20->AddConstProperty("SLOWTIMECONSTANT", 70.*ns);
LiG_GS20->AddConstProperty("YIELDRATIO", 0.667);

//LiG->SetMaterialPropertiesTable(LiG_mt);
GS20->SetMaterialPropertiesTable(LiG_GS20);
// Set the Birks Constant for the--LiG--GS20 scintillator to zero(not organic)
GS20->GetIonisation()->SetBirksConstant(0.0*cm/MeV);//0.0111*cm/MeV);
```

Appendix G

OPTICAL PROPERTIES OF MIRO SILVER IN GEANT4

Plots of reflectivities as a function of the wavelength for Miro Silver and Miro (in a general case), are shown in Figure G.1. An extract from the code in Geant4 for Miro Silver is shown below, containing the corresponding optical properties previously described in section 4.3.

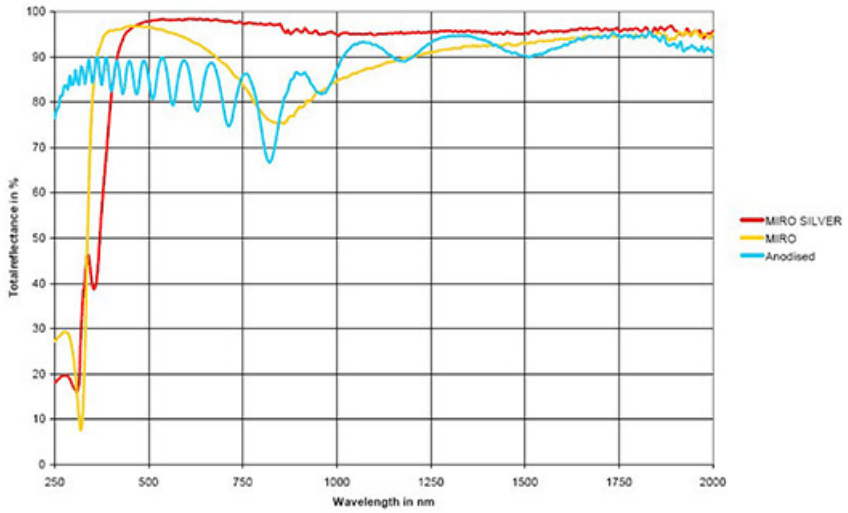

Fig. G.1 Values for reflectivity and wavelength for Miro Silver and Miro [Ala14].

```
/***** Optical properties (Miro Silver - rectangle) ******/

G4OpticalSurface* simpleBox3_OpticalSurface = new G4OpticalSurface
("simpleBox3_Optical_Surface" );
```

```
simpleBox3_OpticalSurface->SetType ( dielectric_metal );
simpleBox3_OpticalSurface->SetFinish ( polished );
simpleBox3_OpticalSurface->SetModel ( glisur );
new G4LogicalSkinSurface("simpleBox3_surf",SimpleBox_log,
simpleBox3_OpticalSurface);
G4double EPhotonSB[19] =

{
  4.0158*eV,
  4.0115*eV,
  3.9636*eV,
  3.7649*eV,
  3.5324*eV,
  3.4507*eV,
  3.3368*eV,
  3.3014*eV,
  3.1629*eV,
  3.0658*eV,
  2.9723*eV,
  2.7223*eV,
  2.5545*eV,
  2.3476*eV,
  2.2562*eV,
  2.0933*eV,
  1.9523*eV,
  1.829*eV,
  1.784*eV
};
```

```
G4double ReflectivitySB[19] =

{
  0.2624,
  0.1844,
  0.3121,
  0.4539,
  0.3865,
  0.4433,
  0.578,
  0.6454,
  0.8014,
  0.9007,
  0.9255,
  0.9716,
  0.9787,
  0.9823,
  0.9823,
  0.9858,
  0.9823,
  0.9823,
  0.9787

};

G4MaterialPropertiesTable *simpleBox3_MPT = new G4MaterialPropertiesTable();
simpleBox3_MPT->AddProperty ( "REFLECTIVITY", EPhotonSB, ReflectivitySB, 19 );
simpleBox3_OpticalSurface->SetMaterialPropertiesTable (simpleBox3_MPT);
```

Appendix H

QUANTUM EFFICIENCY OF THE PHOTOCATHODE IN GEANT4

Extract from the implemented code in the simulation for the photocathode:

```
 G4OpticalSurface* photocath_opsurf=
   new G4OpticalSurface("photocath_opsurf",glisur,polished,
                        dielectric_metal);

const G4int numEne = 33;
const G4double ltoE = 1239.853; // eV * nm
G4double EphotonPC[numEne] =

 {
    ltoE/304.9 *eV,
    ltoE/324.8 *eV,
    ltoE/360.9 *eV,
    ltoE/388 *eV,
    ltoE/420.6 *eV,
    ltoE/449.5 *eV,
    ltoE/478.4 *eV,
    ltoE/501.9 *eV,
    ltoE/509.1 *eV,
```

```
      ltoE/518.2 *eV,
      ltoE/521.8 *eV,
      ltoE/530.8 *eV,
      ltoE/534.4 *eV,
      ltoE/547.1 *eV,
      ltoE/561.5 *eV,
      ltoE/567 *eV,
      ltoE/577.8 *eV,
      ltoE/581.4 *eV,
      ltoE/590.5 *eV,
      ltoE/594.1 *eV,
      ltoE/601.3 *eV,
      ltoE/604.9 *eV,
      ltoE/610.3 *eV,
      ltoE/614 *eV,
      ltoE/617.6 *eV,
      ltoE/621.2 *eV,
      ltoE/624.8 *eV,
      ltoE/628.4 *eV,
      ltoE/630.2 *eV,
      ltoE/632 *eV,
      ltoE/637.4 *eV,
      ltoE/639.3 *eV,
      ltoE/642.9 *eV,
      ltoE/648.3 *eV

};

  G4double photocath_EFF[numEne]={
```

0.1969,

0.2231,

0.2484,

0.2442,

0.24,

0.2237,

0.1941,

0.1655,

0.1542,

0.1224,

0.112,

0.0938,

0.0843,

0.0706,

0.0551,

0.0504,

0.0415,

0.0394,

0.0318,

0.0292,

0.0236,

0.0212,

0.0175,

0.0157,

0.0132,

0.0121,

0.0096,

0.0087,

```
    0.0073,
    0.0065,
    0.0053,
    0.0048,
    0.0038,
    0.0029

};

G4MaterialPropertiesTable* photocath_mt = new G4MaterialPropertiesTable();
photocath_mt->AddProperty("EFFICIENCY",EphotonPC,photocath_EFF,numEne);
photocath_mt->AddProperty("REFLECTIVITY",EphotonPC,photocath_REFL,numEne);
photocath_opsurf->SetMaterialPropertiesTable(photocath_mt);
new G4LogicalSkinSurface("photocath_surf",photocath_log,photocath_opsurf);
```

Appendix I

VERIFICATION OF THE ^{6}LI CONTENT OF THE DETECTOR STACK BY ORIENTATION VIA NEUTRON CAPTURE STUDIES

The experimental setup used by B. Jamieson and L. Rebenitsch [JR15] to identify the depleted and doped sides of the ^{6}Li glass stack, consists of AmBe and ^{252}Cf neutron sources, and a high sensitivity detector (Ortec A-016-025-500), as shown in Figure I.1(a). The signal produced was preamplified (Ortec 142), amplified (Ortec 572A) and finally read by a Multi-Channel Analyzer in which spectra of the deposited energy were generated. As result of data collection, they observed an excess of events in the range of energies between 1.3 MeV and 2.9 MeV, for one of the orientations of the glass stack (see Figure I.1(b)).

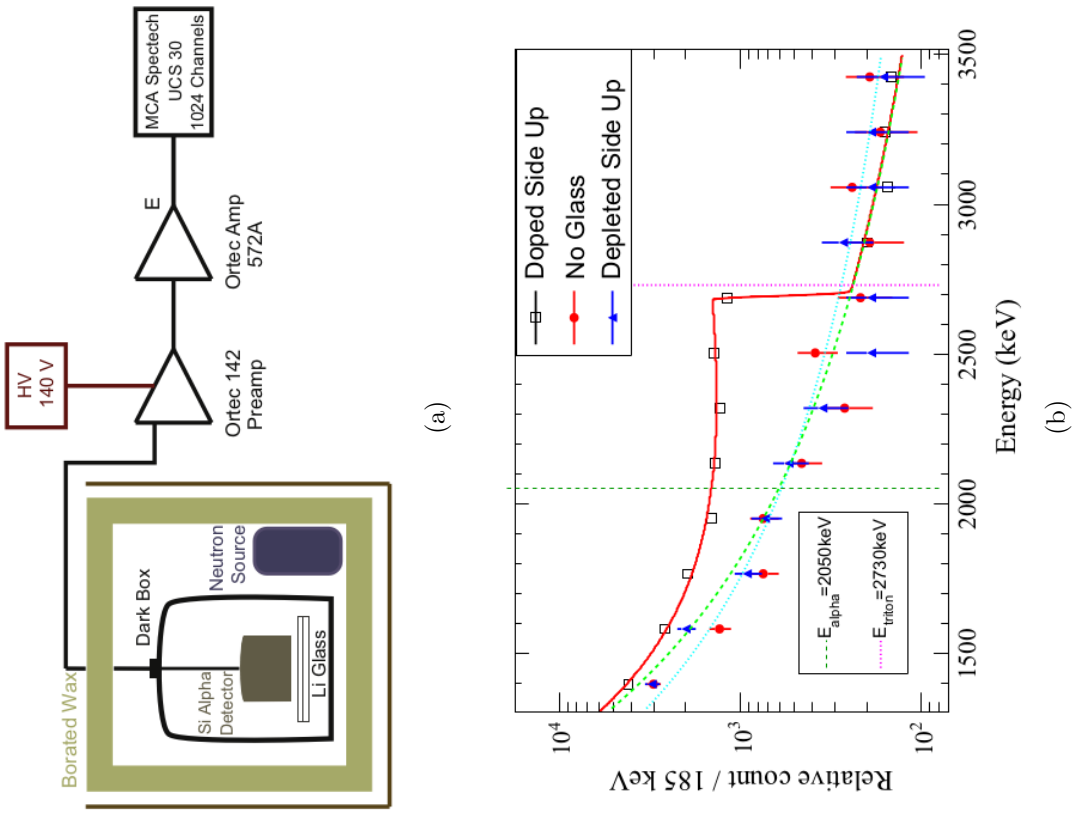

FIG. I.1 I.1(a) Diagrammatic representation of the experimental setup at the University of Winnipeg. I.1(b) Vertical dotted lines show the alpha (2.05 MeV) and triton (2.73 MeV) energies for neutron capture. Black squares are the measurements when the doped glass faced the Si detector. Blue and red dots shows the neutron capture data for the depleted side facing the Si detector and when there was no glass, respectively [JR15].

Appendix J

NEUTRON CAPTURE SIMULATIONS IN GLASS TYPES GS10, GS20, GS30 AND GS20/GS30

Geant4 simulations for the light collection from neutron capture in glass types GS10, GS20, GS30 and GS20/GS30, were performed by Hansen-Romu and B. Jamieson [HJ12a]. The dimensions of the glasses were of $20 \times 20 \times 1$ mm^3, and the results from simulations are shown in Figures J.1 and J.2. The spectrum for the number of photons incident upon the PMT exhibits a peak around 1350 photons for glasses GS10 and GS20 (Figures J.1(a) and J.1(b)). There are edge effects in both distributions, however, these are smaller for the GS10 glass. GS30 exhibits a small number of photons around the peak found by the other glasses, but most of the neutrons travel right through this material (Figure J.2(a)). For the glass stack GS20/GS30 (Figure J.2(b)), the edge effects disappear for the GS20 glass and the spectrum for the light incident on the PMT shows only the distribution with a mean value around 1350 photons. Note that this study focused on the number of photons incident on the PMT. With 24% QE as in the PMT chosen for this thesis work, the Npe predicted for a 0 cm guide is therefore in reasonable agreement with that reported here (390 for 0 cm guide, Table 4.10).

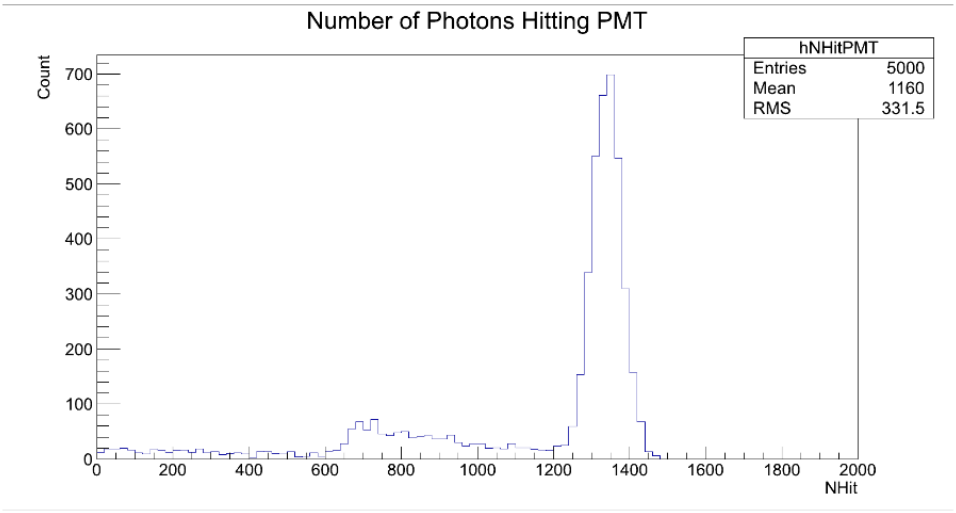

(a) NHit distribution for the GS10 glass.

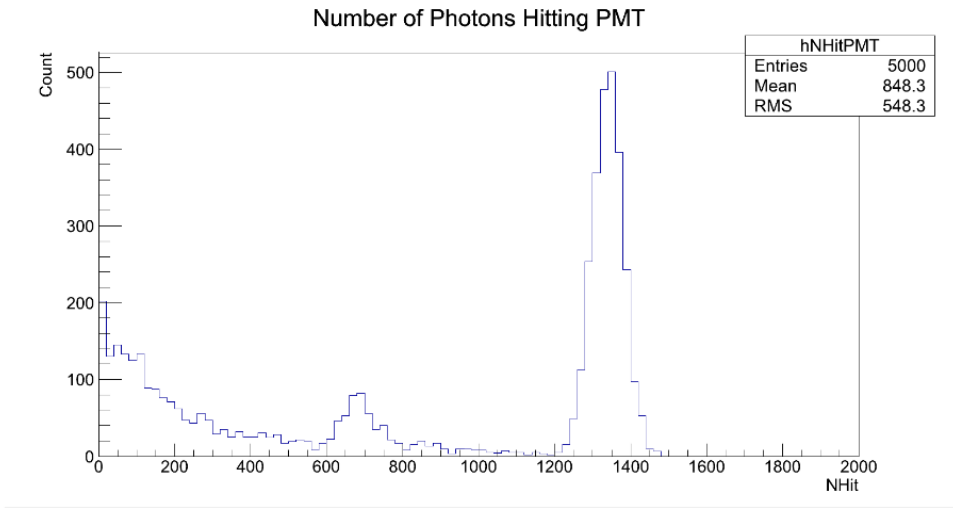

(b) NHit distribution for the GS20 glass.

FIG. J.1 Number of photons hitting the photomultiplier (NHit) distributions for the prototype detector without light guide and with GS10 and GS20 scintillator glasses, obtained from neutron capture simulations [HJ12a].

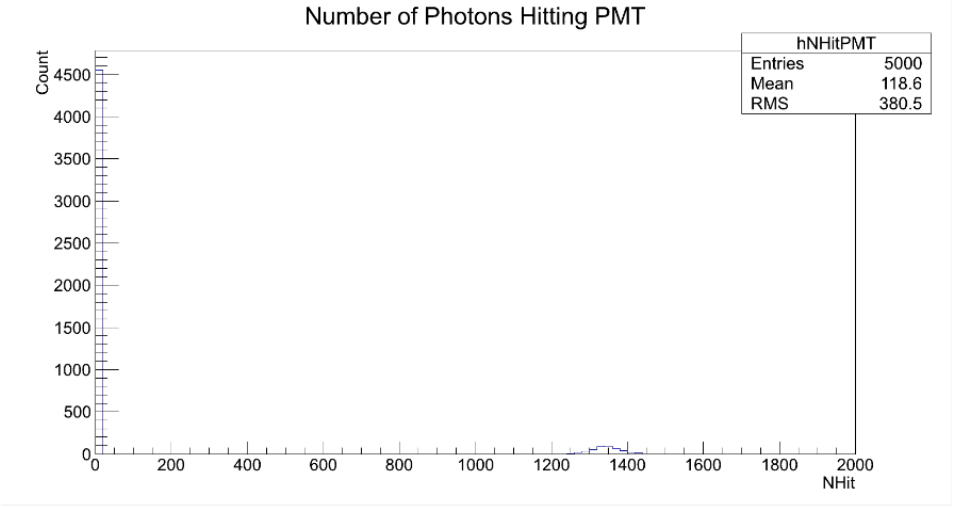

(a) NHit distribution for the GS30 glass.

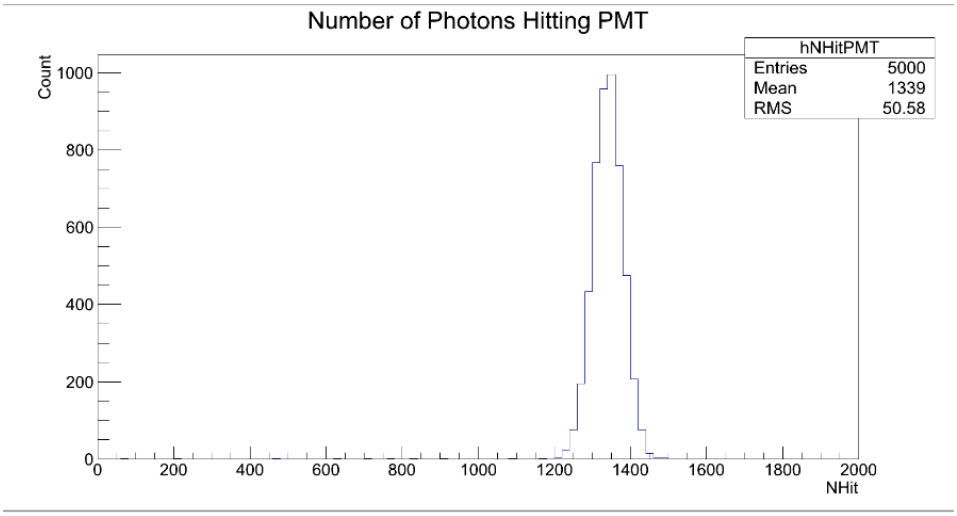

(b) NHit distribution for the glass stack.

FIG. J.2 Number of photons hitting the photomultiplier (NHit) distributions for the prototype detector without light guide and with GS30 and GS20/GS30 scintillator glasses, obtained from neutron capture simulations [HJ12a].

BIBLIOGRAPHY

[A+12] I. Altarev et al., *A next generation measurement of the electric dipole moment of the neutron at the FRM II*, Nuovo Cim. **122** (2012), no. C35. (Cited in page 26.)

[ABA+06] U. Akgun, P. Bruecken, A.S. Ayan, F. Duru, J. Olson, E.A. Albayrak, E. Gulmez, A. Mestvirishvili, Y. Onel, and I. Schmidt, *Radiation damage and light transmission studies on air core light guides*, Nuclear Science, IEEE Transactions on **53** (2006), no. 3, 1547–1550. (Cited in page 63.)

[AC+09] M. Arai, K. Crawford, et al., *Neutron Sources and Facilities*, ch. 2, p. 21, Springer, 2009. (Cited in page 31.)

[Aea03] S. Agostinelli and J. Allison et al., *Geant4—a simulation toolkit*, Nuclear Instruments and Methods in Physics Research Section A: Accelerators, Spectrometers, Detectors and Associated Equipment **506** (2003), no. 3, 250–303. (Cited in page 77.)

[AL12] H. Abele and H. Leeb, *Gravitation and quantum interference experiments with neutrons*, New Journal of Physics **14** (2012), no. 5, 055010. (Cited in page 15.)

[Ala14] *Alanod*, 2014 (accessed December 5, 2014), http://alanod.com/opencms/opencms/en/index.html. (Cited in pages 80, 84 e 135.)

[Ale92] Yu. A. Alexandrov, *Fundamental Properties of the Neutron*, p. 39, Oxford Science Publications, 1992. (Cited in page 19.)

[Ale10] A. Aleksandrov, *Overview and Future Demands of Fast Choppers*, 2010, http://silver.j-parc.jp/linac10/WE104.PDF. (Cited in pages 30, 31 e 32.)

[AST14] *Applied Scintillation Technologies*, 2014 (accessed October 21, 2014), http://www.appscintech.com/. (Cited in page 56.)

[AST15] *Applied Scintillation Technologies*, 2015 (accessed July 20, 2015), http://www.apace-science.com/ast/g_scint.htm. (Cited in page 60.)

[B+12] J. Beringer et al., *(Particle Data Group)*, PR **D86** (2012), no. 010001, http://http://pdg.lbl.gov. (Cited in page 15.)

[BBL+09] G. Ban, K. Bodek, T. Lefort, O. Naviliat-Cuncic, E. Pierre, C. Plonka, and G. Rogel, *UCN detection with 6Li-doped glass scintillators*, Nuclear Instruments and Methods in Physics Research Section A: Accelerators, Spectrometers, Detectors and Associated Equipment **611** (2009), no. 2–3, 280–283, Particle Physics with Slow Neutrons. (Cited in pages 56, 57 e 58.)

[BCS04] N. Bretón, J.L. Cervantes-Cota, and M. Salgado (eds.), *The Early Universe and Observational Cosmology*, Lecture Notes in Physics, vol. 646, Springer-Verlag Berlin Heidelberg, 2004. (Cited in page 20.)

[Ben06] J. Benlliure, *Spallation Reactions in Applied and Fundamental Research*, vol. 700, pp. 191–238, Springer, 2006. (Cited in page 28.)

[BFL+05] G. Ban, X. Fléchard, M. Labalme, et al., *First Tests of 6Li Doped Glass Scintillators for Ultracold Neutron Detection* , J. Res. Natl. Inst. Stand. Technol. **110** (2005), no. 3, 283–288. (Cited in pages 25, 56 e 57.)

[BJ15] Collaboration Meeting Aug 24 2015 Blair Jamieson, UCN Detector Overview, Private communication, 2015. (Cited in page 120.)

[BRS05] J. Basdevant, J. Rich, and M. Spiro, *Fundamentals in Nuclear Physics*, pp. 299–301, Springer, 2005. (Cited in page 40.)

[C+10] C.A. Baker et al., *CryoEDM: a cryogenic experiment to measure the neutron Electric Dipole Moment*, Journal of Physics: Conference Series **251** (2010), no. 1, 012055. (Cited in page 26.)

[C15] International UCN Source Committee and nEDM Experiment at TRIUMF Conceptual Design Report 2015, Private communication, 2015. (Cited in pages 21, 22, 23, 25, 26, 30, 33, 35, 43, 47, 49, 50, 56, 70, 72, 73, 123 e 125.)

[CAE15a] *CAEN S.p.A.* , 2015 (accessed February 20, 2015), http://www.caen.it/csite/CaenProd.jsp?idmod=48&parent=11. (Cited in pages 97 e 98.)

[CAE15b] *CAEN S.p.A.* , 2015 (accessed February 20, 2015), http://www.caen.it/csite/CaenProd.jsp?idmod=41&parent=11. (Cited in pages 97 e 98.)

[CAE15c] *CAEN S.p.A.* , 2015 (accessed February 20, 2015), http://www.caen.it/csite/CaenProd.jsp?idmod=445&parent=11. (Cited in page 99.)

[Car90] J.M. Carpenter, *Cold Moderator for Pulsed Neutron Sources*, Argonne National Laboratory. Los Alamos, N.M., March 1990, pp. 4–5. (Cited in page 39.)

[Car04] ———, *Neutron Production, Moderation, and Characterization*, 2004, http://www.neutron.anl.gov/NeutronProduction.pdf, p. 11. (Cited in page 39.)

[CCK15] J.M. Carpenter and L. Chun-Keung, *Elements of slow-neutron scattering: basics, techniques and applications*, p. 5, Cambridge University Press, 2015. (Cited in page 40.)

[CDS12] L. Canetti, M. Drewes, and M. Shaposhnikov, *Matter and antimatter in the universe*, New Journal of Physics **14** (2012), no. 095012. (Cited in page 19.)

[COD15] CODATA, *The NIST Reference on Constants, Units, and Uncertainties*, 2014 (accessed Sept, 2015), http://physics.nist.gov/cgi-bin/cuu/Value?munn|search_for=neutron+magnetic+moment. (Cited in page 17.)

[Com13] TRIUMF UCN Detector Technical Design Note Committee, Private communication, 2013. (Cited in pages 74 e 127.)

[Com14] nEDM experiment at TRIUMF Experiment Committee, private communication, 2014. (Cited in pages 72, 73, 75, 78 e 79.)

[Dat77] D.W. Datlowe, *Pulse pile-up in nuclear particle detection systems with rapidly varying counting rates*, Nuclear Instruments and Methods **145** (1977), no. 2, 379–387. (Cited in page 73.)

[Dav13] C. Davis, BL1U, Section 1&2, TRI-DN-13-06, 2013. (Cited in pages 31 e 32.)

[E+01] T. Enqvist et al., *Isotopic yields and kinetic energies of primary residues in 1 A GeV 208Pb + p reactions*, Nuclear Physics A **686** (2001), 481–524. (Cited in page 28.)

[F+15] R.B. Firestone et al., *The Isotopes Project Home Page - 241Am Nuclear Science Division - Berkeley Lab*, 2004 (accessed March 5, 2015), http://ie.lbl.gov/toi/nuclide.asp?iZA=950241. (Cited in page 110.)

[G+83] R. Golub et al., *Operation of a Superthermal Ultra-Cold Neutron Source and the Storage of Ultra-Cold Neutrons in Superfluid Helium-4*, Z. Phys. B - Condensed Matter **51** (1983), 187–193. (Cited in page 121.)

[Gar52] R.L. Garwin, *The Design of Liquid Scintillation Cells*, Review of Scientific Instruments **23** (1952), no. 12, 755–757, :/content/aip/journal/rsi/23/12/10.1063/1.1746152. (Cited in page 63.)

[Gea15a] *Geant4 User's Guide for Application Developers*, 2015 (accessed January 29, 2015), http://geant4.web.cern.ch/geant4/UserDocumentation/UsersGuides/ForApplicationDeveloper/html/. (Cited in pages 14 e 84.)

[Gea15b] *Geant4 - Example LXe*, 2015 (accessed January 30, 2015), http://geant4.web.cern.ch/geant4/UserDocumentation/Doxygen/examples_doc/html/ExampleLXe.html. (Cited in page 85.)

[Gea15c] *Geant4 - Example LXe*, 2015 (accessed January 31, 2015), http://wiki.opengatecollaboration.org/Users_Guide_V6.2:Generating_and_tracking_optical_photons. (Cited in page 84.)

[GNS95] W. Greiner, L. Neise, and H. Stocker, *Thermodynamics and Statistical Mechanics*, pp. 172–174, Springer, 1995. (Cited in pages 37 e 38.)

[GP77] R. Golub and J. M. Pendlebury, *THE INTERACTION OF ULTRA-COLD NEUTRONS (UCN) WITH LIQUID HELIUM AND A SUPERTHERMAL UCN SOURCE*, PHYSICS LETTERS **62 A** (1977), no. 5, 337–339. (Cited in page 43.)

[GRL91] R. Golub, D. Richardson, and S. Lamoreaux, *Ultra-Cold Neutrons*, pp. 1–8, 62–66, Taylor & Francis, January 1991. (Cited in pages 17, 18 e 44.)

[HÍ4] V. Hélaine, *Neutron Electric Dipole Moment measurement: simultaneous spin analysis and preliminary data analysis*, Ph.D. thesis, Université de Caen Basse-Normandie, 2014. (Cited in pages 19, 24, 26, 71, 73 e 127.)

[Ham14] *Hamamatsu Photonics K.K.*, 2014 (accessed November 6, 2014), http://www.hamamatsu.com/us/en/index.html. (Cited in pages 68 e 111.)

[Ham15] *Hamamatsu Photonics K.K., Chapter 4 - Characteristics of photomultiplier tubes*, 2015 (accessed May 9, 2015), http://www.hamamatsu.com/resources/pdf/etd/PMT_handbook_v3aE-Chapter4.pdf. (Cited in page 67.)

[HB212] HB2012: Proceedings of the 52nd ICFA Advanced Beam Dynamics Workshop on High-Intensity and High-Brightness Hadron Beams, *Beam Dynamics of the ESS Superconducting Linac*, September 2012. (Cited in page 32.)

[HJ12a] S. Hansen-Romu and B. Jamieson, *Photon Count – Lithium Glass Scintillator – Geant4 Simulation*, Private communication, 2012. (Cited in pages 9, 58, 145, 146 e 147.)

[HJ12b] ———, *Simulations of lithium glass scintillation*, Private communication, 2012. (Cited in pages 73, 127 e 128.)

[HJ13] ———, *Geant4 UCN Rate Study*, Private communication, 2013. (Cited in pages 74, 129 e 130.)

[JC83] G.L. Jensen and J.B. Czirr, *Gamma-ray sensitivity of 6li-glass scintillators*, Nuclear Instruments and Methods in Physics Research **205** (1983), no. 3, 461 – 463. (Cited in page 58.)

[JR15] B. Jamieson and L.A. Rebenitsch, *Determining the 6li doped side of a glass scintillator for ultra cold neutrons*, Nuclear Instruments and Methods in Physics Research Section A: Accelerators, Spectrometers, Detectors and Associated Equipment **790** (2015), 6 – 9. (Cited in pages 60, 143 e 144.)

[Kas04] M. Kasprzak, *Thermal up-scattering of very cold and ultra-cold neutrons in solid deuterium* , Master's thesis, Jagiellonian University, Kraków, 2004, http://arxiv.org/abs/nucl-ex/0407022v1. (Cited in pages 18 e 43.)

[KL97] I.B. Khriplovich and S.K. Lamoreaux, *CP Violation Withouth Strangeness Electric Dipole Moments of Particles, Atoms, and Molecules*, pp. 77–79, Springer-Verlag Berlin Heidelberg, 1997. (Cited in page 36.)

[Kna12] A.R. Knapitsch, *Photonic Crystals: Enhancing the Light Output of Scintillation Based Detectors*, Ph.D. thesis, Viennna University of Technology, 2012. (Cited in page 60.)

[Kno00] G.F. Knoll, *Radiation Detectibn and Measurement, Third Edition*, pp. 231–272, John Wiley & Sons, Inc., 2000. (Cited in pages 51, 62, 66 e 68.)

[Lam66] J. R. Lamarsh, *Introduction to nuclear reactor theory*, pp. 185–186, Addison-Wesley, 1966. (Cited in page 36.)

[Len93] H. Lengeler, *Superconducting Cavities for Neutron Spallation Sources and other High Intensity Proton Accelerators*, Proceedings of the Sixth Workshop on RF Superconductivity, CEBAF, Newport News, Virginia, USA (R.M. Sundelin, ed.), October 1993. (Cited in page 30.)

[Leo94] W. R. Leo, *Techniques for Nuclear and Particle Physics Experiments, A how-to Approach*, second edition ed., pp. 178–200, Springer-Verlag, 1994. (Cited in pages 61, 63 e 67.)

[LG93] S. Lamoreaux and R. Golub, *Angular distribution of ultracold neutrons produced by scattering of cold neutrons in superfluid He-4*, JETP letters **58** (1993), no. 10, 792–795. (Cited in pages 20 e 45.)

[Lia12] C. Liao, *Study on neutron energy spectrum correction and pulse shape discrimination with a Boron-loaded scintillator*, Master's thesis, The University of Utah, 2012. (Cited in page 50.)

[Lóp10] R. López, *Test and commissioning of the detector system in the 209Bi80+ experiment at the Experimental Storage Ring (ESR) at GSI* , Master's thesis, Westfälische Wilhelms-Universität Münster, 2010. (Cited in pages 84 e 110.)

[LY56] T. D. Lee and C. N. Yang, *Question of Parity Conservation in Weak Interactions*, Phys. Rev. **104** (1956), 254–258. (Cited in page 21.)

[M+02] P. Maier-Komor et al., *An ultracold neutron (UCN) detector with Ti/6LiF multi-layer converter and 58Ni reflector*, Nuclear Instruments and Methods in Physics Research Section A: Accelerators, Spectrometers, Detectors and Associated Equipment **480** (2002), no. 1, 109–113. (Cited in page 26.)

[M+11] P. J. Mohr et al., *1. Physical Constants*, Particle Data Group (2011), http://pdg.web.cern.ch/pdg/2012/reviews/rpp2012-rev-phys-constants.pdf. (Cited in page 37.)

[Mat13] R. Matsumiya, *Study of He-II Spallation UCN Source*, Ph.D. thesis, Osaka University, Osaka, JAPAN, June 2013. (Cited in pages 32, 41, 43, 45, 47 e 123.)

[McK02] D.M. McKinsey, *Detection of Magnetically Trapped Neutrons: Liquid Helium as a Scintillator*, Ph.D. thesis, Harvard University, Cambridge, Massachusetts, February 2002. (Cited in pages 45 e 46.)

[MM+15] K. Matsuta, Y. Masuda, et al., *RCNP Annual Report 2009 - Observation of Ramsey Resonance on UCN*, http://www.rcnp.osaka-u.ac.jp/~annurep/2009/matsuta.pdf. (Cited in page 24.)

[Nae07] Syed Naeem A., *Physics and Engeenering of Radiation Detection*, pp. 337–381, Burlington: Elsevier Science, 2007. (Cited in pages 53, 60, 61, 62 e 87.)

[NHIM10] K. Nakamura, Y. Hamana, Y. Ishigami, and T. Matsui, *Latest bialkali photocathode with ultra high sensitivity*, Nuclear Instruments and Methods in Physics Research Section A: Accelerators, Spectrometers, Detectors and Associated Equipment **623** (2010), no. 1, 276–278. (Cited in page 67.)

[Pie13] E. Pierre, Private communication, 2013. (Cited in pages 72 e 125.)

[Pur50] E.M. Ramsey N.F. Purcell, *On the Possibility of Electric Dipole Moments for Elementary Particles and Nuclei*, Physical Review **78** (1950), 807. (Cited in page 21.)

[Ram82] N.F. Ramsey, *Electric-dipole moments of elementary particles*, Rep. Prog. Phys. **45** (1982). (Cited in pages 13, 21 e 49.)

[Rog09] G. Rogel, *Développement de détecteurs de neutrons ultra-froids et d'un système d'analyse de polarisation pour la mesure du moment électrique dipolaire du neutron MEMBRES du*, Ph.D. thesis, UNIVERSITE de CAEN/BASSE-NORMANDIE, October 2009. (Cited in pages 25, 26 e 58.)

[Roo16] *ROOT Data Analysis Framework*, 2016 (accessed Mar 20, 2016), https://root.cern.ch/. (Cited in page 87.)

[S+13] A.P. Serebrov et al., *New measurements of neutron electric dipole moment*, http://arxiv.org/abs/1310.5588 (2013), 1. (Cited in pages 25 e 26.)

[Sak67] A.D. Sakharov, *Violation of CP invariance, C asymmetry, and baryon asymmetry of the universe*, Pis'ma Zh. Eksp. Teor. Fis. **5** (1967), 32–35. (Cited in page 19.)

[Smi57] J.H Purcell E.M. Ramsey N.F. Smith, *Experimental Limit to the Electric Dipole Moment of the Neutron*, Physical Review **108** (1957), 120–122. (Cited in pages 13 e 21.)

[Soz08] M.S. Sozzi, *Discrete Symmetries and CP Violation, From Experiment to Theory*, pp. 149–197, Oxford University Press, 2008. (Cited in pages 19 e 20.)

[Spo69] A.R. Spowart, *Measurement of the absolute scintillation efficiency of granular and glass neutron scintillators*, Nuclear Instruments and Methods **75** (1969), no. 1, 35–42. (Cited in page 131.)

[Spo77] ———, *Neutron scintillating glasses: Part II: The effects of temperature on pulse height and conductivity*, Nuclear Instruments and Methods **140** (1977), no. 1, 19–28. (Cited in pages 82, 88, 131 e 132.)

[Tes85] K. Tesch, *A simple estimation of the laterial shielding for proton accelerators in the energy range 50 to 1000 MeV*, Radiation Protection Dosymetry **11** (1985), no. 3, 165–172. (Cited in pages 32, 33 e 34.)

[Tri16] *TRIUMF/UCN*, 2016, http://www.triumf.ca/ucn/how-ucn-source-works. (Cited in pages 5 e 44.)

[Tso15] N. Tsoulfanidis, *Measurement and detection of radiation, 4th ed.* , p. 203, Taylor & Francis, 2015. (Cited in page 57.)

[VBZR12] J. Voigt, T. Brückel, R. Zorn, and G. Roth, *02: Neutron Sources*, sep 2012, http://juser.fz-juelich.de/record/127645, pp. 2.1–2.14. (Cited in page 30.)

[WAH+57] C. S. Wu, E. Ambler, R. W. Hayward, D. D. Hoppes, and R. P. Hudson, *Experimental Test of Parity Conservation in Beta Decay*, Phys. Rev. **105** (1957), 1413–1415. (Cited in page 21.)

[Wat03] N. Watanabe, *Neutronics of pulsed spallation neutron sources*, Rep. Prog. Phys. **66** (2003), 339–381. (Cited in page 29.)

[WC09] B.T.M. Willis and C.J. Carlile, *Experimental Neutron Scattering*, pp. 59 – 60, Oxford University Press, 2009. (Cited in page 55.)

[Y+03] K.N. Yu et al., *Comparison among alpha-particle energy losses in air obtained from data of SRIM, ICRU and experiments*, Applied Radiation and Isotopes **59** (2003), 363–366. (Cited in page 86.)

[Yan06] L. Yang, *Towards Precision Measurement of the Neutron Lifetime using Magnetically Trapped Neutrons*, Ph.D. thesis, Harvard University, Cambridge, Massachusetts, May 2006. (Cited in page 19.)

[Zhe12] W. Zheng, *Experiments of Search for Neutron Electric Dipole Moment and Spin-Dependent Short-Range Force*, Ph.D. thesis, Duke University, 2012. (Cited in page 26.)

[ZT12] L. Zheng-Tian, Searches for Electric Dipole Moments (Fundamental Symmetries and Neutrinos Working Group, eds.), August 2012, http://www.phy.ornl.gov/funsym/positions/FundSymm-EDM.pdf. (Cited in page 25.)